Mathematical Modelling of the Mitochondrial Dicarboxylate Carrier (SLC25A10)

Ramin Nashebi*[1], Yingying Lyu[2], Elías Vera-Sigüenza[3], Daniel A. Tennant[2], and Fabian Spill†[1]

[1] *School of Mathematics, University of Birmingham, Birmingham, United Kingdom*
[2] *Institute of Metabolism and Systems Research, College of Medical and Dental Sciences, University of Birmingham, Birmingham, United Kingdom*
[3] *Okinawa Institute of Science and Technology Graduate University (OIST), Information Theory, Probability, and Statistics Unit, Okinawa, Japan*

1 Abstract

The mitochondrial dicarboxylate carrier SLC25A10 exchanges phosphate with dicarboxylates such as succinate and malate, playing a central role in metabolic regulation. Structural studies establish a ping–pong mechanism, but most mathematical models still assume sequential binding, lacking mechanistic justification and overlooking the alternation of a single binding site. Here, we present the first mechanistically derived and thermodynamically consistent model of SLC25A10 based on the ping–pong framework. The model incorporates competitive dicarboxylate binding, phosphate exchange, heteroexchange, reversibility, and electroneutrality, and is validated against experimental datasets. To estimate kinetic parameters and quantify their uncertainty, we employed Bayesian inference, enabling statistically rigorous calibration to competition assays. The model introduces new terms that quantify which substrate and from which side of the membrane is most likely to start the transport cycle. Beyond reproducing rapid exchange of different substrates that cannot be directly measured experimentally, the model captures the influence of mitochondrial morphology, enzymatic interactions, and metabolic perturbations on transporter behavior. Specifically, simulations reveal that matrix swelling increases, while matrix condensation decreases, the early SLC25A10 flux magnitude. Moreover, the model demonstrates how SLC25A10 contributes to succinate handling under SDH deficiency, functioning both as a gatekeeper and a pressure-release valve for matrix succinate. Under these conditions, succinate accumulates and is exported into the intermembrane space via SLC25A10, a process critically dependent on phosphate and malate availability.

*Corresponding author: `rxn315@student.bham.ac.uk`
†Corresponding author: `f.spill@bham.ac.uk`

Keywords

Ping–Pong Mechanism; Bayesian Inference; MCMC; Succinate Metabolism; Mitochondrial Transport Mechanistic Modeling

2 Introduction

The solute carrier family 25 member A10 (SLC25A10), also known as the dicarboxylate carrier, is a transporter located in the inner mitochondrial membrane (IMM) [1, 2, 3, 4, 5, 6]. As its name suggests, this carrier facilitates the exchange of substrates containing two carboxyl groups, such as succinate and malate, together with other anions including inorganic phosphate, sulfate and thiosulfate [2, 4, 7, 8]. This exchanger plays a crucial role in the replenishment of intermediates of the tricarboxylic acid (TCA) cycle, supports oxidative phosphorylation, and maintains redox balance by enabling bidirectional exchange of metabolites [5, 4].

Under conditions such as cancer or ischaemia, SLC25A10 can become increasingly important in regulating succinate and malate levels [5, 2, 4, 9, 10, 11]. Evidence points towards SLC25A10 being a key player in the regulation of carbon metabolism under these circumstances, where its activity may contribute to the induction of a pseudo-hypoxic cellular state that promotes tumorigenesis [12, 13, 14].

Mechanically, SLC25A10 functions as a secondary active antiporter. It does not consume ATP directly, but instead utilizes concentration gradients-particularly phosphate—to drive dicarboxylate exchange [15, 16, 17, 2]. Transport is reversible, meaning that substrates can move in either direction depending on relative gradients, and it supports both homoexchange, the exchange of identical metabolites (e.g., succinate-for-succinate), and heteroexchange, the exchange of different metabolites (e.g., phosphate-for-succinate). Since similar-charged molecules are exchanged in a strict 1:1 stoichiometry, the process is electroneutral and therefore insensitive to mitochondrial membrane potential [15]. Importantly, transport competition between dicarboxylates is well established, with malate generally exhibiting higher binding affinity than succinate [3, 15, 16, 17].

Recent structural studies by Ruprecht et al. [18, 4] and Mavridou et al. [19] have shown that mitochondrial carriers of the SLC25 family, including SLC25A10, function as monomers with a single substrate binding site located in a water-filled cavity. This site is accessible from one side of the inner mitochondrial membrane at a time, consistent with an alternating-access mechanism. Complementary kinetic analyses by Cimadamore-Werthein et al. [1] demonstrated that these carriers operate through a ping–pong exchange mechanism, in which a substrate is bound, translocated and released before the counter-substrate can bind. Together, these structural and kinetic results support a single-displacement alternating mechanism, while challenging earlier sequential models that proposed that phosphate and dicarboxylates could bind simultaneously at distinct sites and be co-transported through conformational changes [3, 20, 21, 22, 23, 24, 15, 16, 17]. This combined evidence provides a strong motivation for revisiting the mathematical modeling of SLC25A10 within a ping pong kinetic framework.

An additional but underexplored layer of regulation is the effect of mitochondrial morphology on SLC25A10 transporter fluxes. Both experimental and computational studies have demonstrated that alterations in the relative volumes of the mitochondrial

matrix (MM) and intermembrane space (IMS), strongly influence metabolite diffusion and SLC25-mediated exchange rates [25, 26, 27, 28, 29]. In particular, swelling of the matrix or IMS dilutes metabolite pools and reduces effective concentration gradients. Because SLC25A10 transport relies on substrate gradients rather than ATP hydrolysis for energy, the relative volumes of the matrix and IMS directly determine the magnitude of its fluxes. Thus, it is worth exploring how volume changes modulate SLC25A10 activity at a coarse-grained level.

Several mathematical models have been developed to explore the kinetics of SLC25A10 [15, 16, 17]. While these models incorporate important features such as electroneutral heteroexchange, competitive inhibition, and thermodynamic constraints, they are generally based on a sequential mechanism and rely on the King–Altman method [30]—a graphical approach that simplifies kinetics but lacks mechanistic depth. As a result, these models are considered conceptual or proxy representations rather than mechanistically derived systems.

In this study, we present the first mechanistically derived and thermodynamically validated kinetic model of the mitochondrial dicarboxylate carrier SLC25A10 based on the ping–pong mechanism. Our framework integrates competitive binding of succinate, malate, and phosphate, phosphate-coupled heteroexchange, reversibility, and electroneutrality, and is calibrated against experimental data using Bayesian inference. In contrast to earlier sequential formulations, our model introduces conformational bias weights that quantify how different substrates bias the initiation of the ping–pong cycle, providing a mechanistic way to capture directional preferences in transporter activity. Beyond reproducing classical transport assays, the model extends experimental observations by revealing mechanistic features that are difficult to probe directly, including transient exchange dynamics, the influence of mitochondrial morphology, and the rewiring of transport behavior under succinate dehydrogenase (SDH) deficiency. In doing so, the model provides a predictive and generalizable framework for studying SLC25A10 and related mitochondrial carriers, linking transporter kinetics to broader physiological and pathological processes such as cancer metabolism and processes in which aberrantly high or low metabolite levels alter transporter activity.

3 Model and Methods

3.1 Model Construction

The ping-pong kinetic mechanism describes an alternating-access process in which the transporter cycles between two distinct conformational states, each exposing a single substrate-binding site to one side of the membrane. This mechanism prevents simultaneous binding of counter-substrates and ensures strictly alternating translocation.

The SLC25A10 transporter is located in the IMM and mediates exchange of dicarboxylates and inorganic anions (e.g., succinate, malate, and phosphate) between the MM and the extra-matrix space. In vivo, these substrates originate from the cytosol (C) and can access the IMS by passing through the outer mitochondrial membrane (OM), which is highly permeable to small metabolites due to the presence of the voltage-dependent anion channel (VDAC) (see Fig. 1). Accordingly, in this study we treat the external compartment as the combined IMS and cytosol space (IMS+C) and the internal compartment as

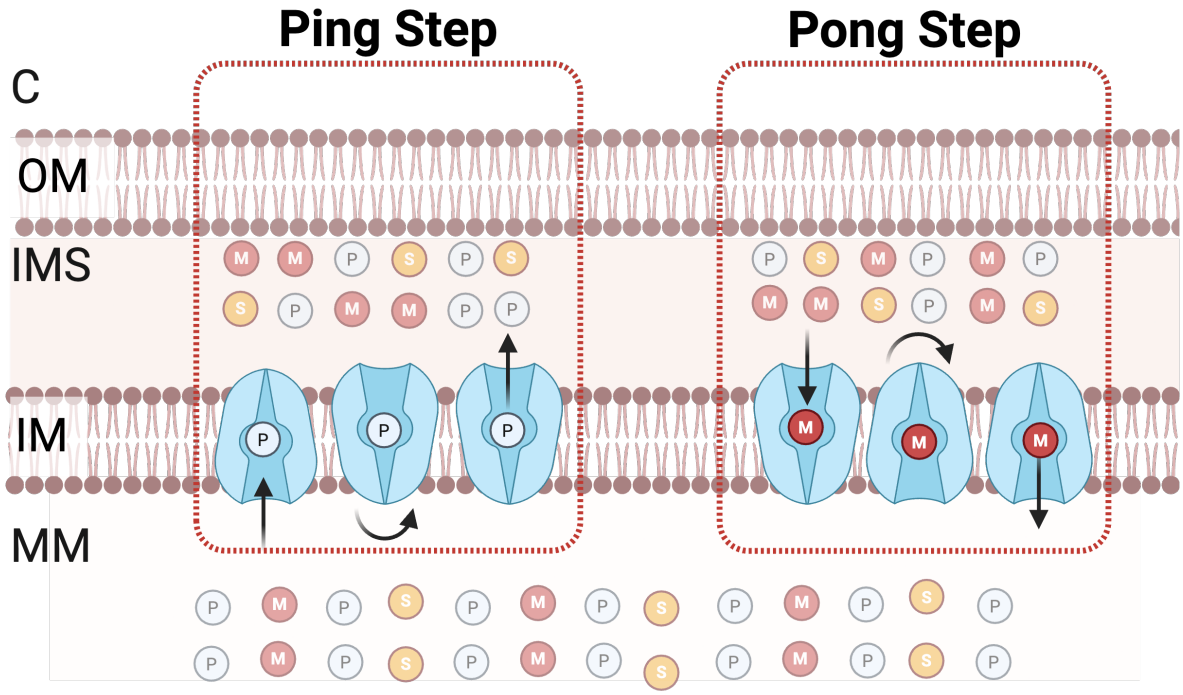

Figure 1: Schematic representation of the SLC25A10 transporter in the IMM, operating via a ping–pong mechanism. The dicarboxylates succinate (S, yellow) and malate (M, red) are exchanged with phosphate (P, white) across the IMM via SLC25A10. In the *ping* step, phosphate is exported from the matrix to the IMS: binding of phosphate is followed by a conformational change and subsequent release into the IMS. In the *pong* step, the vacant binding site is occupied by a malate, which is then imported into the matrix: binding of the malate is followed by a conformational change and final release into the matrix. Created with BioRender.com.

the MM, with transport occurring across the IMM (Fig. 2). For notational simplicity, we refer to this external compartment as the external side (c) throughout the manuscript.

In the mitochondrial matrix, we consider a system where mitochondrial succinate (S_m) and mitochondrial malate (M_m) compete for binding to the carrier. The transporter in its initial state, with the binding site facing the mitochondrial matrix, is denoted T_m (Fig. 2).

Binding of either succinate or malate to T_m depends on their concentrations and binding affinities. When succinate (Fig. 2a) or malate (Fig. 2b) binds, a transient substrate–transporter complex (T_mS or T_mM) is formed [31, 1]. After binding, the carrier can undergo a conformational transition—driven by thermal fluctuations—that reorients the binding site toward the external side, yielding the state T_c. In this configuration, the bound dicarboxylate can dissociate into the external compartment according to the modeled reversible binding/unbinding kinetics, leaving the transporter available to bind the counter-substrate phosphate (P_c) [32]. Upon phosphate binding, the transporter reverts to its original matrix-facing state (T_m) and releases phosphate into the matrix (P_m), thereby completing the transport cycle.

A central feature of this mechanism is that net antiport direction is determined by the prevailing electrochemical driving forces (i.e., the relative substrate gradients and binding-site occupancy) [33, 34, 35]. In the ping–pong cycle, the carrier can bind a substrate on the side to which its binding site is exposed, undergo a conformational reorientation, and release that substrate on the opposite side, after which the counter-substrate binds

and is translocated in the reverse direction. Consequently, SLC25A10 couples exchange direction to the relative concentration gradients: under conditions where matrix dicarboxylate levels dominate, net dicarboxylate efflux is coupled to phosphate influx, whereas under phosphate-rich conditions, net phosphate efflux can be coupled to dicarboxylate uptake. Importantly, the cycle is fully reversible, so transport can proceed in either direction depending on the prevailing gradients, ensuring thermodynamic consistency and adaptability to changing metabolic demands [1]. Experimentally, the dicarboxylate carrier can support both heteroexchange and homoexchange among available substrates; in this work, we focus on the dicarboxylate/phosphate exchange mode relevant to the calibration datasets.

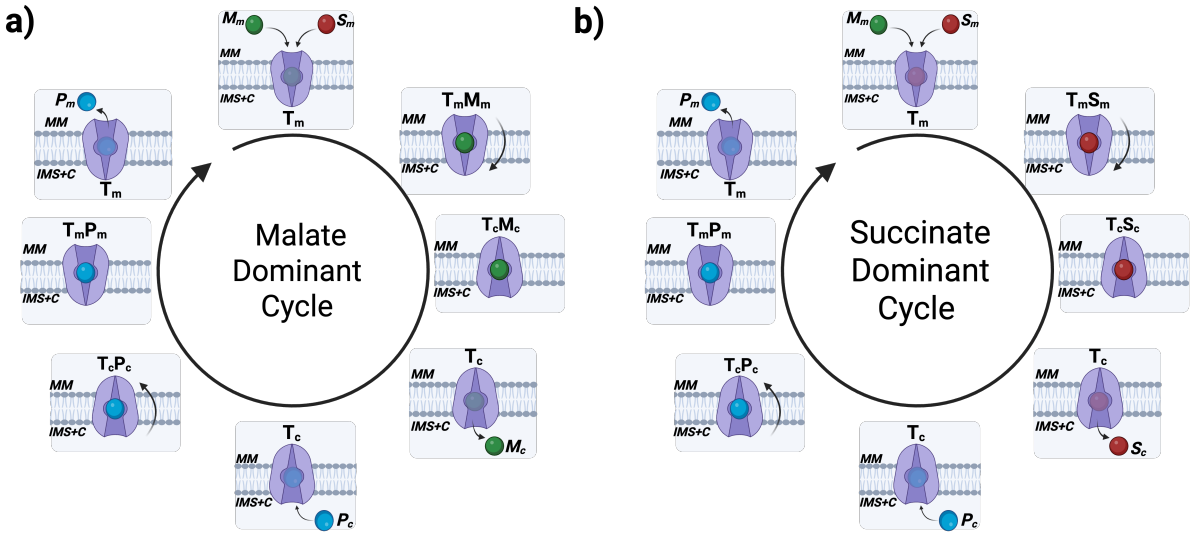

Figure 2: Ping–pong mechanism of the SLC25A10 transporter. The carrier alternates between a matrix-facing conformation (T_m) and an externally facing conformation (T_c), binding and translocating one substrate at a time through a single binding site. The external compartment (c) denotes the combined IMS+cytosol space (IMS+C). **(a)** Malate dominant cycle: malate/phosphate exchange with malate as the dominant transported dicarboxylate. **(b)** Succinate dominant cycle: succinate/phosphate exchange with succinate as the dominant transported dicarboxylate. In both cases, net directionality is not assumed a priori and is determined by the prevailing concentration gradients and reversible kinetics. Created with BioRender.com.

3.1.1 Chemical Reaction Network of the Ping-Pong Mechanism

The reaction begins with the competitive binding of (S_m) and (M_m) to the transporter in its matrix-facing conformation (T_m). Succinate binds to form the complex T_mS, or malate binds to form T_mM. These reversible reactions are characterized by forward (k_1^s, k_1^m) and backward (k_{-1}^s, k_{-1}^m) rate constants:

$$T_m + S_m \underset{k_{-1}^s}{\overset{k_1^s}{\rightleftharpoons}} T_mS, \tag{R1}$$

$$T_m + M_m \underset{k_{-1}^m}{\overset{k_1^m}{\rightleftharpoons}} T_mM. \tag{R2}$$

Once formed, the transporter–substrate complexes undergo conformational changes to expose the binding site to the external side. For succinate and malate, these transitions

occur with rate constants k_c^s, k_{-c}^s and k_c^m, k_{-c}^m, respectively:

$$T_m S \underset{k_{-c}^s}{\overset{k_c^s}{\rightleftharpoons}} T_c S, \tag{R3}$$

$$T_m M \underset{k_{-c}^m}{\overset{k_c^m}{\rightleftharpoons}} T_c M. \tag{R4}$$

At the external side, the transporter releases the bound dicarboxylate, regenerating the free transporter in its external-facing state with release rate constants k_{-3}^s and k_{-3}^m, and corresponding reverse binding rates k_3^s and k_3^m. These reactions leave the transporter in its modified state (T_c), poised for subsequent interactions in the alternating-access cycle:

$$T_c S \underset{k_3^s}{\overset{k_{-3}^s}{\rightleftharpoons}} T_c + S_c, \tag{R5}$$

$$T_c M \underset{k_3^m}{\overset{k_{-3}^m}{\rightleftharpoons}} T_c + M_c. \tag{R6}$$

In its external-facing conformation (T_c), the transporter binds phosphate (P_c) to form the complex $T_c P$. This reversible step is governed by the forward (k_1^p) and backward (k_{-1}^p) rate constants:

$$T_c + P_c \underset{k_{-1}^p}{\overset{k_1^p}{\rightleftharpoons}} T_c P, \tag{R7}$$

The complex then undergoes a conformational change to the matrix-facing state with forward (k_c^p) and backward (k_{-c}^p) rate constants:

$$T_c P \underset{k_{-c}^p}{\overset{k_c^p}{\rightleftharpoons}} T_m P, \tag{R8}$$

after which phosphate is released into the matrix with forward (k_{-3}^p) and reverse (k_3^p) rates. This step regenerates the free transporter (T_m) and completes the transport cycle:

$$T_m P \underset{k_3^p}{\overset{k_{-3}^p}{\rightleftharpoons}} T_m + P_m. \tag{R9}$$

This fully reversible cycle ensures thermodynamic consistency and allows heteroexchange, depending on substrate availability and gradient direction.

3.2 System of Ordinary Differential Equations (ODEs)

The dynamics of the transporter system are described by a set of ordinary differential equations (ODEs) that capture the temporal evolution of transporter states, substrate complexes, and metabolite concentrations. To distinguish between MM and external side, we explicitly include their respective compartment volumes, V_m and V_c, in the model. This ensures that fluxes are appropriately scaled by compartment size and that concentration changes are proportional to the fluxes across compartments. We further assume mass conservation and a spatially homogeneous system, since on the timescales considered, diffusion within each compartment is much faster than the transport processes being modeled. The complete ODE system is provided in Appendix A.

3.3 Model Assumptions and Derivation of Rate Equations for the SLC25A10 Transporter

We assume that the SLC25A10 transporter operates under a symmetric transport mechanism [33, 34, 35]. In this framework, the rate constants governing substrate binding, conformational transitions, and product release are taken to be equal in magnitude for transport in both directions. For example, in the case of succinate, the binding and release rate constants on the matrix side (k_1^s, k_{-1}^s) are assumed identical to the corresponding rate constants on the external side (k_3^s, k_{-3}^s). The same symmetry applies to malate and phosphate. This assumption reduces the number of independent kinetic parameters, thereby simplifying parameter estimation, while also ensuring that the transporter satisfies microscopic reversibility and detailed balance at equilibrium. Under this symmetry, the complete system of ODEs can be further reduced to a compact form, provided in Appendix C.

We further assume that substrate binding and dissociation for the transporter–substrate complexes (T_mS, T_mM, T_mP, T_cS, T_cM, T_cP) occur on a faster timescale than the conformational transitions between matrix-facing and external-facing states [36]. This separation of timescales motivates treating binding and dissociation as quasi-equilibrated relative to the slower conformational changes, enabling a systematic reduction of the full carrier-state model by eliminating the fast binding/unbinding dynamics (see Appendix C).

Accordingly, we apply the rapid equilibrium assumption (REA) [37], which provides a principled way to reduce a mechanistic ping–pong transporter model to closed-form flux expressions while retaining reversibility, saturation, and substrate competition; the full mathematical derivation is provided in Appendix C.

Within this framework, we denote the net flux contributions of succinate, malate, and phosphate by J_{succ}, J_{mal}, and J_{pho}, respectively, and adopt the sign convention that J_{succ} and J_{mal} are positive for net dicarboxylate transport into the matrix, whereas J_{pho} is positive for net phosphate transport into the external compartment (i.e., export from the matrix). Under this convention, J_{succ} is:

$$J_{\text{succ}} = \underbrace{\frac{T_{\max}^s\left(\phi[S_c]-[S_m]\right)}{K_m^s\left(\delta_1+\phi\delta_2\right)}}_{\text{reverse}} - \underbrace{\frac{T_{\max}^s\left([S_m]-\phi[S_c]\right)}{K_m^s\left(\delta_1+\phi\delta_2\right)}}_{\text{forward}}, \tag{1}$$

J_{mal} is:

$$J_{\text{mal}} = \underbrace{\frac{T_{\max}^m\left(\phi[M_c]-[M_m]\right)}{K_m^m\left(\delta_1+\phi\delta_2\right)}}_{\text{reverse}} - \underbrace{\frac{T_{\max}^m\left([M_m]-\phi[M_c]\right)}{K_m^m\left(\delta_1+\phi\delta_2\right)}}_{\text{forward}}, \tag{2}$$

and J_{pho} is:

$$J_{\text{pho}} = \underbrace{\frac{T_{\max}^p\left([P_m]-\phi[P_c]\right)}{K_m^p\left(\delta_1+\phi\delta_2\right)}}_{\text{reverse}} - \underbrace{\frac{T_{\max}^p\left(\phi[P_c]-[P_m]\right)}{K_m^p\left(\delta_1+\phi\delta_2\right)}}_{\text{forward}}, \tag{3}$$

where

$$\phi = \frac{\lambda_1[S_m] + \lambda_2[M_m] + \lambda_3[P_m]}{\lambda_1[S_c] + \lambda_2[M_c] + \lambda_3[P_c]}, \tag{4}$$

The dimensionless ratio ϕ compares the weighted presence of substrates on the two sides of the membrane, thus modulating the extent to which the matrix side pulls the transporter relative to the external side or vice versa. The parameters λ_1, λ_2, and λ_3 are conformational bias weights assigned to succinate, malate, and phosphate, respectively. These quantify how strongly each substrate drives the transporter through its conformational transition once bound. Specifically, λ_1 corresponds to succinate, λ_2 to malate, and λ_3 to phosphate. Biologically, these parameters capture the competitive influence of each substrate at the single binding site of SLC25A10, where succinate, malate, and phosphate compete for access. The λ-weights thus scale the contribution of each substrate to the conformational bias term (ϕ).

It is important to clarify that, in the SLC25A10 ping–pong mechanism, the transport cycle is reversible. Depending on the prevailing concentration gradients, the transporter can initiate the cycle from either the matrix or the external side, and with either a dicarboxylate (succinate or malate) or phosphate as the starting substrate. For instance, if the cycle begins with phosphate, it will be exchanged for a dicarboxylate; conversely, if it begins with a dicarboxylate, it will be exchanged for phosphate. The ratio ϕ, together with the weighting parameters $\lambda_1, \lambda_2, \lambda_3$, governs this directional choice by determining which substrate and which side of the membrane most strongly bias the initiation of the transport cycle.

The terms δ_1 and δ_2 in Eqs. 1–3 are dimensionless partition functions that describe the availability of the transporter for binding on the matrix and external sides, respectively:

$$\delta_1 = 1 + \frac{[S_m]}{K_m^s} + \frac{[M_m]}{K_m^m} + \frac{[P_m]}{K_m^p}, \tag{5}$$

$$\delta_2 = 1 + \frac{[S_c]}{K_m^s} + \frac{[M_c]}{K_m^m} + \frac{[P_c]}{K_m^p}. \tag{6}$$

These include contributions from all three substrates, ensuring that succinate, malate, and phosphate compete for the same single binding site on whichever side of the membrane is exposed. The "1" term corresponds to the unbound transporter, while each substrate term (e.g., $[X_m]/K_m^x$ for the matrix or $[X_c]/K_m^x$ for the external side) represents the relative occupancy weight contributed by substrate X. Here, K_m^s, K_m^m, and K_m^p are Michaelis constants (dissociation constants) representing the binding affinities of the respective substrates to the carrier.

Conceptually, δ_1 and δ_2 have the same form as classical binding polynomials used in enzyme kinetics [38]. Each δ represents the sum of all possible occupancy states on the matrix or external side. Dividing an individual term (e.g. $[S_m]/K_m^s$) by δ gives the probability that the transporter is bound by that substrate. This highlights that our model treats transporter occupancy analogously to enzyme–ligand binding, but extended here to the ping–pong transport mechanism.

In Eqs. 1–3 , $T^s_{\max}$, $T^m_{\max}$, and $T^p_{\max}$ represent the apparent maximal transport capacities for succinate, malate, and phosphate, respectively. Each $T_{\max}$ reflects the product of the amount of active transporter (per gram of protein) and its turnover rate (per second) under saturating substrate conditions, thereby setting the upper bound of the corresponding flux (reported in mmol/s/g protein) in the absence of competitive inhibition or thermodynamic constraints. Differences among $T_{\max}$ values may arise from distinct translocation rates for each substrate or from asymmetries in binding and release kinetics across the two halves of the ping–pong cycle.

Since no leak pathways are considered and SLC25A10 is assumed to have a single binding site, each complete ping–pong cycle exchanges one dicarboxylate for one phosphate. At steady state, the flux through both half-cycles is therefore identical. Using the sign convention defined above, the phosphate flux equals the total dicarboxylate flux:

$$J_{\text{pho}} = J_{\text{succ}} + J_{\text{mal}}. \tag{7}$$

Finally, the overall transport magnitude of the dicarboxylate carrier is expressed as:

$$J_{\text{tot}} = |J_{\text{succ}}| + |J_{\text{mal}}| + |J_{\text{pho}}|. \tag{8}$$

3.4 Reduced Model

Using the approximate flux expressions ($J_{\text{mal}}, J_{\text{succ}}$, and J_{pho}), the full carrier-state ODE system can be reduced to a compartment-level mass-balance model for metabolite concentrations in the MM and the external compartment. Because the transporter fluxes reported in the experimental datasets used to calibrate the model are normalized per gram of protein, the concentration dynamics are written in terms of the compartment volumes per gram of protein, denoted $\tilde{V}_m$ and $\tilde{V}_c$. The reduced model is

$$\frac{d[M_m]}{dt} = \frac{1}{\tilde{V}_m} J_{\text{mal}}, \tag{9}$$

$$\frac{d[M_c]}{dt} = -\frac{1}{\tilde{V}_c} J_{\text{mal}}, \tag{10}$$

$$\frac{d[S_m]}{dt} = \frac{1}{\tilde{V}_m} J_{\text{succ}}, \tag{11}$$

$$\frac{d[S_c]}{dt} = -\frac{1}{\tilde{V}_c} J_{\text{succ}}, \tag{12}$$

$$\frac{d[P_m]}{dt} = -\frac{1}{\tilde{V}_m} J_{\text{pho}}, \tag{13}$$

$$\frac{d[P_c]}{dt} = \frac{1}{\tilde{V}_c} J_{\text{pho}}. \tag{14}$$

Here, positive fluxes are defined as transport into the matrix, such that the corresponding external compartment terms carry the opposite sign. This reduced model preserves mass balance across the membrane while capturing the essential dynamics of succinate, malate, and phosphate exchange through the SLC25A10 transporter.

Table 1: General Model Parameter Values

Parameter	Description	Value	Source
$\tilde{V}_m$	Matrix volume normalized per gram of protein (proteoliposomes)	2.436 $\mathrm{L\,g^{-1}}$	Calculated; see Appendix H
$\tilde{V}_c$	External volume normalized per gram of protein (proteoliposomes)	59.4 $\mathrm{L\,g^{-1}}$	Calculated; see Appendix H
V_m	Matrix compartment volume per assay (proteoliposomes)	3.94 μL	Calculated; see Appendix H
V_c	External compartment volume per assay (proteoliposomes)	96.06 μL	Calculated; see Appendix H
$\tilde{V}_m$	Matrix volume normalized per gram of protein (intact mitochondria)	0.70 $\mu\mathrm{L\,mg^{-1}}$	[39]
$\tilde{V}_c$	External volume normalized per gram of protein (intact mitochondria)	0.49 $\mathrm{L\,g^{-1}}$	Calculated; see Appendix I
V_m	Matrix compartment volume per assay (intact mitochondria)	1.42 μL	Calculated; see Appendix I
V_c	External compartment volume per assay (intact mitochondria)	1.0 mL	Assumed
$[P_m]$	Matrix phosphate concentration	2 mM	[38]
$[S_m]$	Matrix succinate concentration	0.2 mM	[38]
$[M_m]$	Matrix malate concentration	0.2 mM	Assumed

3.5 Calibration Datasets and Experimental Conditions

In this study, we calibrated our mechanistic model using a combination of experimental datasets derived from both reconstituted proteoliposomes and intact rat liver mitochondria. Our study focuses on heteroexchange conditions in which a dicarboxylate (succinate or malate) is exchanged with inorganic phosphate. Consequently, we selected experimental datasets that specifically represent these heteroexchange conditions to constrain the model parameters.

For the core transport kinetics, we used data from reconstituted proteoliposomes reported by Indiveri et al.[23, 40], where the substrate composition on opposing sides of the membrane is strictly controlled. In particular, we selected datasets describing malate uptake against varying internal phosphate and phosphate uptake against varying internal malate (see Fig. 9).

To account for substrate competition and inhibition in a physiological setting, we incorporated data from intact rat liver mitochondria reported by Palmieri et al. [3]. Specifically, the datasets include succinate uptake rates measured over a range of external succinate concentrations, malate uptake rates measured over a range of external malate concentrations, and malate uptake rates measured over a range of external malate concentrations in the presence of external succinate (see Fig. 8). These measurements reveal competitive inhibition between malate and succinate for transport through the carrier and therefore provide key constraints on the competitive-binding component of the model.

Unlike the proteoliposome system, the internal substrate concentrations in intact mitochondria are not explicitly specified in these kinetic datasets. In our model, the external compartment concentrations of succinate, malate, and phosphate (S_c, M_c, P_c) were set according to the experimental conditions in each dataset. The corresponding matrix concentrations (S_m, M_m, P_m) were fixed based on the supporting literature values (see Table 1). Finally, the volumes of the matrix and external compartment (V_m and V_c), together with the corresponding protein-normalized volumes $\tilde{V}_m$ and $\tilde{V}_c$, were fixed and calculated from the experimental sources used in this study (see Appendix H and Appendix I) and are summarized in Table 1.

3.6 Structural Parameter Identifiability Analysis

As the first step of model calibration [41], we analyzed whether the values of all model parameters can, in principle, be determined from perfect, continuous-time, noise-free measurements of the observables, based solely on the model structure and available measure-

ments. Here, observables refer to model outputs that are experimentally measurable, in this case the net fluxes J_{succ}, J_{mal}, and J_{pho}. To this end, we performed a local structural identifiability analysis of the 8-parameter SLC25A10 ping–pong transport model using the STRIKE-GOLDD method [42]. For this analysis, we used the reduced ODE model.

3.7 Local Sensitivity Analysis

To estimate the local sensitivity coefficients (LSCs), we compute the partial derivative of the flux with respect to a given parameter θ. This describes how small perturbations in that parameter change the flux. Each parameter θ_i in $\tilde{\theta}$ was perturbed individually by a factor $\varepsilon = 0.1$ (a 10% change), while keeping all other parameters fixed. The partial derivative was approximated using the central finite difference:

$$\frac{\partial J}{\partial \theta_i} \approx \frac{J(\theta_i\,(1+\varepsilon)) - J(\theta_i\,(1-\varepsilon))}{2\,\varepsilon\,\theta_i}. \tag{15}$$

Since raw sensitivities depend on the units and magnitudes of both the flux and the parameter, they are not directly comparable across parameters. To address this, we use normalized LSCs. In this normalization, each sensitivity is scaled relative to both the corresponding parameter value and the flux value. The normalized LSC is then defined as:

$$\text{LSC}_i = \frac{\theta_i}{J}\frac{\partial J}{\partial \theta_i} \approx \frac{J(\theta_i\,(1+\varepsilon)) - J(\theta_i\,(1-\varepsilon))}{2\,\varepsilon\,J}. \tag{16}$$

This renders the coefficients dimensionless, allowing the influence of parameters with different units (e.g. maximum transport rates versus dissociation constants) to be compared on the same scale. Intuitively, the normalized LSC represents the percentage change in a flux that results from a one percent change in a given parameter.

As a numerical accuracy check for the finite-difference sensitivities used throughout this work, we also compute the same local sensitivity coefficients using the complex-step method [43], which avoids subtractive cancellation and typically provides near machine-precision derivatives for analytic model evaluations.

3.8 Bayesian Framework for Parameter Estimation

To estimate the unknown parameters and quantify their uncertainties in the SLC25A10 transporter flux equations, we apply Bayesian inference using the Metropolis–Hastings Markov Chain Monte Carlo (MCMC) algorithm [44, 45]. The parameter vector $\tilde{\theta}$ is defined as

$$\tilde{\theta} = \left[T^s_{\text{max}},\ \ T^m_{\text{max}},\ \ K^s_m,\ \ K^m_m,\ \ K^p_m,\ \ \lambda_{21},\ \ \lambda_{31}\right]^{\mathsf{T}}$$

Phosphate flux is not independently parameterized, as it is constrained by the cyclic balance equation (7). Therefore, we do not include T^p_{max} in the parameter vector.

According to Bayes' theorem, the conditional probability of the parameter vector $\tilde{\theta}$ given the measured data Y, known as the posterior distribution, is expressed as:

$$p(\tilde{\theta} \mid Y) = \frac{p(Y \mid \tilde{\theta})\,p(\tilde{\theta})}{p(Y)} \tag{17}$$

where $p(\tilde{\theta})$ is the prior distribution of the unknown parameters, encoding available knowledge or plausible ranges before considering the experimental data. $p(Y \mid \tilde{\theta})$ is the likelihood function, describing the probability of observing the experimental data Y given a specific parameter set $\tilde{\theta}$. $p(Y)$ is the marginal likelihood (or evidence), acting as a normalizing constant ensuring $\int p(\tilde{\theta} \mid Y)\, d\tilde{\theta} = 1$. In practice, $p(Y)$ is difficult to compute directly, so inference is carried out up to a proportionality constant:

$$p(\tilde{\theta} \mid Y) \propto p(Y \mid \tilde{\theta})\, p(\tilde{\theta}). \tag{18}$$

3.8.1 Likelihood Function

The results of our SLC25A10 model are always subject to error because it is only an approximation of the underlying transport process. If we consider the experimental measurements, Y, as the observation of the transport fluxes, then the model predictions with parameters $\tilde{\theta}$, denoted $F(\tilde{\theta})$, can be expressed as

$$Y_i = F_i(\tilde{\theta}) + \varepsilon_i, \tag{19}$$

where ε_i represents the error in the model and i indexes the experimental data points. The error is assumed to follow an independent Gaussian distribution with zero mean and constant variance σ^2. Under these assumptions, the likelihood function for the data Y given the parameters $\tilde{\theta}$ and variance σ^2 can be written as

$$p(Y \mid \tilde{\theta}, \sigma^2) = \prod_{i=1}^{n} \frac{1}{\sqrt{2\pi\sigma^2}} \exp\left[-\frac{\left(Y_i - F_i(\tilde{\theta})\right)^2}{2\sigma^2} \right], \tag{20}$$

where n is the total number of flux measurements across all experiments.

Since the error variance σ^2 is unknown, it is treated as an additional parameter to be inferred jointly with $\tilde{\theta}$ in the Bayesian framework. From this point onward, we introduce the overall parameter vector $\tilde{\xi}$, defined as:

$$\tilde{\xi} = \begin{bmatrix} \theta_1, & \theta_2, & \theta_3, & \theta_4, & \theta_5, & \theta_6, & \theta_7, & \sigma^2 \end{bmatrix}^{\mathsf{T}}, \tag{21}$$

To simplify our computations, we take the natural logarithm of the likelihood function. The log-likelihood is then proportional to the sum of squared residuals between the measured and model-predicted fluxes:

$$\begin{aligned} \ln p(Y \mid \tilde{\xi}) &= \sum_{i=1}^{n} \left[-\frac{1}{2} \ln(2\pi\sigma^2) - \frac{(Y_i - F_i(\tilde{\theta}))^2}{2\sigma^2} \right] \\ &= -\frac{n}{2} \ln(2\pi\sigma^2) - \frac{1}{2\sigma^2} \sum_{i=1}^{n} (Y_i - F_i(\tilde{\theta}))^2 \end{aligned} \tag{22}$$

We emphasise that our assumption of independent, identically distributed Gaussian errors is not intended to fully capture the complexity of experimental uncertainty or model–data discrepancy. Instead, we regard this as a proof of concept choice that enables a tractable Bayesian calibration of a mechanistic model grounded in real physiological dynamics. The Gaussian assumption allows for closed form likelihoods and efficient computation, which is essential at this stage.

3.8.2 Prior

The prior distributions of the unknown parameters $\tilde{\xi}$ were assigned based on the results of the structural identifiability analysis and available experimental data.

The structural identifiability analysis indicated that $T^s_{\max}$, $T^m_{\max}$, K^s_m, K^m_m, and K^p_m are structurally unidentifiable. To address this, we adopted their values from the literature, as summarized in Table 2. For these parameters, we assigned Gaussian priors with means and standard deviations set to the reported experimental estimates, thereby constraining them to physiologically realistic ranges while allowing for uncertainty:

$$\tilde{\xi}_i \sim \mathcal{N}(\mu_{\tilde{\xi}_i}, \tau^2_{\tilde{\xi}_i}), \quad i = 1, 2, 3, 4, 5, \tag{23}$$

with probability density function:

$$p(\tilde{\xi}_i) = \frac{1}{\sqrt{2\pi\tau^2_{\tilde{\xi}_i}}} \exp\left(-\frac{(\tilde{\xi}_i - \mu_{\tilde{\xi}_i})^2}{2\tau^2_{\tilde{\xi}_i}}\right). \tag{24}$$

The parameters λ_{21} and λ_{31} were found to be structurally identifiable. We therefore assigned them independent uniform priors over a wide positive range, with lower bound l and upper bound u, reflecting the absence of strong prior constraints:

$$\tilde{\xi}_i \sim \mathcal{U}(l,\, u), \quad i = 6, 7, \tag{25}$$

with probability density function:

$$p(\tilde{\xi}_i) = \frac{1}{u - l}, \quad \tilde{\xi}_i \in [l, u]. \tag{26}$$

The observation error variance σ^2 was assigned an inverse-gamma prior with shape parameter α and scale parameter β:

$$\tilde{\xi}_i \sim \text{Inv-Gamma}(\alpha,\, \beta), \quad i = 8, \tag{27}$$

with probability density function:

$$p(\tilde{\xi}_i) = \frac{\beta^\alpha}{\Gamma(\alpha)} (\tilde{\xi}^2_i)^{-\alpha-1} \exp\left(-\frac{\beta}{\tilde{\xi}^2_i}\right), \quad \tilde{\xi}^2_i > 0. \tag{28}$$

Assuming a priori independence, the joint prior distribution factorizes as:

$$p(\tilde{\xi}) = \prod_{i=1}^{8} p(\tilde{\xi}_i), \tag{29}$$

with each term defined according to the distributional choices described above. To ensure positivity and simplify computations, we used the logarithm of the prior distribution:

$$\ln p(\tilde{\xi}) = \sum_{i=1}^{8} \ln p(\tilde{\xi}_i). \tag{30}$$

Table 2: Literature values of kinetic parameters for isolated intact mitochondria, with mean, standard deviation, 95% confidence intervals, and references.

Parameter	Mean	Std	95% CI (Low–High)	Reference
K_m^s (mM)	1.17	0.10	0.97 – 1.37	[3]
K_m^m (mM)	0.23	0.02	0.19 – 0.27	[3]
K_m^p (mM)	0.93	0.40	0.13 – 1.73	[40, 17]
$T_{\max}^s$ (μmol/min/g)	64.2	5.1	54.0 – 74.4	[3]
$T_{\max}^m$ (μmol/min/g)	69.4	5.6	58.4 – 80.6	[3]

3.8.3 Posterior Distribution

Given the likelihood function $p(Y \mid \tilde{\xi})$ in Eq. (20) and the independent priors $p(\tilde{\xi})$ defined in Eq. (29), the posterior distribution of the parameter vector is obtained using Bayes' theorem (Eq. (18)).

For computational convenience and to ensure positivity, we work with the logarithm of the posterior distribution. Combining Eq. (22) and Eq. (30), the log-posterior can be written as:

$$\ln p(\tilde{\xi} \mid Y) \propto \ln p(\tilde{\xi}) + \ln p(Y \mid \tilde{\xi}). \tag{31}$$

3.8.4 Markov Chain Monte Carlo (MCMC) Method

Direct analytical evaluation of the posterior distribution $p(\tilde{\xi} \,|\, Y)$ is generally intractable due to the complexity of the nonlinear transporter model. Therefore, we employed a Markov Chain Monte Carlo (MCMC) approach to generate samples from the posterior distribution and estimate the kinetic parameters [44].

We used the Metropolis–Hastings algorithm to construct the Markov chain $\{\tilde{\xi}^{(j)} : j = 0, 1, 2, \dots\}$, where j denotes the sampling iteration. At each iteration j, a new candidate $\tilde{\xi}^*$ was generated using a log-normal random walk proposal:

$$\ln \tilde{\xi}^* = \ln \tilde{\xi}^{(j)} + z\eta, \quad \eta \sim \mathcal{N}(0, 1), \tag{32}$$

which ensures positivity of all parameters. Here, z is the step size, set to $z = 0.01$ in our calculations.

The acceptance probability is given by:

$$\alpha\Big(\tilde{\xi}^{(j)}, \tilde{\xi}^*\Big) = \min\left[1, \frac{p(Y \mid \tilde{\xi}^*)\, p(\tilde{\xi}^*)\, q(\tilde{\xi}^{(j)} \mid \tilde{\xi}^*)}{p(Y \mid \tilde{\xi}^{(j)})\, p(\tilde{\xi}^{(j)})\, q(\tilde{\xi}^* \mid \tilde{\xi}^{(j)})}\right], \tag{33}$$

where $q(\cdot|\cdot)$ denotes the log-normal proposal density. Since the log-normal proposal distribution is asymmetric, the Hastings correction (the ratio of proposal densities) is included to guarantee detailed balance and ensure that the posterior distribution remains the stationary distribution of the chain [45].

If $\alpha \geq r$, where $r \sim \mathcal{U}(0, 1)$, the candidate is accepted:

$$\tilde{\xi}^{(j+1)} = \tilde{\xi}^*, \tag{34}$$

otherwise, the current state is retained:

$$\tilde{\xi}^{(j+1)} = \tilde{\xi}^{(j)}. \tag{35}$$

At each iteration, the fluxes J_{succ}, J_{mal}, and J_{pho} were computed using the transporter flux equations. We used all three datasets adopted from [3], which are described above. These datasets together comprise $n = 18$ data points and were used as the observation vector Y.

3.8.5 Estimation of Monte Carlo Standard Error (MCSE)

After generating a sequence of samples from the posterior distribution using the Metropolis–Hastings MCMC algorithm, we used these samples to estimate posterior quantities such as the mean, median, and credible intervals. However, because the number of samples is finite and they are often correlated due to the Markov chain structure;each sample depends on the previous one [46, 47, 48, 49], these estimates have some variability. The MCSE quantifies the error in an MCMC estimate (e.g. the posterior mean) that arises from sampling variability.

To calculate the MCSE of a kinetic parameter of interest θ_i from a chain of N samples, we first compute the sample mean:

$$\hat{\theta} = \frac{1}{N} \sum_{i=1}^{N} \theta_i. \tag{36}$$

We then compute the sample variance of the MCMC samples:

$$\Sigma^2 = \frac{1}{N-1} \sum_{i=1}^{N} (\theta_i - \hat{\theta})^2, \tag{37}$$

which represents the variability of the parameter values in the chain.

Since MCMC samples are correlated, the effective sample size (N_{eff}) is typically smaller than N. To estimate N_{eff}, we compute the autocorrelation at lag k, denoted ρ_k, using the autocorrelation function (ACF) [46]:

$$\rho_k \approx \frac{\sum_{i=1}^{N-k} (\theta_i - \hat{\theta})(\theta_{i+k} - \hat{\theta})}{\sum_{i=1}^{N} (\theta_i - \hat{\theta})^2}. \tag{38}$$

The effective sample size is then estimated as:

$$N_{\text{eff}} = \frac{N}{1 + 2\sum_{k=1}^{\infty} \rho_k}. \tag{39}$$

In practice, the sum is truncated at a lag where ρ_k becomes negligible [49].

Finally, the MCSE for the posterior mean is given by:

$$\text{MCSE} = \sqrt{\frac{\Sigma^2}{N_{\text{eff}}}}.$$

This formula accounts for correlation among the MCMC samples. A small MCSE indicates that the MCMC estimate is precise, meaning that the chain length is sufficient to approximate the true posterior statistic. In this study, we aimed for an MCSE smaller than 10% of the posterior standard deviation (Σ), which reflects the intrinsic uncertainty of the parameter under the posterior distribution. While we cannot guarantee the correctness of the finite set of N samples, by calculating the MCSE-to-SD ratio and targeting values below 0.10, we empirically assessed the convergence and reliability of the chains.

3.8.6 Estimation of $\hat{R}$ Statistic

To assess the convergence of our chains to the equilibrium or stationary distribution, we estimate the Gelman–Rubin statistic, $\hat{R}$ [50, 51]. This diagnostic evaluates whether independently initialized chains target the same stationary posterior. It does so by comparing between-chain to within-chain variability for each parameter.

Suppose there are Ω chains, each with N draws for a parameter θ. Let the draws from chain $\omega \in \Omega$ be denoted $\theta_{\omega,i}$, where i indexes the samples. The chain mean for chain ω is

$$\hat{\theta}_\omega = \frac{1}{N} \sum_{i=1}^{N} \theta_{\omega,i}. \tag{40}$$

The overall mean across all chains is

$$\bar{\theta} = \frac{1}{\Omega} \sum_{\omega=1}^{\Omega} \hat{\theta}_\omega. \tag{41}$$

The between-chain variance is

$$B = \frac{N}{\Omega - 1} \sum_{\omega=1}^{\Omega} \left(\hat{\theta}_\omega - \bar{\theta} \right)^2. \tag{42}$$

The within-chain variance for each chain is

$$\Sigma_\omega^2 = \frac{1}{N-1} \sum_{i=1}^{N} \left(\theta_{\omega,i} - \hat{\theta}_\omega \right)^2, \tag{43}$$

and the average within-chain variance is

$$W = \frac{1}{\Omega} \sum_{\omega=1}^{\Omega} \Sigma_\omega^2. \tag{44}$$

The pooled variance estimator is defined as

$$\Psi = \frac{N-1}{N} W + \frac{1}{N} B, \tag{45}$$

and the Gelman–Rubin statistic is then computed as

$$\hat{R} = \sqrt{\frac{\Psi}{W}}. \tag{46}$$

In practice, values of $\hat{R} \approx 1$ (e.g., < 1.1) indicate acceptable convergence, whereas $\hat{R} > 1.1$ suggests potential convergence issues [50]. In this study, we require $\hat{R} < 1.1$ for all parameters.

3.9 Gibbs Free Energy Calculations for SLC25A10 Antiporter

The Gibbs free energy change (ΔG) for the electroneutral antiport process mediated by the SLC25A10 transporter, which exchanges dicarboxylates (succinate or malate) with phosphate across the mitochondrial membrane, is calculated for the following reactions:

$$\begin{aligned} \mathrm{S_m} + \mathrm{P_c} &\rightleftharpoons \mathrm{S_c} + \mathrm{P_m}, \\ \mathrm{M_m} + \mathrm{P_c} &\rightleftharpoons \mathrm{M_c} + \mathrm{P_m}, \end{aligned}$$

following the methodology of Jol et al. (2010) [52]. The standard chemical-thermodynamics expression for the Gibbs free energy change of a reaction for the above transport processes is:

$$\Delta G = \sum_{i \in \text{transported}} w_i \Delta_f G_i^0 + RT \sum_{i \in \text{transported}} w_i \ln C_i. \tag{47}$$

Here, w_i are the stoichiometric coefficients for the transported species (e.g. S_m, P_m, S_c, P_c), with values of -1 for reactants in the matrix side and $+1$ for products in the external side. For transported species i, $\Delta_f G_i^0$ denotes the Gibbs energy of formation, and C_i denotes the concentration. Moreover, R is the gas constant, T is the absolute temperature.

For succinate exchange, this yields

$$\begin{aligned} \Delta G = &\left(\Delta_f G^\circ_{\mathrm{S}_c} + \Delta_f G^\circ_{\mathrm{P}_m} - \Delta_f G^\circ_{\mathrm{S}_m} - \Delta_f G^\circ_{\mathrm{P}_c}\right) \\ &+ RT\left(\ln C_{\mathrm{S}_c} + \ln C_{\mathrm{P}_m} - \ln C_{\mathrm{S}_m} - \ln C_{\mathrm{P}_c}\right). \end{aligned} \tag{48}$$

Using our notation, with $[S_m], [S_c], [P_m], [P_c]$ in place of concentrations C, we write

$$\Delta G = \left(\Delta_f G^\circ_{\mathrm{S}_c} + \Delta_f G^\circ_{\mathrm{P}_m} - \Delta_f G^\circ_{\mathrm{S}_m} - \Delta_f G^\circ_{\mathrm{P}_c}\right) + RT \ln\left(\frac{[S_c]\,[P_m]}{[S_m]\,[P_c]}\right). \tag{49}$$

Similarly, for malate exchange,

$$\Delta G = \left(\Delta_f G^\circ_{\mathrm{M}_c} + \Delta_f G^\circ_{\mathrm{P}_m} - \Delta_f G^\circ_{\mathrm{M}_m} - \Delta_f G^\circ_{\mathrm{P}_c}\right) + RT \ln\left(\frac{[M_c]\,[P_m]}{[M_m]\,[P_c]}\right). \tag{50}$$

At thermodynamic equilibrium, $\Delta G = 0$, giving

$$\frac{[S_c^{eq}]\,[P_m^{eq}]}{[S_m^{eq}]\,[P_c^{eq}]} = K_{eq}, \tag{51}$$

Table 3: Thermodynamic parameters and constants for Gibbs free energy calculations of SLC25A10 antiport reactions.

Species / Constant	**Charge (z)**	**$\Delta_f G^\circ$ (kJ/mol)**	**Stoichiometry (s_i)**	**Reference**
External Malate (M_c)	-2	-842.66	$+1$	[17, 53]
Matrix Malate (M_m)	-2	-842.66	-1	[17, 53]
External Succinate (S_c)	-2	-690.44	$+1$	[52, 53]
Matrix Succinate (S_m)	-2	-690.44	-1	[52, 53]
External Phosphate (P_c)	-2	-1069.1	-1	[52, 53]
Matrix Phosphate (P_m)	-2	-1069.1	$+1$	[52, 53]
Gas Constant (R)	–	0.008314 kJ/K	–	[52]
Temperature (T)	–	298.15 K (25 °C)	–	[52]

where $[S_m^{eq}]$, $[P_m^{eq}]$, $[S_c^{eq}]$, and $[P_c^{eq}]$ are the equilibrium concentrations of matrix and external succinate and phosphate, respectively. The equilibrium constant (K_{eq})) is given by

$$K_{eq} = \exp\left(-\frac{\Delta_f G^\circ_{rxn}}{RT}\right), \tag{52}$$

where

$$\Delta_f G^\circ_{rxn} = \Delta_f G^\circ_{\mathrm{S}_c} + \Delta_f G^\circ_{\mathrm{P}_m} - \Delta_f G^\circ_{\mathrm{S}_m} - \Delta_f G^\circ_{\mathrm{P}_c} \tag{53}$$

is the standard Gibbs free energy change of the reaction. Since the species are chemically identical across compartments, $\Delta_f G^\circ_{rxn}$ is zero, and the equilibrium distribution is dominated by the concentration ratios.

From conservation of mass in each metabolite pool, the analytical equilibrium concentrations can be written as explicit functions of initial metabolite concentrations. Let the initial mitochondrial concentrations for succinate, and phosphate be $[S_m^0]$, and $[P_m^0]$, respectively, and let the external initial concentrations be $[S_c^0]$, and $[P_c^0]$, respectively. Then, the resulting closed-form equilibrium concentrations are

$$[S_\mathrm{c}^\mathrm{eq}] = [S_\mathrm{c}^0] + \frac{[P_\mathrm{c}^0][S_m^0] - [P_m^0][S_\mathrm{c}^0]}{[P_m^0] + [S_m^0] + \frac{V_\mathrm{c}}{V_m}([P_\mathrm{c}^0] + [S_\mathrm{c}^0])}, \tag{54}$$

$$[S_m^\mathrm{eq}] = [S_m^0] - \frac{\frac{V_\mathrm{c}}{V_m}([P_\mathrm{c}^0][S_m^0] - [P_m^0][S_\mathrm{c}^0])}{[P_m^0] + [S_m^0] + \frac{V_\mathrm{c}}{V_m}([P_\mathrm{c}^0] + [S_\mathrm{c}^0])}, \tag{55}$$

$$[P_\mathrm{c}^\mathrm{eq}] = [P_\mathrm{c}^0] - \frac{[P_\mathrm{c}^0][S_m^0] - [P_m^0][S_\mathrm{c}^0]}{[P_m^0] + [S_m^0] + \frac{V_\mathrm{c}}{V_m}([P_\mathrm{c}^0] + [S_\mathrm{c}^0])}, \tag{56}$$

$$[P_m^\mathrm{eq}] = [P_m^0] + \frac{\frac{V_\mathrm{c}}{V_m}([P_\mathrm{c}^0][S_m^0] - [P_m^0][S_\mathrm{c}^0])}{[P_m^0] + [S_m^0] + \frac{V_\mathrm{c}}{V_m}([P_\mathrm{c}^0] + [S_\mathrm{c}^0])}. \tag{57}$$

These closed-form expressions allow direct analytical validation of the simulated equilibrium state of the reduced transporter model against thermodynamic constraints. The full derivation of these expressions is provided in Appendix G.

3.10 Simulating the Effect of Succinate Accumulation in the Mitochondrial Matrix on the Dynamics of the SLC25A10 Transporter

To simulate succinate accumulation, we incorporated a source and a sink into our transporter model. Specifically, we added the flux of succinyl-CoA synthetase (SCAS) as a source of succinate and the flux of succinate dehydrogenase (SDH) as a sink for succinate.

SDH is a mitochondrial enzyme that functions in both the tricarboxylic acid (TCA) cycle and the electron transport chain (ETC). It catalyzes the oxidation of succinate to fumarate (F_m) while reducing ubiquinone (Q_m) to ubiquinol ($QH_{2,m}$). This reaction depletes the mitochondrial succinate pool, thereby affecting the fluxes and dynamic behavior of the SLC25A10 transporter, which exchanges succinate with phosphate. The electron transfer reactions catalyzed by SDH (Complex II) are:

$$\mathrm{S}_m + \mathrm{FAD}_m \rightleftharpoons \mathrm{F}_m + \mathrm{FADH}_{2,m} \tag{R10}$$

$$\mathrm{FADH}_{2,m} + \mathrm{Q}_m \rightleftharpoons \mathrm{FAD}_m + \mathrm{QH}_{2,m} \tag{R11}$$

which can be lumped into a single overall reaction:

$$\mathrm{S}_m + \mathrm{Q}_m \rightleftharpoons \mathrm{F}_m + \mathrm{QH}_{2,m}, \tag{R12}$$

where S_m denotes mitochondrial succinate, F_m fumarate, Q_m ubiquinone, and $QH_{2,m}$ ubiquinol. The flux of this reaction, J_{SDH}, was adopted from Sadri et al. [17]. The complete flux equation, parameter values, and assumptions are provided in Appendix Appendix E.

SCAS is another enzyme of the TCA cycle that catalyzes the reversible conversion of succinyl-CoA into succinate. This reaction simultaneously produces a nucleoside triphosphate (typically GTP) from mitochondrial phosphate (P_m) and GDP, thereby increasing mitochondrial succinate levels while depleting phosphate:

$$\text{Succinyl-CoA}_m + \mathrm{GDP}_m + \mathrm{P}_m \rightleftharpoons \mathrm{S}_m + \mathrm{GTP}_m + \mathrm{CoA}_m + \mathrm{H}^+_m. \tag{R13}$$

The flux of this enzyme, J_{SCAS}, was also taken from Sadri et al. [17]; full details are provided in Appendix F.

We integrated these fluxes into the dynamic equations governing the SLC25A10 transporter: J_{SDH} was included as a sink (negative term) and J_{SCAS} as a source (positive term). High SDH activity results in rapid succinate depletion, whereas high SCAS activity leads to succinate accumulation and phosphate consumption.

We simulated two scenarios: SDH-active (normal mitochondria), where succinate is oxidized by SDH, and SDH-deficient, where SDH is knockdown. The modified reduced

ODE system for the SDH-active condition is:

$$\frac{d[M_m]}{dt} = \frac{1}{\tilde{V}_m} J_{\text{mal}}, \tag{50.1}$$

$$\frac{d[M_c]}{dt} = -\frac{1}{\tilde{V}_c} J_{\text{mal}}, \tag{50.2}$$

$$\frac{d[S_m]}{dt} = \frac{1}{\tilde{V}_m}\Big(J_{\text{succ}} - J_{\text{SDH}} + J_{\text{SCAS}}\Big), \tag{50.3}$$

$$\frac{d[S_c]}{dt} = -\frac{1}{\tilde{V}_c} J_{\text{succ}}, \tag{50.4}$$

$$\frac{d[P_m]}{dt} = \frac{1}{\tilde{V}_m}\Big(-J_{\text{pho}} - J_{\text{SCAS}}\Big), \tag{50.5}$$

$$\frac{d[P_c]}{dt} = \frac{1}{\tilde{V}_c} J_{\text{pho}}. \tag{50.6}$$

For the SDH-deficient case, we set $J_{\text{SDH}} = 0$.

4 Results

4.1 Structural Identifiability Analysis of the SLC25A10 Transporter Model

The local structural identifiability analysis indicates that the system is not fully observable and that not all parameters are structurally identifiable under the current model formulation and output configuration. Two main structural reasons explain this loss of identifiability are: Scaling symmetries between T^x_{max} and K^x_m, for x substrate and Relative nature of λ_1, λ_2, and λ_3 parameters.

In each flux equation, T^x_{max} and K^x_m appear together as the ratio T^x_{max}/K^x_m because the denominator is of the form $K^x_m(\delta_1 + \phi\,\delta_2)$. Multiplying T^x_{max} by a constant factor and K^x_m by the same factor leaves the flux unchanged, making them inseparable without additional constraints or data.

In the ϕ expression, the λ values act only as proportional weights on succinate, malate, and phosphate concentrations. Scaling all λ values by a common constant leaves both ϕ unchanged. As a result, the absolute values of λ_1, λ_2, and λ_3 cannot be uniquely determined—only their ratios, and thus the relative weighting between substrates, are structurally identifiable.

To address the symmetry in the λ parameters, we reparameterized the model by introducing the ratios $\lambda_{21} = \lambda_2/\lambda_1$ and $\lambda_{31} = \lambda_3/\lambda_1$ as new parameters, replacing λ_1, λ_2, and λ_3 in the ϕ term. These ratios represent relative weightings of malate (λ_2) and phosphate (λ_3) with respect to succinate (λ_1) in determining the transporter's conformational bias term (ϕ).

A second STRIKE-GOLDD analysis of the reparameterized model showed that λ_{21} and λ_{31} became structurally identifiable. However, the transport capacities T^x_{max} and the Michaelis constants K^x_m for each substrate remained structurally unidentifiable due to their appearance only as ratios T^x_{max}/K^x_m in the flux equations.

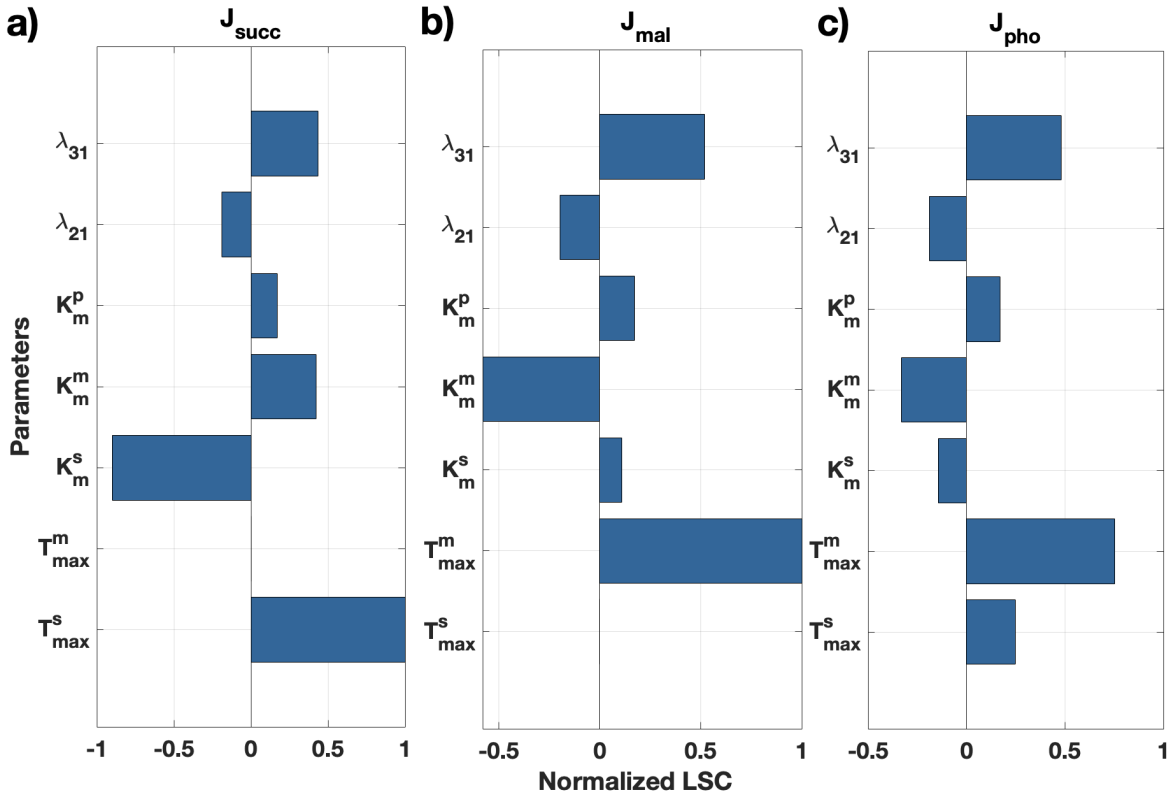

Figure 3: Normalized Local sensitivity coefficients (LSCs) for (a) succinate flux J_{succ}, (b) malate flux J_{mal}, and (c) phosphate flux J_{pho} with respect to model parameters. Here, "normalized" means that each sensitivity is scaled relative to both the value of the parameter and the corresponding flux, making the coefficients dimensionless. This allows the influence of parameters with different units and magnitudes to be compared on the same scale. Positive values indicate that increasing a parameter increases the fluxes, whereas negative values imply the opposite.

To fully resolve the identifiability issue, we adopted literature values for T^x_{max} and K^x_m for succinate and malate from Palmieri et al. [3] and for phosphate from Indiveri et al. [40] and Sadri et al. [17]. This parameter fixing removed the scaling symmetry between T^x_{max} and K^x_m, rendering the remaining free parameters structurally identifiable in the STRIKE-GOLDD analysis.

4.2 Local Sensitivity Analysis

Following the structural identifiability analysis and reparameterization of the model, we investigated how the kinetic parameters influence the dynamics of the SLC25A10 transporter. To this end, we computed normalized local sensitivity coefficients (LSCs) for three key output fluxes: succinate (J_{succ}), malate (J_{mal}), and phosphate (J_{pho}). Positive values indicate that an increase in the parameter enhances the flux, while negative values indicate suppression.

The analysis was performed on the reparameterized transporter model with seven kinetic parameters: the maximum transport rates for succinate (T^s_{max}) and malate (T^m_{max}); the dissociation constants for succinate (K^s_m), malate (K^m_m), and phosphate (K^p_m); and the coupling ratios λ_{21} and λ_{31}. For phosphate, we applied the cyclic balance constraint

from Eq. (7), so no independent phosphate transport capacity was included.

Parameter values were initialized according to Table 1. External compartment metabolite concentrations were set to match the experimental data of Palmieri et al. [3], specifically the dataset measuring malate uptake in the presence of 0.5 mM external succinate. This condition provides a direct test of competitive inhibition. Here, the external malate concentration was fixed at 0.9077 mM, external succinate at 0.5 mM, and other conditions matched the experimental setup.

We compare finite-difference and complex-step sensitivity coefficients as a numerical accuracy check by reporting the absolute and relative differences between the two estimates (see Appendix J). The results show close agreement across all parameters (maximum discrepancy $< 8 \times 10^{-4}$), supporting the numerical reliability of our finite-difference implementation for the chosen perturbation size.

For the succinate flux (Fig. 3a), the dominant positive driver is the maximal succinate transport capacity $T^s_{\max}$, as expected for a capacity-limited contribution. The strongest negative sensitivity is to K^s_m, indicating that increasing K^s_m (i.e., lowering succinate affinity) substantially reduces J_{succ}. In addition, λ_{31} has a clear positive influence, consistent with stronger phosphate–succinate coupling bias increasing succinate turnover. By contrast, λ_{21} is negative, implying that increasing malate weighting suppresses succinate flux through competition. Notably, K^m_m appears with a positive sensitivity: increasing K^m_m (i.e., weakening malate affinity) alleviates competition at the binding site and thereby increases succinate flux. Overall, J_{succ} is governed primarily by intrinsic succinate capacity and affinity ($T^s_{\max}, K^s_m$), with coupling (λ_{31}) and competitive effects (λ_{21}, K^m_m) providing secondary modulation.

For the malate flux (Fig. 3b), the largest positive sensitivity is to $T^m_{\max}$, indicating that malate exchange is strongly capacity-controlled in this regime. The dominant negative contribution comes from K^m_m, showing that reduced malate affinity (higher K^m_m) substantially decreases J_{mal}. The coupling weight λ_{31} also contributes positively, indicating that phosphate-related bias promotes malate turnover in the antiport cycle, while λ_{21} contributes negatively, consistent with its role as a competitive weighting in the conformational-bias terms. Other parameters have comparatively smaller effects.

For the phosphate flux (Fig. 3c), $T^m_{\max}$ again emerges as the strongest positive driver, reflecting the obligatory coupling between phosphate exchange and dicarboxylate turnover in the ping–pong mechanism. The next largest contributions are a positive sensitivity to λ_{31} and a negative sensitivity to K^m_m, reinforcing that phosphate flux is tightly linked to malate-side saturation/competition in these conditions. In contrast to the original interpretation, $T^s_{\max}$ now shows a non-negligible positive influence on J_{pho}, consistent with succinate exchange contributing to overall carrier cycling and thus to phosphate turnover.

4.3 Bayesian Parameter Estimation

Following the structural identifiability and local sensitivity analyses, we employed a Bayesian inference framework to quantitatively estimate the kinetic parameters and assess the uncertainty of the SLC25A10 transporter model. The model was then validated against experimental datasets from both reconstituted proteoliposomes and intact rat liver mitochondria.

We ran 1,000,000 Metropolis-Hastings MCMC iterations, discarding the first 10,000 as burn-in to reduce dependence on the initial guess. Posterior means, standard deviations,

modes, and 95% credible intervals are computed from the retained samples for all parameters, including σ^2, for each uptake-assay dataset. A statistical summary of the posterior parameter estimates for the intact mitochondria calibration is provided in Table 4. The corresponding posterior summary for the proteoliposome calibration is reported separately in Table 5.

For convergence diagnostics, we ran four independent MCMC chains initialized from dispersed starting values, each for 1,000,000 iterations with the first 10,000 discarded as burn-in for both uptake assays calibration. For each parameter, we computed the split-$\hat{R}$ statistic using the post–burn-in draws across chains. All parameters satisfied $\hat{R} < 1.1$. Table 6 shows the MCMC diagnostic for intact mitochondria assays, with values close to 1.0 (maximum $\hat{R} = 1.0288$). Table 7 shows the MCMC diagnostic for proteoliposomes assays, with values very close to 1.0 (maximum $\hat{R} = 1.0039$). Both tables indicate good mixing and strong evidence of convergence to a common stationary posterior. The Metropolis–Hastings transition kernel used in our sampler satisfies a detailed balance with respect to the posterior target by construction; the small $\hat{R}$ values confirm that the chains reached this stationary regime in practice.

Table 4: Statistical summary of posterior parameter estimates inferred from isolated intact mitochondria uptake assays, including 95% credible intervals.

Parameter	**Mean**	**Median**	**Mode**	**Std**	**95% Credible Interval**	
					Low	**High**
$T^s_{\max}$	67.209	67.150	67.033	3.4395	60.660	74.102
$T^m_{\max}$	53.162	53.121	53.103	1.4494	50.448	56.122
K^s_m	1.1387	1.1382	1.1387	0.076008	0.99135	1.2888
K^m_m	0.23009	0.22982	0.22907	0.015321	0.20097	0.26072
K^p_m	0.76652	0.73785	0.58268	0.35948	0.18643	1.5894
λ_{21}	0.041481	0.019144	0.012203	0.079453	0.01027	0.23232
λ_{31}	35.399	29.645	21.779	20.349	10.011	87.426
σ^2	2.1579	2.0155	1.8275	0.80027	1.1337	4.2201

Table 5: Statistical summary of posterior parameter estimates inferred from proteoliposome transport assays, including 95% credible intervals.

Parameter	**Mean**	**Median**	**Mode**	**Std**	**95% Credible Interval**	
					Low	**High**
$T^m_{\max}$	9.5011	8.7143	8.5784	2.7581	6.1540	17.497
K^m_m	0.53092	0.49264	0.45581	0.18066	0.28148	1.0025
K^p_m	8.9870	7.1638	3.9217	6.4434	1.6343	25.931
λ_{21}	0.052137	0.046076	0.042740	0.021108	0.027205	0.10996
λ_{31}	0.015758	0.013712	0.010504	0.0058706	0.010117	0.032148
σ^2	0.18237	0.17340	0.16311	0.052224	0.10744	0.31055

For the intact-mitochondria calibration, the effective sample sizes (N_{eff}) ranged from 4,936 to 8,156, while for the proteoliposome calibration they ranged from 4,953 to 5,097. These values indicate that the retained draws correspond to several thousand effectively independent samples per parameter. The Monte Carlo standard errors (MCSEs) are small relative to the posterior standard deviations (Σ), with MCSE/Σ ratios between 0.020 and

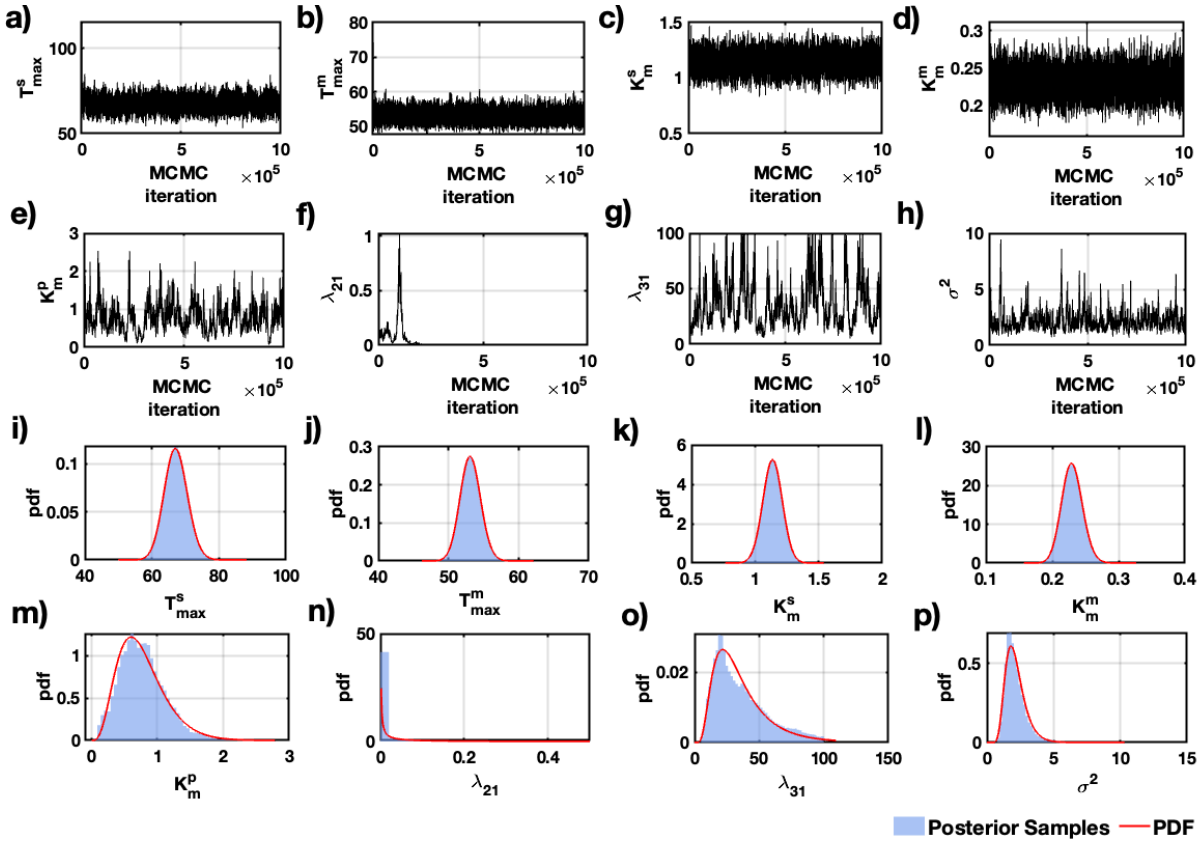

Figure 4: MCMC posterior summaries for the intact mitochondria uptake-assay calibration. Trace plots for the sampled parameter chains are shown in (a–h): (a) $T^s_{\max}$, (b) $T^m_{\max}$, (c) K^s_m, (d) K^m_m, (e) K^p_m, (f) λ_{21}, (g) λ_{31}, and (h) σ^2. Posterior densities for the same parameters are shown in (i–p), where blue histograms denote posterior samples and red curves denote the selected smooth density estimates. Specifically, the red curves correspond to: $T^s_{\max}$ (Gamma fit), $T^m_{\max}$ (Lognormal fit), K^s_m (Normal fit), K^m_m (Gamma fit), K^p_m (Gamma fit), λ_{21} (kernel density estimate; KDE), λ_{31} (Lognormal fit), and σ^2 (Lognormal fit). See Appendix K for the density-selection procedure used to choose the corresponding smooth estimates.

0.127 for the intact-mitochondria calibration and between 0.056 and 0.111 for the proteoliposome calibration. Most parameters meet the conventional benchmark MCSE/$\Sigma < 0.10$, suggesting that Monte Carlo variability contributes negligibly to posterior uncertainty.

For the intact-mitochondria calibration, the largest relative Monte Carlo errors occur for λ_{21} (0.127), λ_{31} (0.102), and K^p_m (0.092). For the proteoliposome calibration, slightly elevated relative Monte Carlo errors are observed for K^p_m (0.106), λ_{21} (0.109), and λ_{31} (0.111). These patterns most likely reflect stronger posterior correlations and/or weaker practical identifiability under the respective assay conditions, rather than lack of convergence, as supported by the corresponding $\hat{R}$ values remaining close to 1.0. Overall, these diagnostics indicate that the posterior summaries for both the intact-mitochondria and proteoliposome calibrations are numerically stable and suitable for inference, while highlighting parameters for which additional or more informative experiments could further reduce uncertainty.

Figures 4 and 5 summarize the MCMC trace plots and posterior distributions for parameters inferred from the intact-mitochondria uptake-assay calibration and the proteoliposome calibration, respectively. In both cases, the trace plots indicate stable exploration

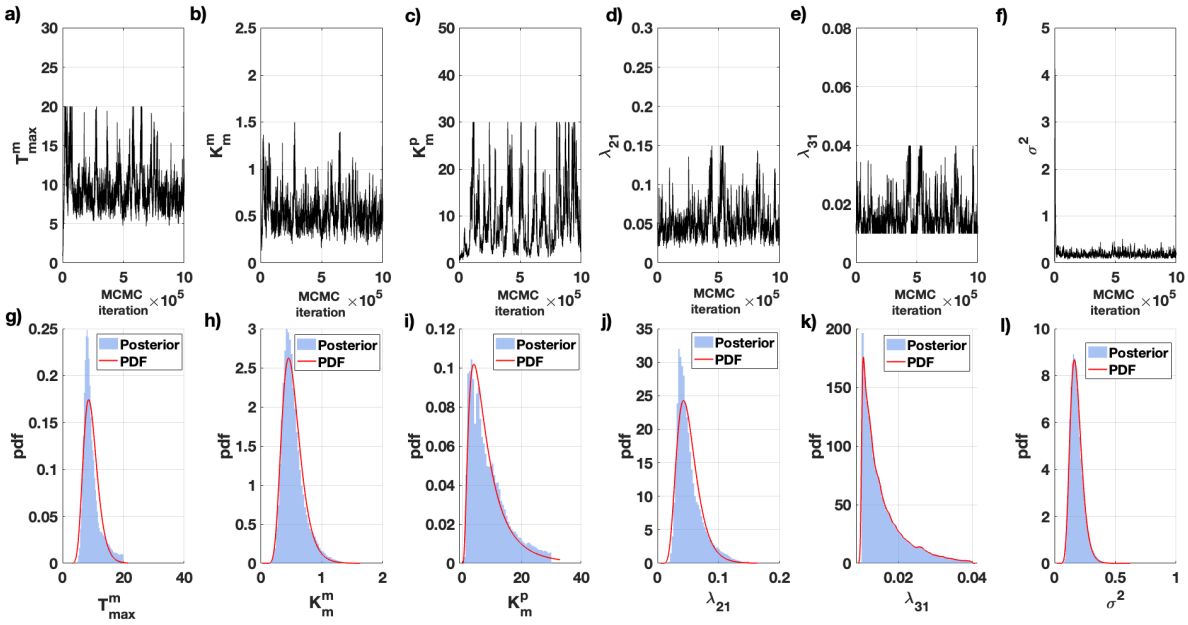

Figure 5: MCMC posterior summaries for the proteoliposome calibration. Trace plots for the sampled parameter chains: (a) $T^m_{\max}$, (b) K^m_m, (c) K^p_m, (d) λ_{21}, (e) λ_{31}, and (f) σ^2. Posterior densities for the same parameters are shown in (g–l), where blue histograms denote posterior samples and red curves denote smooth density estimates fit to the samples. The fitted density models are: $T^m_{\max}$ (Lognormal fit), K^m_m (Lognormal fit), K^p_m (Lognormal fit), λ_{21} (Lognormal fit), λ_{31} (kernel density estimate; KDE), and σ^2 (Lognormal fit). See Appendix K for the density-selection and summary procedure used to generate these curves.

Table 6: MCMC diagnostics for the intact mitochondria uptake-assay calibration. Diagnostics are reported per parameter with respect to total draws (N), burn-in draws (N_{burn}), effective sample size (N_{eff}), Monte Carlo standard error (MCSE), posterior standard deviation (Σ), relative Monte Carlo error (MCSE/Σ), and $\hat{R}$.

Parameter	N	N_{burn}	N_{eff}	**MCSE**	Σ	**MCSE**/Σ	$\hat{R}$
$T^s_{\max}$	1000000	10000	6875.724	0.135	3.448	0.039	1.0007
$T^m_{\max}$	1000000	10000	8156.273	0.030	1.435	0.021	1.0288
K^s_m	1000000	10000	6552.831	0.002	0.077	0.020	1.0002
K^m_m	1000000	10000	6743.586	0.000	0.015	0.020	1.0005
K^p_m	1000000	10000	4970.351	0.033	0.360	0.092	1.0014
λ_{21}	1000000	10000	4936.520	0.008	0.059	0.127	1.0279
λ_{31}	1000000	10000	4958.208	2.112	20.788	0.102	1.0062
σ^2	1000000	10000	5003.506	0.049	0.775	0.064	1.0006

of the posterior after burn-in, and the marginal densities highlight which parameters are well constrained by the available data.

For the intact-mitochondria dataset (Fig. 4), the transport-capacity parameters $T^s_{\max}$ and $T^m_{\max}$ and the dicarboxylate affinities K^s_m, K^m_m, and K^p_m exhibit well-mixed chains and relatively narrow, unimodal posteriors, indicating good practical identifiability under the uptake-assay conditions. By contrast, the coupling ratios show greater uncertainty than the capacity and affinity parameters: λ_{21} is strongly right-skewed with most posterior mass near small values, whereas λ_{31} displays a broader distribution with a pronounced right tail, suggesting that relative substrate weighting (particularly phosphate versus succinate)

Table 7: MCMC diagnostics for the proteoliposome uptake-assay calibration. Diagnostics are reported per parameter with respect to total draws (N), burn-in draws (N_{burn}), effective sample size (N_{eff}), Monte Carlo standard error (MCSE), posterior standard deviation (Σ), relative Monte Carlo error (MCSE/Σ), and $\hat{R}$.

Parameter	N	$N_{\textbf{burn}}$	$N_{\textbf{eff}}$	**MCSE**	Σ	**MCSE/Σ**	$\hat{R}$
$T^m_{\max}$	1000000	10000	5007.117	0.266	2.848	0.093	1.0007
K^m_m	1000000	10000	5009.954	0.015	0.187	0.079	1.0015
K^p_m	1000000	10000	4953.067	0.589	5.543	0.106	1.0017
λ_{21}	1000000	10000	4976.636	0.003	0.026	0.109	1.0035
λ_{31}	1000000	10000	4980.060	0.001	0.008	0.111	1.0039
σ^2	1000000	10000	5096.987	0.003	0.046	0.056	1.0007

is only weakly constrained by the intact-mitochondria uptake assays. The noise variance σ^2 is unimodal with a stationary trace, supporting a consistent estimate of model–data discrepancy under the Gaussian error assumption.

For the proteoliposome dataset (Fig. 5), the malate affinity K^m_m and $T^m_{\max}$ are tightly constrained, whereas K^p_m remains comparatively uncertain with a wider, right-skewed posterior. The coupling ratios are concentrated at small values: λ_{21} is relatively well constrained, while λ_{31} is more strongly concentrated near zero, consistent with limited information in this dataset for identifying phosphate-related weighting effects. This pattern also suggests potential posterior dependence between K^p_m and λ_{31}, since both parameters influence phosphate-related terms in the reduced flux expressions; consequently, the proteoliposome measurements may be less informative for disentangling these effects. As in the mitochondria calibration, σ^2 is narrowly distributed and the trace remains stationary.

Overall, the intact-mitochondria uptake assays constrain the core transport behavior more strongly, both transport capacities ($T^s_{\max}, T^m_{\max}$) and affinities (K^s_m, K^m_m, K^p_m) show well-behaved, relatively tight posteriors, whereas the proteoliposome calibration most tightly identifies the malate branch (notably K^m_m, with reasonable constraint on $T^m_{\max}$) but leaves phosphate-related effects less informative (broad K^p_m). In both settings, the coupling ratios ($\lambda_{21}, \lambda_{31}$) are comparatively harder to identify than capacity and affinity parameters, indicating that the available datasets more robustly determine the rate scale and dicarboxylate binding than the strength of phosphate-driven competition. Biologically, this implies that succinate/malate transport capacity and affinity are reliably supported by the uptake data, while conclusions about phosphate weighting are more assay-dependent: the intact-mitochondria posteriors allow substantial uncertainty in phosphate-versus-succinate weighting (broader λ_{31}), whereas the proteoliposome calibration concentrates λ_{31} near small values, suggesting weaker inferred phosphate weighting in the reconstituted setting.

Figures 6 and 7 compare prior and posterior distributions for the inferred parameters under the intact-mitochondria and proteoliposome calibrations, respectively. In the intact-mitochondria uptake assays (Fig. 6), the Gaussian priors for the transport capacities $T^s_{\max}$ and $T^m_{\max}$ and for the dicarboxylate affinities K^s_m, K^m_m, and K^p_m contract to narrower, unimodal posteriors, indicating strong practical identifiability from the uptake data. The coupling ratios exhibit the largest prior-to-posterior shift: λ_{21} concentrates near small values, while λ_{31} retains a broader, right-tailed posterior, suggesting that relative substrate-weighting—especially phosphate vs. succinate—is less directly constrained

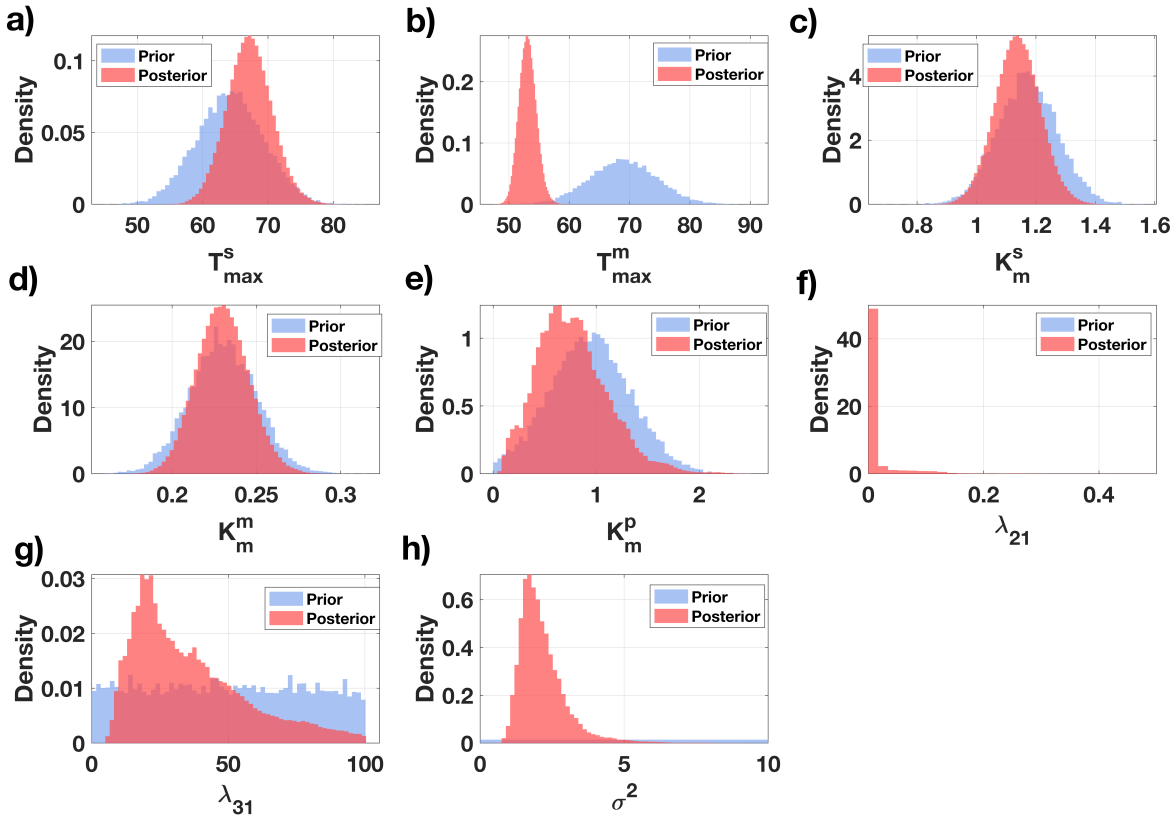

Figure 6: Prior–posterior comparison for the intact-mitochondria uptake-assay calibration. Overlaid density plots comparing the prior (blue) and posterior (red) distributions for all inferred model parameters under the intact-mitochondria uptake-assay setting. Panels (a–b) show the transport-capacity parameters $T^s_{\max}$ and $T^m_{\max}$; (c–e) show the substrate-affinity parameters K^s_m, K^m_m, and K^p_m; (f–g) show the coupling ratios λ_{21} (malate/succinate weighting) and λ_{31} (phosphate/succinate weighting); and (h) shows the observation-noise variance σ^2. Gaussian priors are used for the capacity and affinity parameters, while uniform priors are used for the coupling ratios and σ^2.

than core capacity/affinity parameters. In the proteoliposome setting (Fig. 7), the posteriors similarly depart from uniform priors, with the tightest contraction for the malate branch (K^m_m and, to a lesser extent, $T^m_{\max}$), while K^p_m remains wide and right-skewed and λ_{31} is strongly concentrated near zero, consistent with weaker identifiability of phosphate-related effects in the reconstituted system. In both datasets, the posterior for σ^2 concentrates toward small values, indicating a consistent and relatively low inferred model–data discrepancy under the Gaussian error assumption.

Figure 8 compares Bayesian model predictions (posterior mean and 95% credible intervals) against the experimental uptake-assay flux measurements. For the intact-mitochondria datasets (Fig. 8a–c), the inferred model closely tracks the observed trends across all tested conditions. Specifically, succinate uptake J_{succ} (Fig. 8a) increases monotonically with external succinate $[S_c]$, and the posterior mean follows the experimental curve with all points lying within the 95% credible band, indicating that the calibrated transport capacity and succinate affinity are well constrained. For malate uptake J_{mal} under non-competitive conditions (Fig. 8b), the posterior mean reproduces the saturating dependence on $[M_c]$, with minor deviations at intermediate concentrations remaining consistent with the credible uncertainty. Under competitive conditions with external succinate present (Fig. 8c), the model captures the reduced malate flux across $[M_c]$, demon-

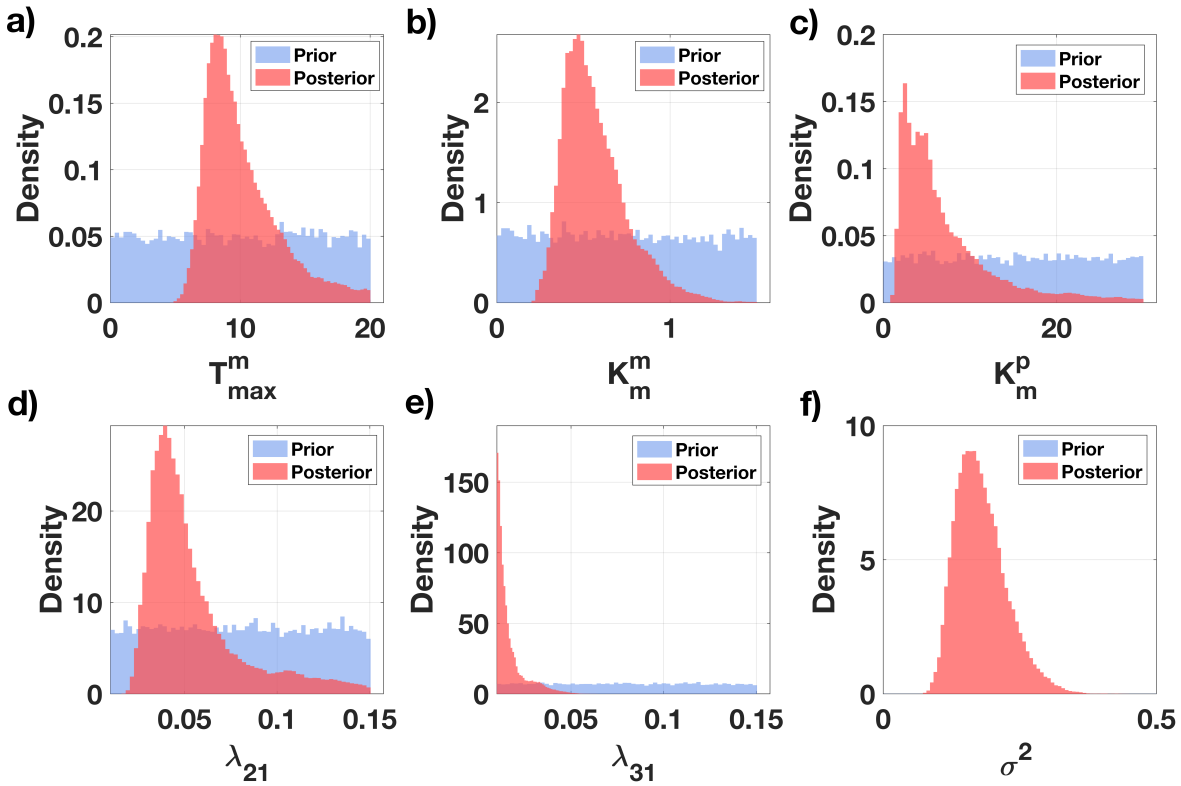

Figure 7: Prior–posterior comparison for the proteoliposome calibration. Overlaid density plots comparing the prior (blue) and posterior (red) distributions for all inferred parameters under the proteoliposome setting. Panels (a–c) show the inferred kinetic parameters $T^m_{\max}$, K^m_m, and K^p_m; (d–e) show the coupling ratios λ_{21} (malate/succinate weighting) and λ_{31} (phosphate/succinate weighting); and (f) shows the observation-noise variance σ^2. Uniform priors are used for all parameters in this calibration.

strating that the inferred competitive coupling in the ping–pong framework quantitatively accounts for substrate competition.

The proteoliposome validation experiments (Fig. 9a–f) show similarly strong agreement between model and data under multiple assay configurations. The model reproduces malate transport responses across varying $[M_c]$ at fixed intravesicular phosphate $[P_m]$ (Fig. 9a, 9b, 9e), as well as the dependence of malate flux on $[P_m]$ at fixed $[M_c]$ (Fig. 9c, 9f), indicating that the model captures the phosphate-coupled exchange kinetics in the reconstituted system. In addition, the model matches the phosphate uptake data J_{pho} as a function of external phosphate $[P_c]$ at fixed intravesicular malate (Fig. 9d), supporting consistency of the inferred phosphate-linked exchange step.

Overall, across both intact mitochondria and proteoliposome settings, the posterior predictive bands generally enclose the experimental measurements and the posterior mean trajectories reproduce the observed saturation and competitive effects. These results support that the Bayesian-calibrated model provides a quantitatively accurate and mechanistically consistent representation of SLC25A10-mediated dicarboxylate/phosphate exchange under the experimental assay conditions.

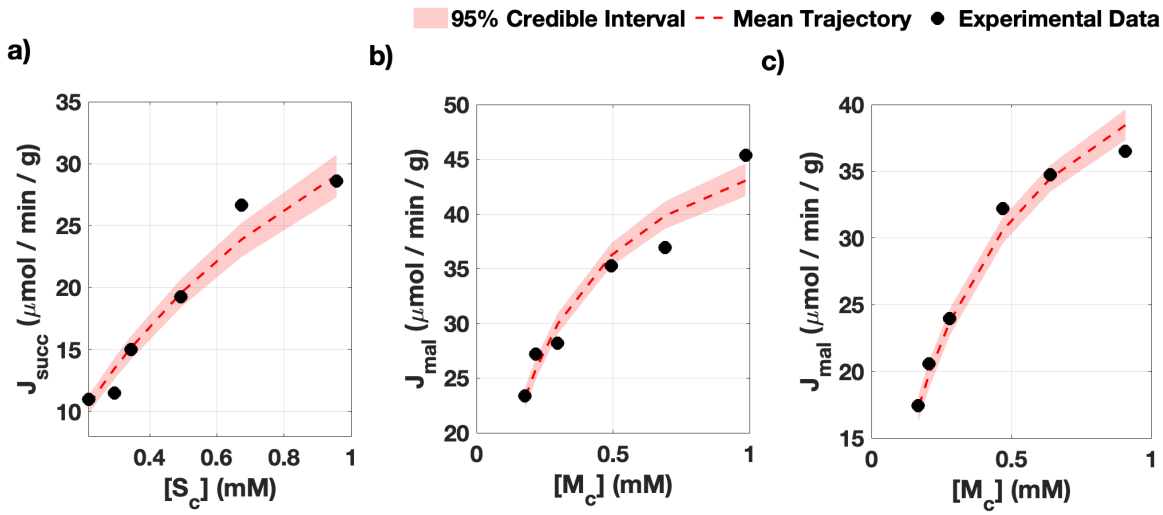

Figure 8: Model validation against isolated intact-mitochondria uptake assays. Experimental uptake fluxes (black dots) are compared with the Bayesian model fit, shown as the posterior mean trajectory (red dashed line) with a 95% credible interval (shaded band). **(a)** Succinate uptake flux J_{succ} as a function of external succinate concentration $[S_c]$, with external malate and phosphate held at zero. **(b)** Malate uptake flux J_{mal} as a function of external malate concentration $[M_c]$ under non-competitive conditions (no external succinate or phosphate). **(c)** Malate uptake flux J_{mal} as a function of $[M_c]$ under competitive conditions, with external succinate fixed at 0.5 mM and external phosphate set to zero.

4.4 Thermodynamic Validation of the Kinetic Model

To ensure that the SLC25A10 model is not only mathematically consistent but also thermodynamically sound, we validated it by analyzing flux trajectories, Gibbs free-energy dissipation, and equilibrium metabolite concentrations under defined initial conditions in both calibration settings.

Figures 10 and 11 show that the model satisfies thermodynamic constraints and reproduces the analytically predicted equilibrium partitioning between compartments. In the intact-mitochondria setting (Fig. 10), the antiport nature of the mechanism is reflected by the opposing signs of the succinate and phosphate fluxes, J_{succ} and J_{pho}, which relax to zero as concentration gradients dissipate (Fig. 10a). Consistently, the Gibbs free-energy change ΔG increases toward zero and asymptotically approaches $\Delta G = 0$, indicating relaxation to thermodynamic equilibrium (Fig. 10b). Simulated equilibrium concentrations for succinate and phosphate in the matrix and external medium agree closely with the closed-form equilibrium expressions derived from the reduced mass-balance formulation (Fig. 10c–f), providing an independent check that the reduced and full formulations are mutually consistent.

An analogous validation holds in the proteoliposome setting (Fig. 11). Here, the malate and phosphate fluxes, J_{mal} and J_{pho}, exhibit rapid relaxation to zero (Fig. 11a), and the corresponding ΔG trajectory approaches $\Delta G = 0$ (Fig. 11b). As in the intact-mitochondria case, the simulated equilibrium concentrations match the analytically derived equilibrium values for the malate/phosphate exchange system (Fig. 11c–f).

Together, these results demonstrate that the model implements a reversible, electroneutral 1:1 antiport constraint between a dicarboxylate and phosphate, and that its dynamics are thermodynamically consistent: modeled fluxes decay as driving forces dis-

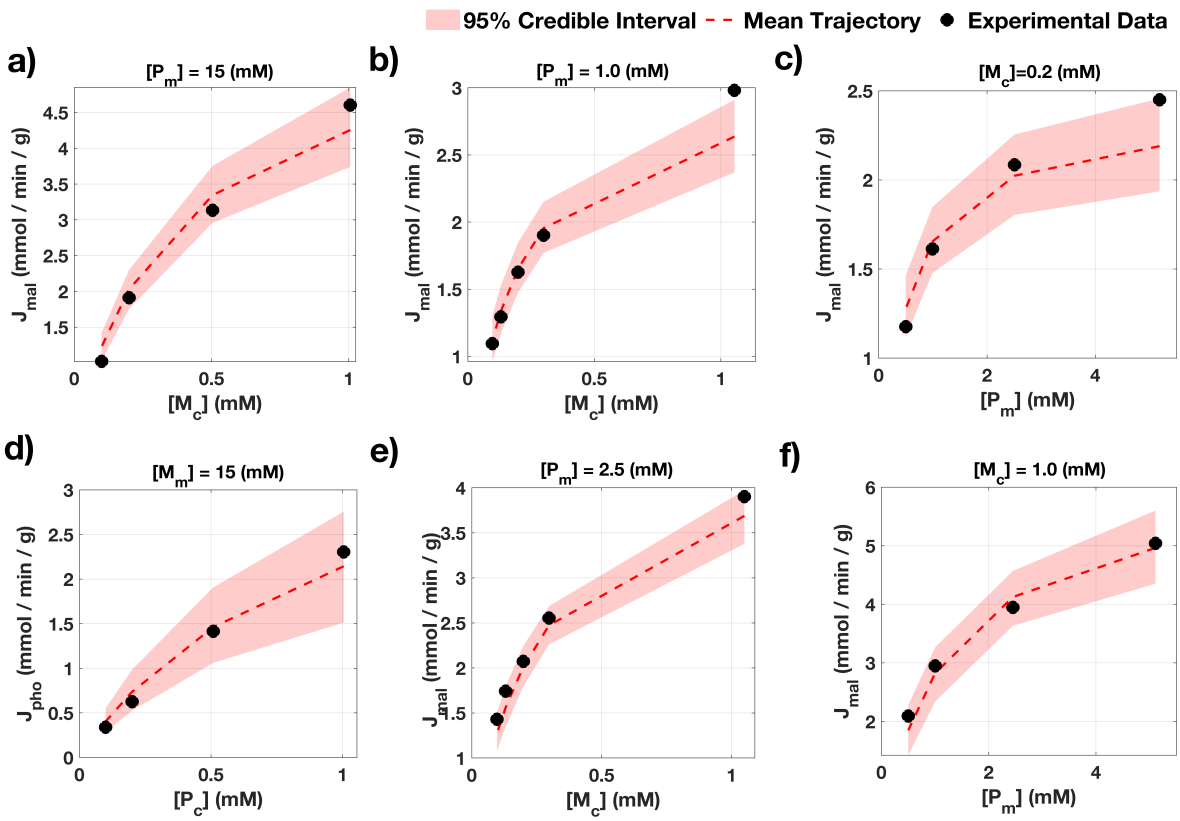

Figure 9: Model validation against proteoliposome uptake assays. Experimental flux measurements (black dots) are compared with the Bayesian model fit, shown as the posterior mean trajectory (red dashed line) with a 95% credible interval (shaded band). **(a)** Malate uptake flux J_{mal} as a function of external malate $[M_c]$ with intravesicular phosphate fixed at $[P_m] = 15$ mM. **(b)** J_{mal} versus $[M_c]$ with $[P_m] = 1.0$ mM. **(c)** J_{mal} versus intravesicular phosphate $[P_m]$ with external malate fixed at $[M_c] = 0.2$ mM. **(d)** Phosphate uptake flux J_{pho} as a function of external phosphate $[P_c]$ with intravesicular malate fixed at $[M_m] = 15$ mM. **(e)** J_{mal} versus $[M_c]$ with $[P_m] = 2.5$ mM. **(f)** J_{mal} versus $[P_m]$ with $[M_c] = 1.0$ mM.

sipate, and the system converges to the analytically predicted equilibrium state. In the intact-mitochondria configuration, this equilibration illustrates how a dicarboxylate–phosphate exchange mechanism can redistribute succinate (or malate) relative to the extra-matrix compartment while maintaining strict coupling to phosphate counter-transport, linking dicarboxylate handling relevant to TCA-cycle metabolism with phosphate exchange relevant to mitochondrial bioenergetics.

4.5 Our model reveals the non-equilibrium dynamics of the dicarboxylate carrier (SLC25A10), shedding light on behaviors that are experimentally challenging

To investigate the dynamic behavior of the SLC25A10 transporter under experimentally realistic conditions, we simulated a competitive transport scenario analogous to the classical malate–succinate uptake experiments of Palmieri et al. [3]. The system was initialized with 0.908 mM malate, 0.5 mM succinate, and no phosphate in the external compartment, while the mitochondrial matrix concentrations and compartment volumes are set accord-

ing to Table 1. These conditions mimic isolated mitochondrial uptake assays but allow us to resolve rapid transients that are experimentally inaccessible due to the sub-second timescale of equilibration and the technical difficulty of measuring compartment-resolved metabolite gradients in real time.

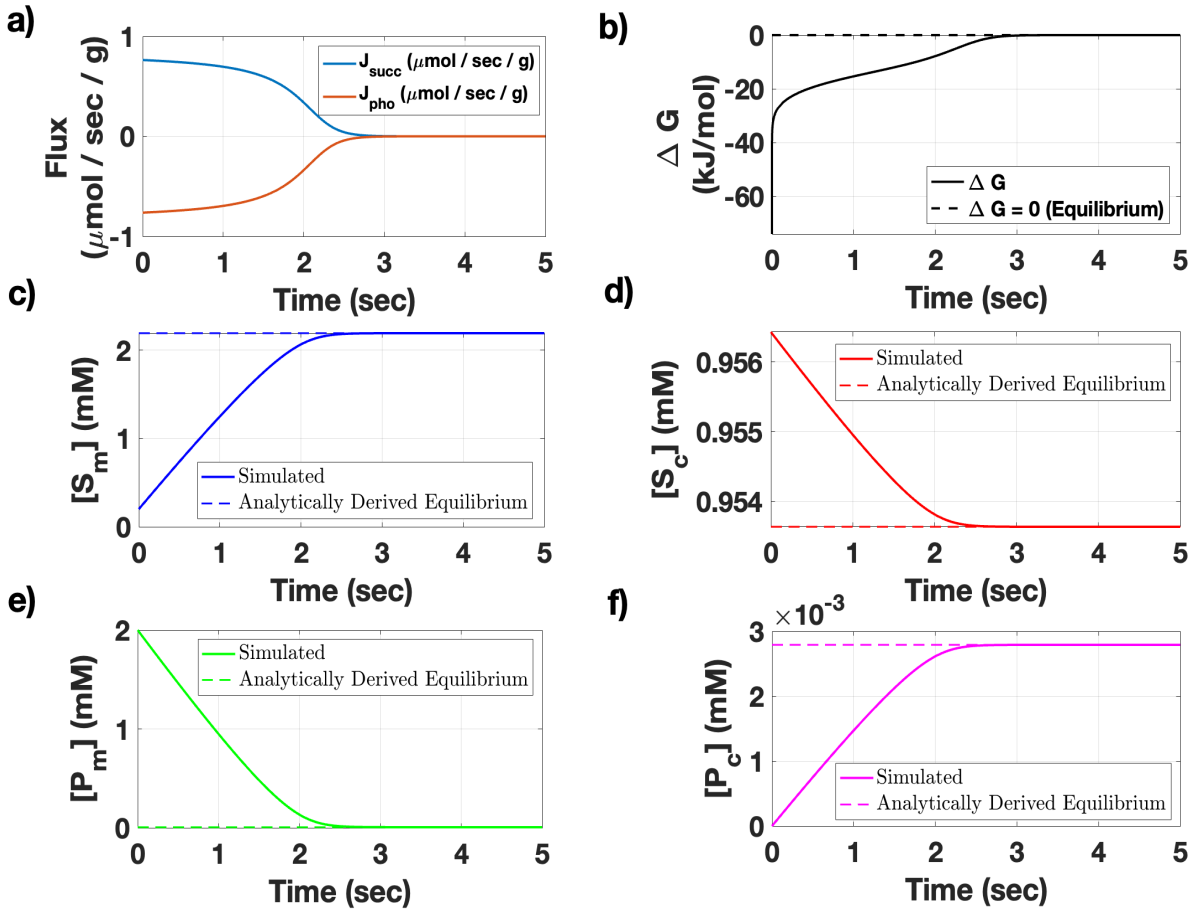

Figure 10: Thermodynamic analysis and equilibrium validation of the SLC25A10 antiport model in the intact mitochondria setting. (a) Time-dependent fluxes of succinate (J_{succ}) and phosphate (J_{pho}) showing relaxation toward equilibrium under electroneutral exchange stoichiometry. (b) Time-resolved Gibbs free energy change (ΔG) for the succinate/phosphate exchange reaction $\mathrm{S}_m + \mathrm{P}_c \rightleftharpoons \mathrm{S}_c + \mathrm{P}_m$; the dashed line indicates $\Delta G = 0$ (thermodynamic equilibrium).(c–f) Simulated concentrations of succinate and phosphate in the matrix (m) and the external compartment (c; assay medium) compared with analytically derived equilibrium values (dashed lines). Initial conditions are $[S_c] = 0.1$ mM and $[P_c] = 0$ mM, with malate set to zero in both compartments; remaining initial concentrations are set according to Table 1. Simulations use the intact-mitochondria compartment volumes (per gram protein) reported in Table 1. Parameter values for $T^s_{\max}$, K^s_m, K^p_m, λ_{21}, and λ_{31} are fixed at their posterior modes (Table 4).

Figure 12 shows the time evolution of metabolite concentrations and their gradients across the inner mitochondrial membrane. Matrix malate ($[M_m]$) increases rapidly (Fig. 12a), while external malate ($[M_c]$) decreases correspondingly (Fig. 12b), producing a transient rise in the malate gradient (Fig. 12c). Succinate exhibits a similar but more gradual response. The $[S_m]$ increases (Fig. 12d) as $[S_c]$ decreases (Fig. 12e), yielding a steadily increasing succinate gradient (Fig. 12f). In contrast, phosphate displays the opposite trend. The $[P_m]$ decreases sharply (Fig. 12g) while $[P_c]$ increases (Fig. 12h), leading

to a rapid collapse of the phosphate gradient (Fig. 12i).

The corresponding flux trajectories (Fig. 13) reveal the mechanistic basis of these concentration changes under the rapid-equilibrium reduction for binding/unbinding. Initially, malate flux (J_{mal}) is positive, indicating net import into the matrix, while phosphate flux (J_{pho}) is negative, indicating net export to the external compartment (Fig. 13a). Succinate flux (J_{succ}) is comparatively smaller in magnitude, consistent with competitive exchange in which malate dominates early transport. All flux components relax toward zero on a sub-second timescale as the concentration gradients equilibrate. The total transport magnitude J_{tot} (Fig. 13b) exhibits a pronounced initial peak followed by rapid decay, capturing the short-lived burst of carrier turnover immediately after gradient imposition.

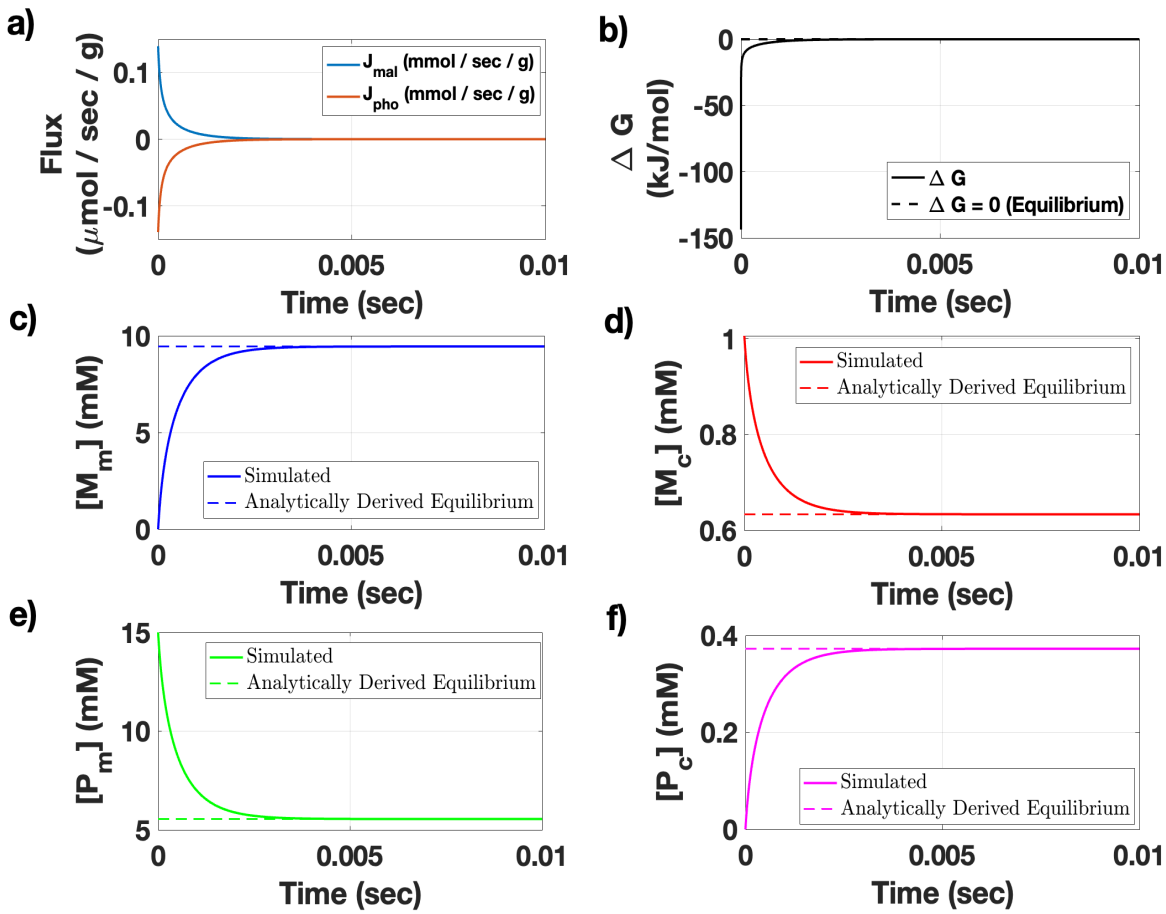

Figure 11: Thermodynamic analysis and equilibrium validation of the SLC25A10 antiport model in the proteoliposome setting. (a) Time-dependent fluxes of malate (J_{mal}) and phosphate (J_{pho}) showing rapid relaxation toward equilibrium under electroneutral exchange stoichiometry. (b) Time-resolved Gibbs free-energy change (ΔG) for the malate/phosphate exchange reaction $\text{M}_m + \text{P}_c \rightleftharpoons \text{M}_c + \text{P}_m$; the dashed line indicates $\Delta G = 0$ (thermodynamic equilibrium). (c–f) Simulated concentrations of malate and phosphate in the internal compartment (m) and the external compartment (c; extraliposomal assay medium) compared with analytically derived equilibrium values (dashed lines). Initial conditions are $[M_c] = 1$ mM and $[P_m] = 15$ mM, with $[M_m] = 0$ and $[P_c] = 0$. Simulations use the proteoliposome compartment volumes (per gram protein) reported in Table 1. Parameter values for $T^m_{\max}$, K^m_m, K^p_m, λ_{21}, and λ_{31} are fixed at their posterior modes (Table 5).

Together, these simulations highlight the transient and gradient-driven nature of SLC25A10 transport under the rapid-equilibrium reduction. The imposed phosphate

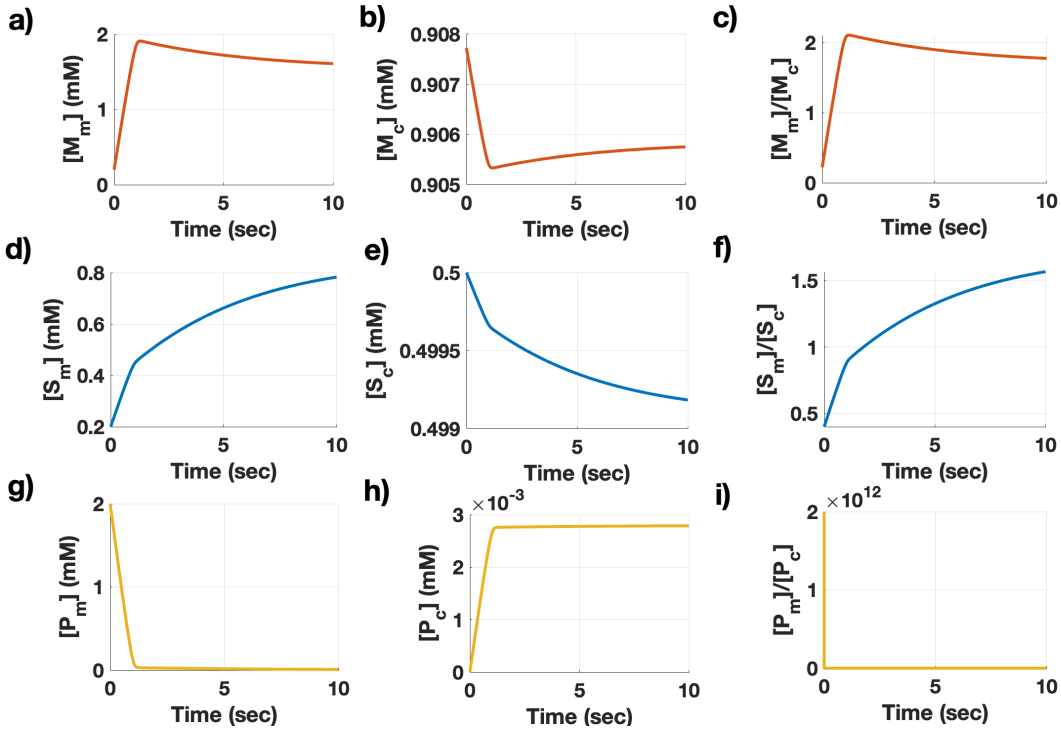

Figure 12: Time-dependent concentration and gradient dynamics of the SLC25A10 transporter in the intact-mitochondria setting. (a–b) Malate concentrations in the matrix (m) and external compartment (c); (c) malate concentration ratio $[M_m]/[M_c]$. (d–e) Succinate concentrations in the matrix and external compartment; (f) succinate concentration ratio $[S_m]/[S_c]$. (g–h) Phosphate concentrations in the matrix and external compartment; (i) phosphate concentration ratio $[P_m]/[P_c]$. Initial external concentrations are $[M_c] = 0.908$ mM, $[S_c] = 0.50$ mM, and $[P_c] = 10^{-12}$ mM (used in place of zero to avoid division by zero in $[P_m]/[P_c]$), while initial matrix concentrations $[M_m]$, $[S_m]$, and $[P_m]$ are set according to Table 1. Compartment volumes also follow Table 1. Parameter values are set to the intact-mitochondria posterior summary (Table 4).

gradient drives a brief burst of exchange in which phosphate exits the matrix while dicarboxylates enter, consistent with the electroneutral 1:1 antiport stoichiometry and the requirement for a counter-substrate to sustain cycling. In this competitive regime, malate carries the larger share of the early dicarboxylate influx, while succinate contributes more modestly, reflecting competition at the single binding site in the ping–pong mechanism. As phosphate redistributes and its gradient collapses, the driving force diminishes and all flux components relax toward zero, indicating that SLC25A10 behaves as a rapid buffering exchanger rather than a sustained flux provider at steady state. Overall, these non-equilibrium dynamics illustrate how SLC25A10 can rapidly reshape matrix–external dicarboxylate and phosphate distributions following changes in substrate availability during experimental perturbations or metabolic stress [5, 4].

4.6 Effect of Mitochondrial Morphology on Initial SLC25A10 Fluxes

To quantify how mitochondrial morphology modulates dicarboxylate exchange, we investigated the sensitivity of the initial SLC25A10 fluxes to protein-normalized compartment volumes in the intact mitochondria setting. We considered two coupled scenarios: matrix

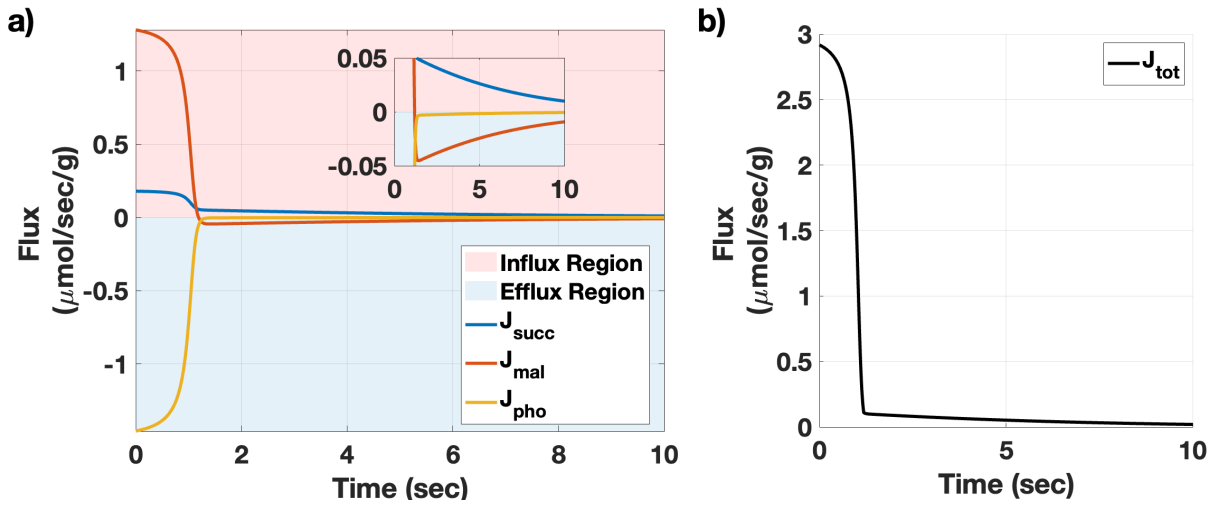

Figure 13: Time-varying SLC25A10 fluxes in the intact-mitochondria setting under the rapid-equilibrium reduction for binding/unbinding. (a) Individual flux components for succinate (J_{succ}), malate (J_{mal}), and phosphate (J_{pho}) as functions of time. Positive flux denotes net transport into the matrix; negative flux denotes net transport into the external compartment. Shaded regions indicate influx (pink) and efflux (blue) according to this sign convention. (b) Total transport magnitude $J_{\text{tot}} = |J_{\text{succ}}| + |J_{\text{mal}}| + |J_{\text{pho}}|$. Initial external concentrations are $[M_c] = 0.908$ mM, $[S_c] = 0.50$ mM, and $[P_c] = 10^{-12}$ mM (used in place of zero for numerical stability), while initial matrix concentrations and compartment volumes are set according to Table 1. Parameter values are fixed at their posterior modes (Table 4).

swelling, in which $\tilde{V}_m$ increases while $\tilde{V}_c$ decreases, and matrix condensation, in which $\tilde{V}_m$ decreases while $\tilde{V}_c$ increases. The combined matrix and external (medium) specific volume per gram protein was held fixed by enforcing $\tilde{V}_m + \tilde{V}_c = \tilde{V}_{\text{tot}}$, such that increases in $\tilde{V}_m$ are accompanied by compensatory decreases in $\tilde{V}_c$, and vice versa. Here, $\tilde{V}_{\text{tot}}$ is defined as the sum of the baseline $\tilde{V}_m$ and $\tilde{V}_c$ values reported in Table 1. For each condition, we recorded the succinate flux (J_{succ}), malate flux (J_{mal}), phosphate flux (J_{pho}), and the total transport magnitude (J_{tot}) at $t = 1$ s (Fig. 14).

Figure 14 shows the dependence of initial carrier activity on morphology under the coupled-volume constraint. Increasing the matrix volume (swelling) modestly increases both dicarboxylate flux components, J_{succ} and J_{mal} (Fig. 14a–b), while simultaneously making the phosphate flux J_{pho} more negative (Fig. 14c), indicating stronger phosphate export from the matrix under our sign convention. This coordinated change is consistent with the antiport stoichiometry: enhanced dicarboxylate influx is accompanied by an increased counter-flux of phosphate in the opposite direction. The net effect is an increase in the overall transport magnitude J_{tot} with swelling (Fig. 14d), indicating faster initial carrier turnover when the matrix swells and the opposing compartment contracts.

Conversely, matrix condensation produced the opposite behavior: J_{succ} and J_{mal} decreased, J_{pho} became less negative (weaker counter-transport in the negative direction), and J_{tot} declined. Mechanistically, these trends are not driven by changes in the intrinsic binding parameters (K_m^s, K_m^m, K_m^p), which are held fixed, but rather by how compartment volumes scale the early-time evolution of concentration gradients. In particular, swelling reduces the rate of concentration change on the matrix side while amplifying it on the external side, thereby altering the short-time gradients and the effective competition and saturation factors entering the REA flux expressions. Under the coupled-volume con-

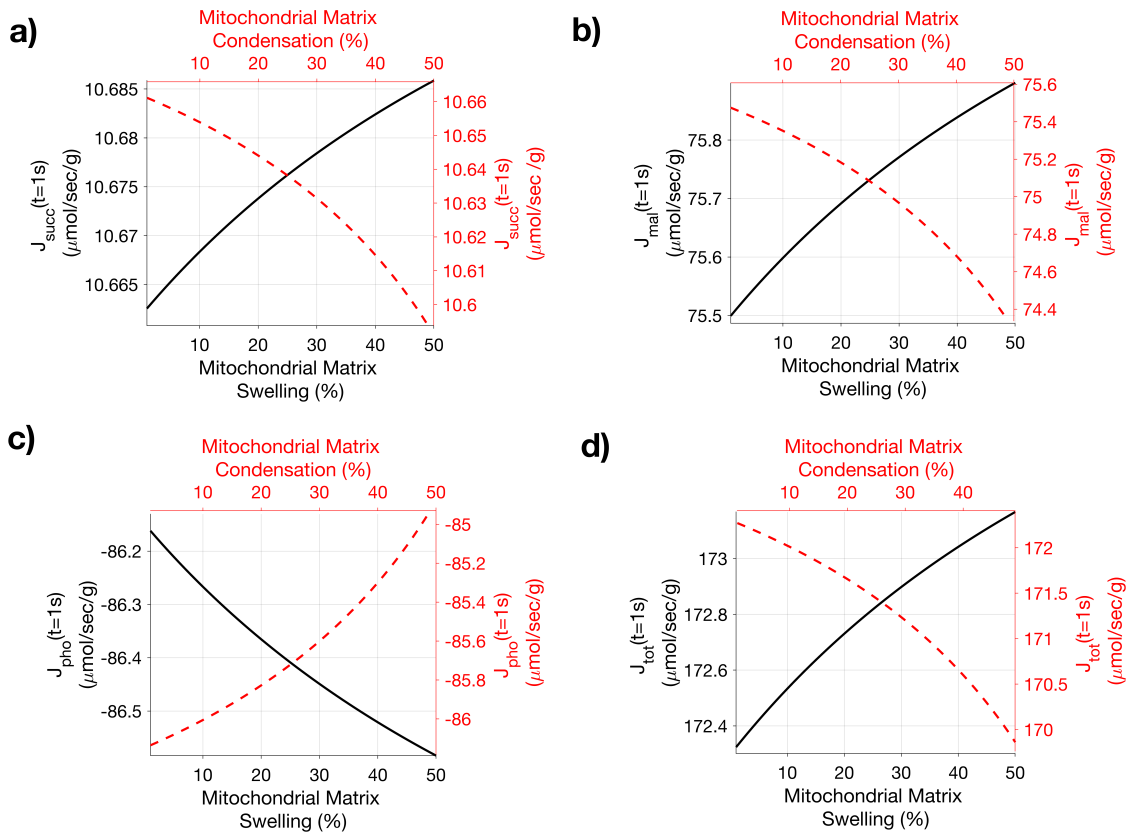

Figure 14: Effect of matrix swelling and condensation on initial SLC25A10 fluxes under a coupled-volume constraint in intact mitochondria. Changes in the initial fluxes of (a) succinate J_{succ}, (b) malate J_{mal}, (c) phosphate J_{pho}, and (d) the total transport magnitude J_{tot}, evaluated at time equal to one second ($t = 1$ s), as the matrix normalized volume ($\tilde{V}_m$) is varied between -50% (condensation; red dashed curves) and $+50\%$ (swelling; black solid curves) relative to the baseline value in Table 1. Initial concentrations are set to $[M_c] = 0.91$ mM, $[S_c] = 0.5$ mM, and $[P_c] = 0.1$ mM on the external side, while $[M_m]$, $[S_m]$, and $[P_m]$ in the matrix are set according to Table 1. Parameter values for $T^s_{\max}$, $T^m_{\max}$, $T^p_{\max}$, K^s_m, K^m_m, K^p_m, λ_{21}, and λ_{31} are fixed at their posterior modes (Table 4).

straint, these effects bias the initial exchange toward larger dicarboxylate fluxes (and a correspondingly larger phosphate counter-flux) when the matrix swells.

Overall, the dependence on morphology is monotonic over the tested range: swelling systematically increases J_{tot}, whereas condensation decreases it. Among the individual components, malate shows the largest absolute change, consistent with its larger baseline magnitude under the assay conditions. These results emphasize that morphology-induced volume redistribution—when the total matrix-plus-external volume per protein is constrained—can modulate the initial transport capacity of SLC25A10 by reshaping how rapidly gradients evolve, rather than by altering intrinsic affinity parameters. This is consistent with the general biophysical principle that compartment volumes buffer concentration changes and thereby influence transport-driven transients and effective driving forces [25, 26, 27, 28, 29]. Physiologically, moderate, transient changes in matrix volume could therefore tune early exchange rates, whereas sustained condensation could dampen initial dicarboxylate/phosphate turnover and slow the redistribution of metabolites across the inner mitochondrial membrane.

4.7 Succinate accumulation drives SLC25A10-mediated transport dynamics under SDH deficiency

Succinate is a key intermediate of the TCA cycle; however, excessive accumulation in the mitochondrial matrix is associated with multiple pathophysiological states, including cancer and metabolic disorders [5]. Within the matrix, succinate levels are tightly regulated by two enzymes: succinyl-CoA synthetase (SCAS), which generates succinate, and succinate dehydrogenase (SDH), which consumes it [15, 16, 17, 38]. Inactivating mutations in SDH impair succinate oxidation and lead to pathological succinate buildup [12, 13, 38, 5]. A central question is how the dicarboxylate carrier SLC25A10 responds under these SDH-deficient conditions, when the normal metabolic sink is absent.

To investigate this, we extended the intact-mitochondria calibrated reduced exchange model by coupling SLC25A10 to SDH and SCAS fluxes, which represent an enzymatic sink and source for matrix succinate, respectively (Fig. 15a). Throughout, carrier kinetics are held fixed at their intact-mitochondria posterior estimates, enabling a direct comparison of SDH-active and SDH-deficient scenarios and isolating the effect of altered metabolic context on the emergent exchange dynamics.

Figure 15 illustrates how coupling the carrier to SDH and SCAS reshapes the emergent dynamics under SDH-active conditions. The concentration trajectories (Fig. 15b) show a pronounced early transient driven by rapid carrier exchange: matrix malate $[M_m]$ rises sharply (overshoot) while external malate $[M_c]$ dips, consistent with an initial burst of malate uptake. In parallel, matrix succinate $[S_m]$ exhibits a brief increase followed by a rapid drop to low levels, reflecting fast SDH-mediated oxidation of imported succinate; thereafter, $[S_m]$ shows only a small recovery consistent with the comparatively weaker SCAS source term. Phosphate displays strong net export on this timescale: $[P_m]$ collapses quickly while $[P_c]$ rises, indicating sustained matrix phosphate depletion. The corresponding fluxes (Fig. 15c–d) support this interpretation: J_{mal} and J_{pho} show a short lived, high magnitude exchange burst that relaxes rapidly as gradients dissipate, whereas the enzymatic fluxes satisfy J_{SDH} bigger than J_{SCAS} over the simulated window, maintaining low matrix succinate and setting the slower relaxation of the coupled system.

Figure 16 compares SDH-active and SDH-deficient conditions. In the SDH-deficient scenario, matrix succinate $[S_m]$ remains elevated relative to the SDH-active case and is sustained at a higher level over the simulated window (Fig. 16b), consistent with removal of the SDH sink. In contrast, in the SDH-active case, $[S_m]$ rapidly relaxes to a low level after a short transient. Matrix malate $[M_m]$ also differs markedly between the two conditions: under SDH deficiency it stays high, whereas under SDH activity it decays toward near depletion (Fig. 16a). Phosphate $[P_m]$ is rapidly depleted in both cases on this timescale (Fig. 16c), while the external pools show only small but distinct shifts (Fig. 16d–f). Flux profiles confirmed these trajectories (Fig. 16g–i).

Physiologically, this reduced SLC25A10 exchange model coupled to SDH and SCAS captures a minimal control loop for matrix succinate: SCAS supplies succinate (and consumes phosphate), SDH provides the dominant succinate sink when present, and SLC25A10 offers a rapid, phosphate-coupled exchange route that redistributes dicarboxylates in response to gradients. When SDH is active, succinate is efficiently buffered by oxidation and the carrier primarily contributes fast equilibration rather than sustained net export. When SDH is deficient, removal of the dominant sink sustains elevated $[S_m]$ and increases the thermodynamic tendency for succinate efflux; however, under the present

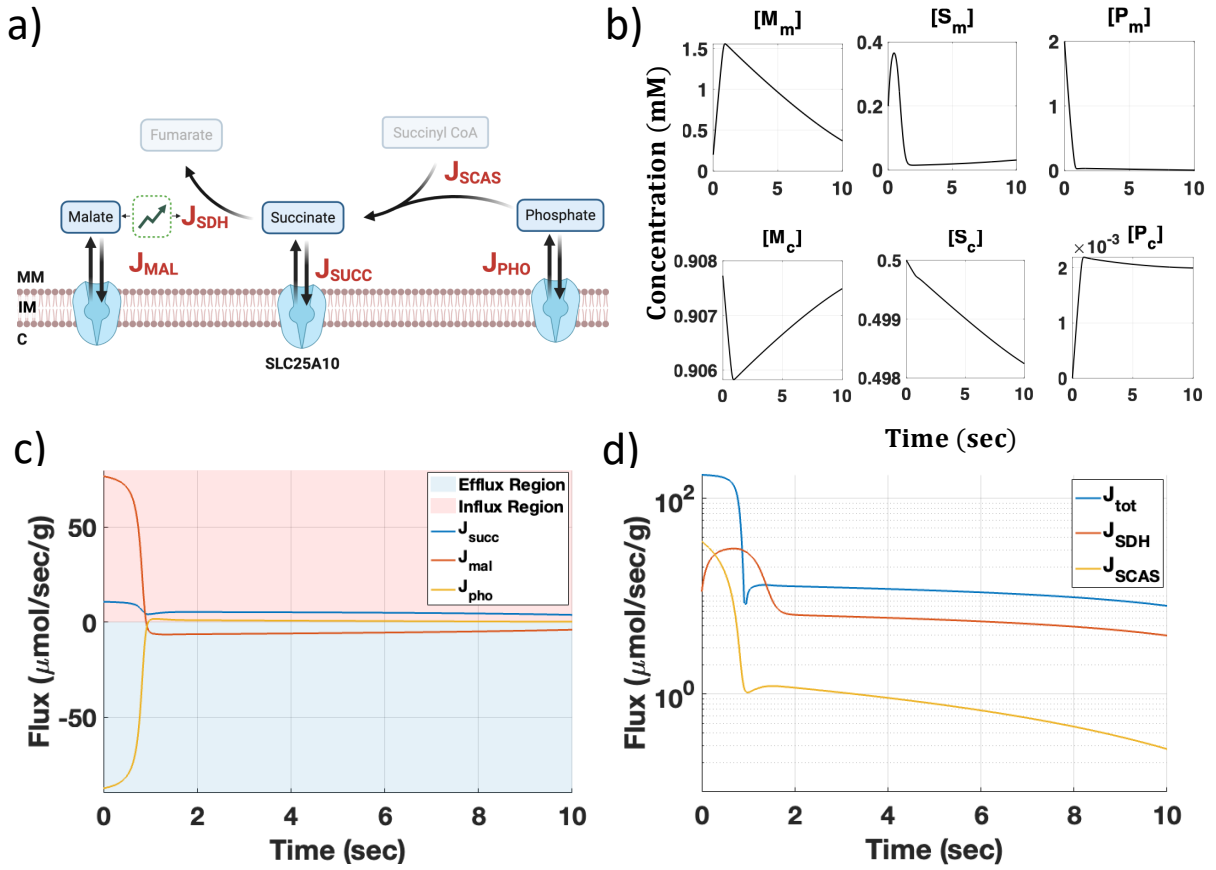

Figure 15: Metabolic integration of SLC25A10 with succinate dehydrogenase (SDH) and succinyl–CoA synthetase (SCAS) in the intact-mitochondria setting. (a) Schematic coupling of SLC25A10-mediated dicarboxylate/phosphate exchange with SDH (succinate oxidation) and SCAS (succinate production) within the mitochondrial matrix (MM); the external compartment c. (b) Time courses of matrix (top row) and external (bottom row) concentrations for malate, succinate, and phosphate. (c) Time-dependent SLC25A10 flux components J_{succ}, J_{mal}, and J_{pho}, with shaded regions indicating influx (pink) and efflux (blue). (d) Comparison of the total transporter activity J_{tot} with the enzymatic fluxes J_{SDH} and J_{SCAS} (log scale). Simulations use the intact-mitochondria compartment volumes and initial matrix concentrations from Table 1; initial external concentrations are $[M_c] = 0.908$ mM, $[S_c] = 0.5$ mM, with no phosphate. Kinetic parameters are set to the posterior modes from Table 4.

initial conditions, carrier-mediated exchange still relaxes rapidly toward near-equilibrium, so the dominant signature of SDH loss is persistent matrix succinate elevation. Within this module, malate shapes succinate handling indirectly by modulating SDH throughput in the SDH-active regime and by competing with succinate for phosphate-coupled exchange via SLC25A10 when SDH is absent.

This framework is consistent with the broader concept that succinate accumulation in SDH-deficient settings can promote pseudohypoxic signaling, in which cytosolic succinate inhibits prolyl hydroxylases and stabilizes HIF-1α, activating hypoxia-responsive transcriptional programs implicated in SDH-deficient chromaffin tumors such as paragangliomas and pheochromocytomas [12, 13, 54, 14, 5].

Finally, to provide biological context for the model and to assess qualitative consistency with cellular phenotypes associated with SLC25A10 perturbation, we performed targeted metabolomic measurements in immortalized murine chromaffin cells (imCCs) with inducible SLC25A10 knockdown (SLC25A10-KD), alongside wild-type imCCs as

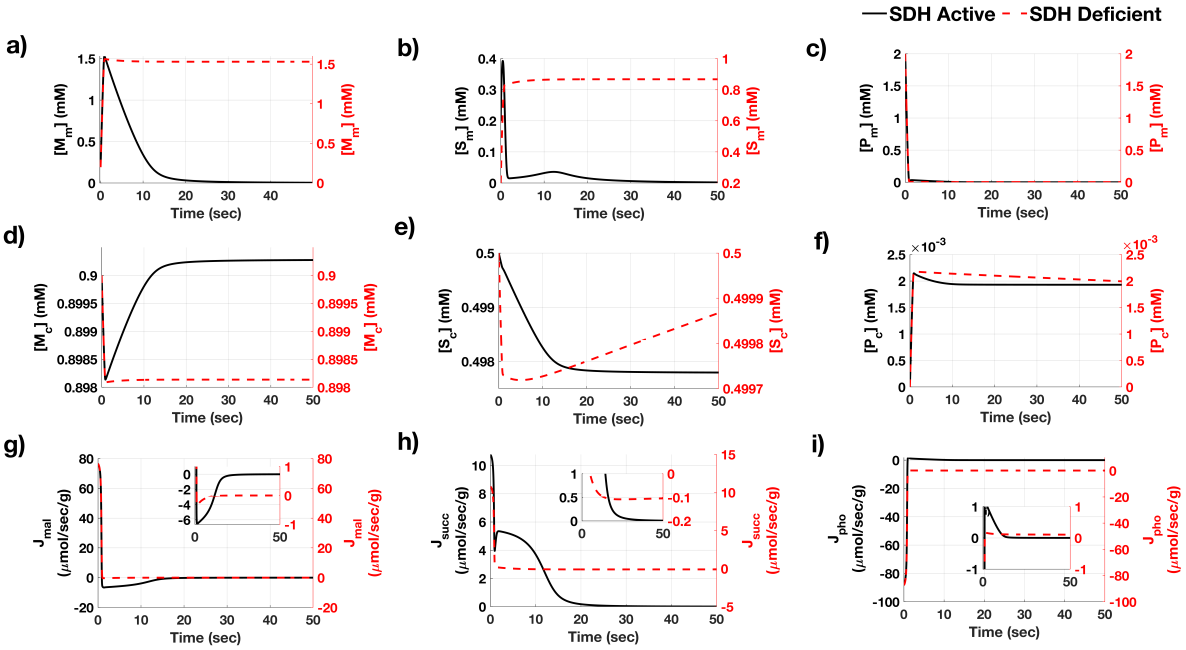

Figure 16: Comparison of metabolite concentration and flux profiles under SDH-active and SDH-deficient conditions in the intact-mitochondria setting. Time courses are shown for SDH-active (solid black) and SDH deficient (red dashed) simulations. (a–c) Matrix concentrations of malate $[M_m]$, succinate $[S_m]$, and phosphate $[P_m]$. (d–f) External-compartment concentrations $[M_c]$, $[S_c]$, and $[P_c]$. (g–i) Corresponding SLC25A10 flux components: malate flux J_{mal}, succinate flux J_{succ}, and phosphate flux J_{pho}. Initial matrix concentrations and compartment volumes follow Table 1; initial external concentrations are $[M_c] = 0.908$ mM, $[S_c] = 0.5$ mM, and $[P_c] = 10^{-12}$ mM (to avoid division by zero in gradient calculations). Kinetic parameters are fixed at the posterior modes from Table 4. SDH deficiency is implemented by setting the SDH flux to zero ($J_{\text{SDH}} = 0$) while keeping all other model components unchanged.

controls (see Appendix Appendix F for detailed methods). The data revealed significant alterations in intracellular succinate levels attributable to SLC25A10 deficiency. As shown in Fig. 17, succinate accumulated markedly in SLC25A10-KD cells relative to controls, consistent with impaired succinate efflux.

Overall, these simulations and measurements support a coherent picture in which SDH activity sets the dominant metabolic context for matrix succinate buffering, while SLC25A10 provides a rapid, phosphate-coupled exchange route that can mitigate succinate burden depending on the prevailing gradients and counter-substrate availability. Although this framework is deliberately simplified and is intended only to mimic the interplay between the SDH and SCAS enzymes and the SLC25A10 transporter in an isolated intact-mitochondria experimental setting (without incorporating the full set of TCA-cycle reactions or other transporters), it nonetheless extends the experimental observations by providing a mechanistic explanation for how SLC25A10 contributes to succinate handling under SDH deficiency, highlighting its potential role as both a gatekeeper and a pressure-release valve for matrix succinate levels.

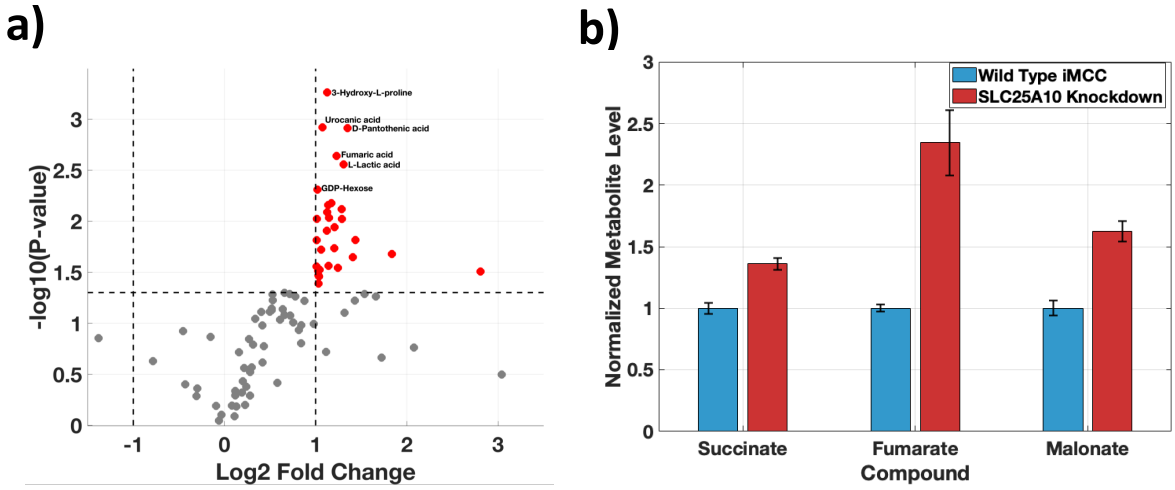

Figure 17: Targeted metabolomics shows increased dicarboxylate-related metabolite levels in SLC25A10 knockdown immortalized murine chromaffin cells (imCCs). (a) Volcano plot summarizing differential metabolite analysis between SLC25A10 knockdown and wild-type imCCs. Red points indicate metabolites that increase significantly in the knockdown condition (e.g., succinate, fumarate, and malonate), while grey points denote non-significant changes (dashed lines indicate the fold-change and significance thresholds used in the analysis). **(b)** Normalized metabolite levels for succinate, fumarate, and malonate in wild-type (blue) and SLC25A10 knockdown (red) imCCs, showing higher levels in the knockdown condition.

5 Discussion and Conclusion

In this study, we developed the first mechanistically derived and thermodynamically consistent kinetic model of the mitochondrial dicarboxylate carrier SLC25A10, based on the ping–pong mechanism. Our framework incorporates competitive binding, conformational bias weights, and thermodynamic constraints, allowing the model to quantitatively reproduce experimental transport assays while providing mechanistic insights into regimes that remain experimentally inaccessible.

The strengths of the framework extend beyond parameter estimation. Structural identifiability analysis clarified which parameters can be determined from experimental outputs and guided reparameterization. Bayesian inference enabled statistically rigorous calibration of kinetic parameters with credible intervals, separately for intact-mitochondria uptake assays and reconstituted proteoliposome experiments, that quantify uncertainty. Thermodynamic validation ensured compliance with physical laws, confirming that fluxes, Gibbs free energy, and equilibrium concentrations converge consistently. Together, these analyses establish a robust and generalizable modeling platform for mitochondrial carriers of the SLC25 family.

Several kinetic models of SLC25A10 have been proposed previously, including those by Bazil et al. [15] and Zhang et al. [16]. These models incorporate competitive binding, reversibility, heteroexchange, and thermodynamic consistency, but they rely on the assumption of a sequential transport mechanism. Such models are calibrated using classical transport assays [23, 20] and employ the King–Altman method [30] to derive rate equations. While conceptually valuable, this approach simplifies kinetics and lacks mechanistic depth. Recent structural and biophysical evidence, however, demonstrates that SLC25A10 is monomeric with a single binding site, consistent with a ping–pong mecha-

nism [1]. Our work therefore advances the field by explicitly embedding this mechanism into a thermodynamically consistent kinetic framework.

A central innovation of the model is the introduction of conformational bias weights, λ_{21} and λ_{31}, which quantify the relative influence of malate versus succinate and phosphate versus succinate, respectively. Together with the ratio ϕ (Eq. (4)), these parameters determine the directional preference of SLC25A10 by defining which substrate and which side of the membrane most strongly bias initiation of the transport cycle. Values near unity indicate equal competition, values below unity indicate succinate dominance, and values above unity indicate bias toward malate or phosphate. From a flux perspective, J_{succ} and J_{mal} depend directly on λ_{21}, while phosphate flux is shaped by λ_{31}. These bias weights thus provide a mechanistic lens for dissecting competitive exchange dynamics beyond what can be inferred from King–Altman–based formulations.

The inferred posterior summaries show that core capacity and dicarboxylate-affinity parameters are more tightly constrained by uptake data than phosphate-related effects and conformational weighting. In the intact-mitochondria calibration, the maximum transport capacity parameters for succinate (T^s_{max}), and malate (T^m_{max}), and the affinity parameters for succinate (K^s_m), malate (K^m_m), and phosphate (K^p_m) exhibit well-behaved, comparatively narrow posteriors, whereas the coupling ratios λ_{21}, and λ_{31} remain less sharply identified (Fig. 4). In the proteoliposome calibration, the malate branch is most strongly constrained K^m_m, and T^m_{max}, while phosphate affinity and phosphate-related weighting retain broader uncertainty, consistent with limited information content in the available measurements for isolating phosphate-dependent effects (Fig. 5). Biologically, these posteriors support robust inference of the overall rate scale and dicarboxylate binding under both assay types, while indicating that conclusions about phosphate weighting are more assay-dependent and would benefit from targeted experiments designed to separately excite phosphate-sensitive degrees of freedom.

Another strength of our framework is its ability to provide mechanistic insight into heteroexchange behavior that is difficult to infer from classical uptake assays [3, 23]. Conventional experiments report bulk uptake or exchange rates and do not directly resolve compartment concentrations or the microscopic carrier-state transients. In our model, flux trajectories are therefore computed as time-varying outputs of the reduced (rapid-equilibrium) transporter formulation, driven by the evolving matrix and external concentrations in the coupled mass-balance system (Fig. 12 and Fig. 13). Under these assumptions, simulations predict that phosphate efflux can support net dicarboxylate uptake early in the trajectory, with competition between malate and succinate shaping the relative flux contributions, and that the flux magnitudes diminish as concentration gradients relax toward equilibrium. Accordingly, the framework bridges a practical gap by enabling quantitative analysis of exchange driving forces and coordinated dicarboxylate–phosphate fluxes within a thermodynamically consistent (Fig. 10 and Fig. 11).

The simulations also highlight how mitochondrial morphology can modulate SLC25A10 activity under the intact-mitochondria coupled-volume constraint (Fig. 14). When the total normalized volume per gram protein is held fixed, matrix swelling, modestly increases the initial dicarboxylate flux components and increases the overall initial transport magnitude J_{tot}, with a correspondingly larger phosphate counter-flux of opposite sign. Conversely, matrix condensation reduces the initial flux components and decreases J_{tot}. Mechanistically, these trends arise from how coupled volume redistribution reshapes the early-time evolution of concentration gradients and saturation terms in the reduced

flux expressions, rather than from changes in intrinsic binding parameters (which are held fixed). These results are consistent with the broader view that crista geometry and compartment volumes influence carrier-driven transients and effective driving forces [26, 29], linking mitochondrial structure to short-timescale metabolic exchange capacity.

We also examined how metabolic context modulates transporter behavior by coupling the intact-mitochondria-calibrated exchange model to SDH and SCAS fluxes as a minimal succinate control loop. This framework is deliberately simplified and is intended only to mimic the interplay between SDH, SCAS, and SLC25A10 in an isolated intact-mitochondria experimental setting, without incorporating the full set of TCA-cycle reactions or other transporters. In this SLC25A10-coupled SDH–SCAS reduced exchange model, SDH activity strongly conditions matrix succinate buffering: when SDH is active, imported or SCAS-generated succinate is efficiently removed, leading to low sustained $[S_m]$; when SDH is absent, $[S_m]$ remains elevated because the dominant sink is removed. In both conditions, the carrier-mediated exchange fluxes are transient and relax rapidly toward near-equilibrium over the simulated time window, indicating that the most persistent signature of SDH loss in this reduced setting is elevated matrix succinate rather than sustained long-term net succinate export.

Within this module, phosphate availability couples succinate production and exchange because SCAS consumes inorganic phosphate and SLC25A10 requires phosphate counter-transport. Malate shapes succinate handling indirectly by modulating SDH throughput when SDH is active and by competing with succinate for phosphate-coupled exchange when SDH is absent. Moreover, targeted metabolomics in SLC25A10 knockdown chromaffin cells shows increased succinate levels relative to controls (Fig. 17), consistent with impaired succinate handling when transporter activity is reduced. Together, these results support the view that SLC25A10 can act as a rapid, phosphate-coupled exchange route that modulates succinate burden in SDH-deficient contexts, which are relevant to pseudo-hypoxic signaling where succinate can inhibit prolyl hydroxylases and stabilize HIF-1α [54, 12, 13, 38].

Despite these advances, the model has limitations. A key constraint in parameter estimation is the remaining uncertainty in the coupling ratios, particularly λ_{21} and λ_{31}, which are less directly informed by the available uptake assays than the core capacity and dicarboxylate-affinity parameters. In the intact-mitochondria calibration, λ_{21} exhibits a strongly right-skewed posterior with most mass at small values and a long upper tail, indicating that the data favor succinate-dominant weighting while still permitting malate-favored regimes. The posterior for λ_{31} is comparatively broad and right-tailed, reflecting weaker practical identifiability of phosphate weighting relative to succinate under these conditions. By contrast, the proteoliposome calibration concentrates both coupling ratios at small values (especially λ_{31}), but phosphate-related quantities (notably K_m^p) remain weakly constrained, suggesting that this dataset provides limited information to disentangle phosphate affinity from phosphate-weighting effects. Overall, these posteriors indicate that conclusions about relative substrate weighting are more assay-dependent and less identifiable than the transport-rate scale and dicarboxylate binding parameters, motivating future experiments specifically designed to better isolate phosphate-coupled competition effects.

While a common benchmark for Monte Carlo precision is $\mathrm{MCSE}/\Sigma < 0.10$, most parameters in the intact-mitochondria calibration satisfy this criterion (Table 6). The largest relative Monte Carlo errors occur for λ_{21} ($\mathrm{MCSE}/\Sigma = 0.127$), λ_{31} (0.102), and K_m^p (0.092),

indicating that the coupling ratios and phosphate affinity are the least precisely estimated quantities under these uptake-assay conditions. Importantly, this behavior is not consistent with non-convergence: all $\hat{R}$ values remain close to 1.0, and the effective sample sizes are in the several-thousand range ($N_{\text{eff}} \approx$ 4,970–8,156). We therefore interpret the slightly elevated MCSE/Σ values as a consequence of limited data informativeness and posterior dependence structure (e.g., correlations among phosphate-related parameters and coupling ratios), rather than as a limitation of the Metropolis–Hastings sampler. Overall, the diagnostics support numerically stable posterior summaries for inference, while highlighting directions in parameter space where more informative experiments (e.g., designs that better isolate phosphate-coupled competition) could further reduce uncertainty and Monte Carlo error.

Beyond this, our Bayesian calibration adopts simplifying assumptions about both the likelihood and the priors. For the likelihood, we assume independent, identically distributed Gaussian errors on the flux measurements; in practice, experimental errors and model–data discrepancy may be heteroskedastic (larger fluxes often exhibit larger variance), correlated across conditions within an assay, or non-Gaussian (e.g., due to detection limits and instrumental drift), which could affect posterior uncertainty and potentially bias estimates. Nevertheless, we adopt this Gaussian error model to enable tractable likelihood evaluation and parameter inference, and we view the present work as a foundation for future calibration methods that incorporate more realistic error structures.

For the priors, we use Gaussian priors for the intact-mitochondria capacity and affinity parameters, while assigning uniform priors to the coupling ratios and σ^2; in the proteoliposome setting, we use uniform priors for all inferred parameters. These choices maintain tractability and reflect differences in available prior information, and future work with richer datasets could support hierarchical priors and more informative, data-driven prior specifications.

Additionally, the distribution of dicarboxylates and phosphate among their protonation (and, where relevant, metal-bound) species depends on pH and ionic conditions, which can influence the concentrations of the transporter-relevant charged forms (e.g. $HPO_4{}^{2-}$). In the present work, we model transport under the experimental assay conditions, where pH and buffer composition are controlled and effectively constant; accordingly, speciation is treated as fixed and its effect is absorbed into the inferred effective kinetic parameters (e.g., K_m parameters and $T_{\max}$). Incorporating explicit pH-dependent speciation (and cation binding) would be most informative when datasets spanning multiple pH values and ionic conditions are available, enabling those additional degrees of freedom to be constrained rather than introducing non-identifiable parameters.

Moreover, several modeling assumptions limit the scope of the present framework. First, while the model is mechanistically grounded in a ping–pong scheme, we employ a reduced rapid-equilibrium treatment of the carrier complex (fast binding/unbinding), which collapses intermediate carrier-state transients and may miss finer regulatory steps or additional conformational intermediates. Relatedly, parameter lumping in the reduced flux expressions can mask asymmetries between binding and release kinetics that would be resolvable only with richer time-resolved datasets.

Second, the SDH–SCAS coupling is implemented as a minimal succinate control loop with fixed enzyme fluxes adopted from the literature rather than jointly re-estimated, so quantitative predictions of the coupled dynamics are sensitive to these prescribed rates and to omitted reactions in the full TCA network. Third, compartments are treated as well-

mixed volumes, neglecting sub-mitochondrial microdomains, diffusion limitations, and interactions with other carriers that could be important in highly structured mitochondria. Finally, calibration relies on isolated uptake assays (intact mitochondria and proteoliposomes) under controlled buffer conditions; tissue-specific regulation, post-translational modifications, and in vivo substrate gradients are not represented, which limits direct translatability to physiological and pathological settings. Future work should integrate additional carrier states, broader metabolic coupling, and spatially resolved compartmentalization within whole-mitochondrion models, supported by more diverse experimental measurements.

A further limitation concerns the interpretation of the targeted metabolomics data used to contextualize the model. The measured metabolite abundances reflect whole-cell pools and therefore conflate mitochondrial, cytosolic, and other subcellular contributions. Moreover, SLC25A10 perturbation can induce broad proteome remodeling and compensatory pathway reprogramming [55], so changes in succinate, malate, or phosphate levels cannot be attributed uniquely to a single transport step. As a result, metabolomics alone cannot determine the in vivo directionality or mechanistic mode of SLC25A10 exchange, nor can it provide a thermodynamic constraint without compartment-resolved concentrations. Robust inference of net transport direction from free-energy considerations would require measurements of matrix versus external concentrations under matched conditions, which are not available in the present dataset. Accordingly, we treat the metabolomics results as qualitative consistency checks and motivation, rather than as direct mechanistic validation of the transport model.

In conclusion, we present a mechanistically derived and thermodynamically consistent kinetic model of the mitochondrial dicarboxylate carrier SLC25A10 grounded in a ping–pong, single-binding-site mechanism. Using a reduced rapid-equilibrium flux formulation with Bayesian calibration to both intact-mitochondria uptake assays and proteoliposome data, the model quantitatively reproduces the measured exchange kinetics. The calibrated framework captures competitive coupling between succinate, malate, and phosphate, and shows that morphology-induced volume redistribution can systematically modulate early exchange capacity by reshaping how concentration gradients evolve.

When embedded in a simplified SLC25A10-coupled SDH and SCAS reduced exchange model, the simulations highlight how SDH activity conditions the metabolic context for succinate buffering. Together with targeted metabolomics in SLC25A10 knockdown chromaffin cells showing succinate accumulation, these results support a coherent picture in which SLC25A10 provides a fast, phosphate-coupled exchange route that can mitigate succinate burden depending on prevailing gradients and counter-substrate availability. Beyond reproducing classical transport assays, the framework generates testable predictions and provides a foundation for integrative studies of mitochondrial carrier dynamics, linking transporter behavior to broader physiological and pathological processes—including cancer metabolism and conditions in which these metabolites are dysregulated, such as ischemia. More broadly, our approach offers a transferable workflow—mechanistic reduction, identifiability analysis, Bayesian inference, and thermodynamic validation—that can be adapted to other SLC25 carriers to connect structure-informed transport mechanisms to quantitative, experimentally grounded mitochondrial transport dynamics.

References

[1] Camila Cimadamore-Werthein et al. "Human mitochondrial carriers of the SLC25 family function as monomers exchanging substrates with a ping-pong kinetic mechanism". In: *EMBO Journal* (2024). ISSN: 14602075. DOI: 10.1038/s44318-024-00150-0.

[2] Edmund R.S. Kunji et al. "The SLC25 carrier family: Important transport proteins in mitochondrial physiology and pathology". In: *Physiology* 35 (5 Sept. 2020), pp. 302–327. ISSN: 15489221. DOI: 10.1152/physiol.00009.2020.

[3] Ferdinando Palmieri et al. "Kinetic Study of the Dicarboxylate Carrier in Rat Liver Mitochondria". In: *European Journal of Biochemistry* 22 (1 1971), pp. 66–74. ISSN: 14321033. DOI: 10.1111/j.1432-1033.1971.tb01515.x.

[4] Luc Rochette et al. *Mitochondrial SLC25 carriers: Novel targets for cancer therapy.* May 2020. DOI: 10.3390/molecules25102417.

[5] Adrian Casas-Benito, Sonia Martínez-Herrero, and Alfredo Martínez. *Succinate-Directed Approaches for Warburg Effect-Targeted Cancer Management, an Alternative to Current Treatments?* May 2023. DOI: 10.3390/cancers15102862.

[6] Amer Ahmed et al. *The Role of Mitochondrial Solute Carriers SLC25 in Cancer Metabolic Reprogramming: Current Insights and Future Perspectives.* Jan. 2025. DOI: 10.3390/ijms26010092.

[7] Eva Pyrihová et al. "A mitochondrial carrier transports glycolytic intermediates to link cytosolic and mitochondrial glycolysis in the human gut parasite Blastocystis". In: *eLife* 13 (May 2024). ISSN: 2050084X. DOI: 10.7554/ELIFE.94187.

[8] Shinji Mizuarai et al. "Identification of dicarboxylate carrier Slc25a10 as malate transporter in de Novo fatty acid synthesis". In: *Journal of Biological Chemistry* 280 (37 Sept. 2005), pp. 32434–32441. ISSN: 00219258. DOI: 10.1074/jbc.M503152200.

[9] Charlotte Lussey-Lepoutre et al. *Mitochondrial deficiencies in the predisposition to paraganglioma.* June 2017. DOI: 10.3390/metabo7020017.

[10] Julian Hlouschek et al. "Targeting SLC25A10 alleviates improved antioxidant capacity and associated radioresistance of cancer cells induced by chronic-cycling hypoxia". In: *Cancer Letters* 439 (Dec. 2018), pp. 24–38. ISSN: 18727980. DOI: 10.1016/j.canlet.2018.09.002.

[11] Ferdinando Palmieri, Pasquale Scarcia, and Magnus Monné. *Diseases caused by mutations in mitochondrial carrier genes SLC25: A review.* Apr. 2020. DOI: 10.3390/biom10040655.

[12] Katarina Kluckova and Daniel A Tennant. "Metabolic implications of hypoxia and pseudohypoxia in pheochromocytoma and paraganglioma". In: *Cell and tissue research* 372 (2018), pp. 367–378.

[13] Katarína Kľučková et al. "Succinate dehydrogenase deficiency in a chromaffin cell model retains metabolic fitness through the maintenance of mitochondrial nadh oxidoreductase function". In: *FASEB Journal* 34 (1 2020), pp. 303–315. ISSN: 15306860. DOI: 10.1096/fj.201901456R.

[14] Elías Vera-Sigüenza et al. *A Mathematical Exploration of SDH-b Loss in Chromaffin Cells*. July 2024. DOI: 10.1101/2024.07.15.603520. URL: http://biorxiv.org/lookup/doi/10.1101/2024.07.15.603520.

[15] Jason N. Bazil, Gregery T. Buzzard, and Ann E. Rundell. "Modeling mitochondrial bioenergetics with integrated volume dynamics". In: *PLoS Computational Biology* 6 (1 2010). ISSN: 15537358. DOI: 10.1371/journal.pcbi.1000632.

[16] Xiao Zhang et al. "Integrated computational model of the bioenergetics of isolated lung mitochondria". In: *PLoS ONE* 13 (6 June 2018). ISSN: 19326203. DOI: 10.1371/journal.pone.0197921.

[17] Shima Sadri et al. "Computational Modeling of Substrate-Dependent Mitochondrial Respiration and Bioenergetics in the Heart and Kidney Cortex and Outer Medulla". In: *Function* 4 (5 2023). ISSN: 26338823. DOI: 10.1093/function/zqad038.

[18] Jonathan J. Ruprecht and Edmund R. S. Kunji. "Structural Mechanism of Transport of Mitochondrial Carriers." In: *Annual review of biochemistry* (2021). URL: https://api.semanticscholar.org/CorpusID:231874184.

[19] Vasiliki Mavridou et al. "Substrate binding in the mitochondrial ADP/ATP carrier is a step-wise process guiding the structural changes in the transport cycle". In: *Nature Communications* 13 (1 Dec. 2022). ISSN: 20411723. DOI: 10.1038/s41467-022-31366-5.

[20] F. Palmieri. *Mitochondrial carrier proteins*. June 1994. DOI: 10.1016/0014-5793(94)00329-7.

[21] R. N. Johnson and J. Brian Chappell. "The transport of inorganic phosphate by the mitochondrial dicarboxylate carrier." In: *The Biochemical journal* 134 3 (1973), pp. 769–74. URL: https://api.semanticscholar.org/CorpusID:22142227.

[22] Faustino Bisaccia, Cesare Indiveri, and Ferdinando Palmieri. "Purification and reconstitution of two anion carriers from rat liver mitochondria: the dicarboxylate and the 2-oxoglutarate carrier." In: *Biochimica et biophysica acta* 933 2 (1988), pp. 229–40. URL: https://api.semanticscholar.org/CorpusID:25273025.

[23] Cesare Indiveri et al. "Kinetics of the reconstituted dicarboxylate carrier from rat liver mitochondria." In: *Biochimica et biophysica acta* 977 2 (1989), pp. 187–93. URL: https://api.semanticscholar.org/CorpusID:1667771.

[24] Cesare Indiveri et al. "Kinetic discrimination of two substrate binding sites of the reconstituted dicarboxylate carrier from rat liver mitochondria." In: *Biochimica et biophysica acta* 977 2 (1989), pp. 194–9. URL: https://api.semanticscholar.org/CorpusID:40809880.

[25] Emmet A Francis et al. "Spatial modeling algorithms for reactions and transport in biological cells". en. In: *Nat. Comput. Sci.* 5.1 (Jan. 2025), pp. 76–89.

[26] Guadalupe C Garcia et al. "Mitochondrial morphology provides a mechanism for energy buffering at synapses". en. In: *Sci. Rep.* 9.1 (Dec. 2019), p. 18306.

[27] Sabzali Javadov, Xavier Chapa-Dubocq, and Vladimir Makarov. "Different approaches to modeling analysis of mitochondrial swelling". In: *Mitochondrion* 38 (Jan. 2018), pp. 58–70.

[28] Raquel Adams et al. "How the topology of the mitochondrial inner membrane modulates ATP production". en. In: *Cells* 14.4 (Feb. 2025), p. 257.

[29] Nasrin Afzal et al. "Effect of crista morphology on mitochondrial ATP output: A computational study". en. In: *Curr. Res. Physiol.* 4 (Apr. 2021), pp. 163–176.

[30] Edward L. King and Carl Altman. "A Schematic Method of Deriving the Rate Laws for Enzyme-Catalyzed Reactions". In: *The Journal of Physical Chemistry* 60 (1956), pp. 1375–1378. URL: https://api.semanticscholar.org/CorpusID:101759412.

[31] Lucy R. Forrest, Reinhard Krämer, and Christine Ziegler. "The structural basis of secondary active transport mechanisms." In: *Biochimica et biophysica acta* 1807 2 (2011), pp. 167–88. URL: https://api.semanticscholar.org/CorpusID:10803966.

[32] Jonathan J. Ruprecht and Edmund R.S. Kunji. *The SLC25 Mitochondrial Carrier Family: Structure and Mechanism.* Mar. 2020. DOI: 10.1016/j.tibs.2019.11.001.

[33] Alex Berlaga and Anatoly B. Kolomeisky. "Molecular Mechanisms of Active Transport in Antiporters: Kinetic Constraints and Efficiency". In: *Journal of Physical Chemistry Letters* 12 (39 Oct. 2021), pp. 9588–9594. ISSN: 19487185. DOI: 10.1021/acs.jpclett.1c02846.

[34] Alex Berlaga and Anatoly B. Kolomeisky. "Understanding Mechanisms of Secondary Active Transport by Analyzing the Effects of Mutations and Stoichiometry". In: *Journal of Physical Chemistry Letters* 13 (24 June 2022), pp. 5405–5412. ISSN: 19487185. DOI: 10.1021/acs.jpclett.2c01232.

[35] Alex Berlaga and Anatoly B. Kolomeisky. "Theoretical study of active secondary transport: Unexpected differences in molecular mechanisms for antiporters and symporters". In: *Journal of Chemical Physics* 156 (8 Feb. 2022). ISSN: 10897690. DOI: 10.1063/5.0082589.

[36] Roger Springett et al. "Modelling the free energy profile of the mitochondrial ADP/ATP carrier". In: *Biochimica et Biophysica Acta - Bioenergetics* 1858 (11 Nov. 2017), pp. 906–914. ISSN: 18792650. DOI: 10.1016/j.bbabio.2017.05.006.

[37] James Keener and James Sneyd. *Mathematical Physiology II: Systems Physiology.* Springer, 2009.

[38] Elías Vera-Sigüenza et al. "A mathematical exploration of SDH-b loss in chromaffin cells". en. In: *Bull. Math. Biol.* 87.4 (Mar. 2025), p. 53.

[39] Eric J. Harris and Karel van Dam. "Changes of total water and sucrose space accompanying induced ion uptake or phosphate swelling of rat liver mitochondria." In: *The Biochemical journal* 106 3 (1968), pp. 759–66. URL: https://api.semanticscholar.org/CorpusID:37995416.

[40] Cesare Indiveri et al. "Kinetic characterization of the reconstituted dicarboxylate carrier from mitochondria: a four-binding-site sequential transport system." In: *Biochimica et biophysica acta* 1143 3 (1993), pp. 310–8. URL: https://api.semanticscholar.org/CorpusID:8502488.

[41] Alejandro F. Villaverde et al. "A protocol for dynamic model calibration". In: *Briefings in Bioinformatics* 23 (1 Jan. 2022). ISSN: 14774054. DOI: 10.1093/bib/bbab387.

[42] Alejandro F. Villaverde, Antonio Barreiro, and Antonis Papachristodoulou. "Structural Identifiability of Dynamic Systems Biology Models". In: *PLoS Computational Biology* 12 (10 Oct. 2016). ISSN: 15537358. DOI: 10.1371/journal.pcbi.1005153.

[43] William Squire and George Trapp. "Using complex variables to estimate derivatives of real functions". In: *SIAM Rev. Soc. Ind. Appl. Math.* 40.1 (Jan. 1998), pp. 110–112.

[44] Hanwen Huang, Andreas Handel, and Xiao Song. "A Bayesian approach to estimate parameters of ordinary differential equation". In: *Computational Statistics* 35 (3 Sept. 2020), pp. 1481–1499. ISSN: 16139658. DOI: 10.1007/s00180-020-00962-8.

[45] Christophe Andrieu et al. "On the utility of Metropolis-Hastings with asymmetric acceptance ratio". In: (Mar. 2018). URL: http://arxiv.org/abs/1803.09527.

[46] Aki Vehtarh et al. "Rank-Normalization, Folding, and Localization: An Improved (Formula presented) for Assessing Convergence of MCMC (with Discussion)*†". In: *Bayesian Analysis* 16 (2 2021), pp. 667–718. ISSN: 19316690. DOI: 10.1214/20-BA1221.

[47] Andrew Gelman et al. *Bayesian Data Analysis*. 3rd. London: Chapman & Hall/CRC, 2013.

[48] Bob Carpenter et al. "Stan: A probabilistic programming language". In: *Journal of Statistical Software* 76 (1 2017). ISSN: 15487660. DOI: 10.18637/jss.v076.i01.

[49] Ying Liu, Dootika Vats, and James M. Flegal. "Batch Size Selection for Variance Estimators in MCMC". In: *Methodology and Computing in Applied Probability* 24 (1 Mar. 2022), pp. 65–93. ISSN: 15737713. DOI: 10.1007/s11009-020-09841-7.

[50] Andrew Gelman and Donald B. Rubin. "Inference from Iterative Simulation Using Multiple Sequences". In: *Statistical Science* 7 (1992), pp. 457–472. URL: https://api.semanticscholar.org/CorpusID:14661921.

[51] P. Stephen et al. "General methods for monitoring convergence of iterative simulations". In: *Journal of Computational and Graphical Statistics* 7 (1998), pp. 434–455. URL: https://api.semanticscholar.org/CorpusID:7300890.

[52] Stefan J. Jol et al. "Thermodynamic calculations for biochemical transport and reaction processes in metabolic networks". In: *Biophysical Journal* 99 (10 Nov. 2010), pp. 3139–3144. ISSN: 15420086. DOI: 10.1016/j.bpj.2010.09.043.

[53] X. Li et al. "A database of thermodynamic quantities for the reactions of glycolysis and the tricarboxylic acid cycle". In: *Journal of Physical Chemistry B* 114 (49 Dec. 2010), pp. 16068–16082. ISSN: 15205207. DOI: 10.1021/jp911381p.

[54] G. M. Tannahill et al. "Succinate is an inflammatory signal that induces IL-1 through HIF-1". In: *Nature* 496 (7444 Apr. 2013), pp. 238–242. ISSN: 00280836. DOI: 10.1038/nature11986.

[55] Xiaoshan Zhou et al. "The mitochondrial carrier SLC25A10 regulates cancer cell growth". In: *Oncotarget* 6 (2015), pp. 9271–9283. URL: https://api.semanticscholar.org/CorpusID:1570957.

[56] W. Wallace Cleland. "Derivation of rate equations for multisite ping-pong mechanisms with ping-pong reactions at one or more sites." In: *The Journal of biological chemistry* 248 24 (1973), pp. 8353–5. URL: https://api.semanticscholar.org/CorpusID:26861029.

[57] Eric Letouzé et al. "SDH mutations establish a hypermethylator phenotype in paraganglioma". In: *Cancer cell* 23.6 (2013), pp. 739–752.

Data Availability

The core MATLAB codes supporting this study are publicly available on GitHub: https://github.com/rxn315/MATHEMATICAL_MODEL_SLC25A10_REVISED.git. Due to file-size limitations, the full reproducibility package (including scripts used to generate all figures and tables in the revised manuscript) is archived on Zenodo: (DOI: https://doi.org/10.5281/zenodo.18664645).

Acknowledgments

ES was supported by a Cancer Research UK grant (C42109/A24757). YL was supported by The Paradifference Foundation. FS was supported by a UKRI Future Leaders Fellowship (MR/T043571/1). We acknowledge that we used ChatGPT to refine and enhance the clarity of this article. However, all ideas and content are our own, and we take full responsibility for the final submission. Additionally, I acknowledge the use of BioRender in creating some of the scientific illustrations for this article.

Author Contributions

Ramin Nashebi: Mathematical model conceptualisation, computational methodology, software, visualisation, model validation, model analysis, writing, and editing.

Yingying Liu: Experimental data procurement and writing the description of the experimental work.

Elías Vera-Sigüenza: Model Validation, model analysis, article review.

Daniel A. Tennant: Conceptualisation, experimental data validation, article review, and editing.

Fabian Spill: Mathematical model conceptualisation, model validation, article review and editing, supervised and managed the study.

Appendix A Full ODE System for SLC25A10 Ping–Pong Model

The complete set of ordinary differential equations (ODEs) governing transporter states, complexes, and metabolite concentrations is:

$$\frac{d[T_m]}{dt} = -k_1^s[T_m][S_m] + k_{-1}^s[T_mS] - k_1^m[T_m][M_m] + k_{-1}^m[T_mM] + k_{-3}^p[T_mP] - k_3^p[T_m][P_m], \tag{A.1}$$

$$\frac{d[T_mS]}{dt} = k_1^s[T_m][S_m] - k_{-1}^s[T_mS] - k_c^s[T_mS] + k_{-c}^s[T_cS], \tag{A.2}$$

$$\frac{d[T_mM]}{dt} = k_1^m[T_m][M_m] - k_{-1}^m[T_mM] - k_c^m[T_mM] + k_{-c}^m[T_cM], \tag{A.3}$$

$$\frac{d[T_cS]}{dt} = k_c^s[T_mS] - k_{-c}^s[T_cS] - k_{-3}^s[T_cS] + k_3^s[T_c][S_c], \tag{A.4}$$

$$\frac{d[T_cM]}{dt} = k_c^m[T_mM] - k_{-c}^m[T_cM] - k_{-3}^m[T_cM] + k_3^m[T_c][M_c], \tag{A.5}$$

$$\frac{d[T_cP]}{dt} = k_1^p[T_c][P_c] - k_{-1}^p[T_cP] - k_c^p[T_cP] + k_{-c}^p[T_mP], \tag{A.6}$$

$$\frac{d[T_mP]}{dt} = k_c^p[T_cP] - k_{-c}^p[T_mP] - k_{-3}^p[T_mP] + k_3^p[T_m][P_m], \tag{A.7}$$

$$\frac{d[T_c]}{dt} = -k_1^p[T_c][P_c] + k_{-1}^p[T_cP] + k_{-3}^s[T_cS] - k_3^s[T_c][S_c] + k_{-3}^m[T_cM] - k_3^m[T_c][M_c], \tag{A.8}$$

$$\frac{d[S_m]}{dt} = \frac{1}{\tilde{V}_m}\Big(- k_1^s[T_m][S_m] + k_{-1}^s[T_mS]\Big), \tag{A.9}$$

$$\frac{d[M_m]}{dt} = \frac{1}{\tilde{V}_m}\Big(- k_1^m[T_m][M_m] + k_{-1}^m[T_mM]\Big), \tag{A.10}$$

$$\frac{d[S_c]}{dt} = \frac{1}{\tilde{V}_c}\Big(k_{-3}^s[T_cS] - k_3^s[T_c][S_c]\Big), \tag{A.11}$$

$$\frac{d[M_c]}{dt} = \frac{1}{\tilde{V}_c}\Big(k_{-3}^m[T_cM] - k_3^m[T_c][M_c]\Big), \tag{A.12}$$

$$\frac{d[P_c]}{dt} = \frac{1}{\tilde{V}_c}\Big(- k_1^p[T_c][P_c] + k_{-1}^p[T_cP]\Big), \tag{A.13}$$

$$\frac{d[P_m]}{dt} = \frac{1}{\tilde{V}_m}\Big(k_{-3}^p[T_mP] - k_3^p[T_m][P_m]\Big). \tag{A.14}$$

Appendix B Symmetric Transport Assumption

We assume that the SLC25A10 transporter operates with symmetric kinetics [33, 34, 35]. Under this assumption, the elementary rate constants governing substrate binding/unbinding, conformational transitions, and substrate release have the same magnitudes when the carrier operates toward the mitochondrial matrix (m) or toward the external compartment (c).

Table 8: State variables in the SLC25A10 transport model.

Symbol	Description	Units
S_m	Succinate concentration in matrix	$\mathrm{mol\,L^{-1}}$
M_m	Malate concentration in matrix	$\mathrm{mol\,L^{-1}}$
P_m	Phosphate concentration in matrix	$\mathrm{mol\,L^{-1}}$
S_c	Succinate concentration in external compartment	$\mathrm{mol\,L^{-1}}$
M_c	Malate concentration in external compartment	$\mathrm{mol\,L^{-1}}$
P_c	Phosphate concentration in external compartment	$\mathrm{mol\,L^{-1}}$
T_m	Free transporter facing matrix	$\mathrm{mol\,g^{-1}}$
T_c	Free transporter facing external compartment	$\mathrm{mol\,g^{-1}}$
T_mS	Transporter–succinate complex facing matrix	$\mathrm{mol\,g^{-1}}$
T_mM	Transporter–malate complex facing matrix	$\mathrm{mol\,g^{-1}}$
T_cS	Transporter–succinate complex facing external side	$\mathrm{mol\,g^{-1}}$
T_cM	Transporter–malate complex facing external side	$\mathrm{mol\,g^{-1}}$
T_cP	Transporter–phosphate complex facing external side	$\mathrm{mol\,g^{-1}}$
T_mP	Transporter–phosphate complex facing matrix	$\mathrm{mol\,g^{-1}}$
T_{total}	Total transporter amount per gram protein	$\mathrm{mol\,g^{-1}}$

Note: L denotes liters, g denotes grams of protein, and mol denotes moles.

For example, for succinate, the matrix-side binding and release rates (k_1^s, k_{-1}^s) are assumed equal to the corresponding rates on the external side (k_3^s, k_{-3}^s):

$$k_1^s = k_3^s, \tag{B.1}$$

$$k_{-1}^s = k_{-3}^s. \tag{B.2}$$

Analogous relations hold for malate and phosphate, and for the associated conformational transition steps. This symmetry reduces the number of independent kinetic parameters, facilitates parameter estimation, and ensures that the transporter satisfies microscopic reversibility and detailed balance at equilibrium.

Appendix C Rapid–Equilibrium Assumption and Derivation of the Rate Equation

Appendix C.1 Forward Cycle

To derive the rate equations, we invoke the rapid–equilibrium assumption (REA) for substrate binding. In the context of carrier-mediated transport, REA assumes that substrate binding and release to/from the carrier are much faster than the conformational transitions of the loaded carrier, so that the binding steps can be treated as being at thermodynamic equilibrium [37]. The slow, rate-limiting steps are the translocation (ping–pong) transitions of the loaded carrier.

For succinate on the matrix side, the binding reaction

$$T_m + S_m \underset{k_{-1}^s}{\overset{k_1^s}{\rightleftharpoons}} T_mS$$

Table 9: Model parameters, definitions, and units.

Symbol	Description	Units
$\tilde{V}_m$	Matrix volume per gram protein (V_m/g)	$\mathrm{L\,g^{-1}}$
$\tilde{V}_c$	External volume per gram protein (V_c/g)	$\mathrm{L\,g^{-1}}$
V_m	Matrix compartment volume	L
V_c	External compartment volume	L
k_1^s	Succinate binding rate of matrix side	$\mathrm{L\,mol^{-1}\,s^{-1}}$
k_{-1}^s	Succinate unbinding rate of matrix side	$\mathrm{s^{-1}}$
k_3^s	Succinate binding rate of external side	$\mathrm{L\,mol^{-1}\,s^{-1}}$
k_{-3}^s	Succinate unbinding rate of external side	$\mathrm{s^{-1}}$
k_c^s	Conformational rate of succinate-loaded carrier	$\mathrm{s^{-1}}$
k_{-c}^s	Reverse conformational rate of succinate-loaded carrier	$\mathrm{s^{-1}}$
k_1^m	Malate binding rate of matrix side	$\mathrm{L\,mol^{-1}\,s^{-1}}$
k_{-1}^m	Malate unbinding rate of matrix side	$\mathrm{s^{-1}}$
k_3^m	Malate binding rate of external side	$\mathrm{L\,mol^{-1}\,s^{-1}}$
k_{-3}^m	Malate unbinding rate of external side	$\mathrm{s^{-1}}$
k_c^m	Conformational rate of malate-loaded carrier	$\mathrm{s^{-1}}$
k_{-c}^m	Reverse conformational rate of malate-loaded carrier	$\mathrm{s^{-1}}$
k_1^p	Phosphate binding rate of external side,	$\mathrm{L\,mol^{-1}\,s^{-1}}$
k_{-1}^p	Phosphate unbinding rate of external side	$\mathrm{s^{-1}}$
k_3^p	Phosphate binding rate of matrix side	$\mathrm{L\,mol^{-1}\,s^{-1}}$
k_{-3}^p	Phosphate unbinding rate of matrix side	$\mathrm{s^{-1}}$
k_c^p	Conformational rate of phosphate-loaded carrier	$\mathrm{s^{-1}}$
k_{-c}^p	Reverse conformational rate of phosphate-loaded carrier	$\mathrm{s^{-1}}$
K_m^x	Matrix side dissociation constant for $x \in \{s, m, p\}$	$\mathrm{mol\,L^{-1}}$
K_m^x	External side dissociation constant for $x \in \{s, m, p\}$	$\mathrm{mol\,L^{-1}}$
$T_{\max}^x$	Maximal Transport capacity for $x \in \{s, m, p\}$	$\mathrm{mol\,g^{-1}\,s^{-1}}$
λ_{21}	Conformational-bias ratio (malate vs. succinate weighting)	dimensionless
λ_{31}	Conformational-bias ratio (phosphate vs. succinate weighting)	dimensionless
ϕ	Weighted ratio of matrix to external substrate levels	dimensionless
δ_1	Matrix side saturation factor	dimensionless
δ_2	External side saturation factor	dimensionless

Note: L denotes liters, s denotes seconds, g denotes grams of protein, and mol denotes moles.

is assumed to be at equilibrium on the timescale of transport. Thus, the net rate of this binding step is zero:

$$k_1^s[T_m][S_m] - k_{-1}^s[T_m S] = 0, \tag{C.1}$$

which yields

$$[T_m S] = \frac{k_1^s}{k_{-1}^s}[T_m][S_m] = \frac{[T_m][S_m]}{K_m^s}, \tag{C.2}$$

where

$$K_m^s = \frac{k_{-1}^s}{k_1^s} \tag{C.3}$$

is the equilibrium dissociation constant for succinate on the matrix side. By symmetry of the carrier, the same dissociation constant applies on the external side,

$$T_c + S_c \underset{k_{-1}^s}{\overset{k_1^s}{\rightleftharpoons}} T_cS,$$

so that

$$[T_cS] = \frac{[T_c][S_c]}{K_m^s}. \tag{C.4}$$

The same reasoning applies to malate and phosphate. For malate,

$$T_m + M_m \underset{k_{-1}^m}{\overset{k_1^m}{\rightleftharpoons}} T_mM, \qquad T_c + M_c \underset{k_{-1}^m}{\overset{k_1^m}{\rightleftharpoons}} T_cM,$$

we obtain

$$[T_mM] = \frac{[T_m][M_m]}{K_m^m}, \qquad [T_cM] = \frac{[T_c][M_c]}{K_m^m}, \tag{C.5}$$

with

$$K_m^m = \frac{k_{-1}^m}{k_1^m}. \tag{C.6}$$

For phosphate,

$$T_c + P_c \underset{k_{-1}^p}{\overset{k_1^p}{\rightleftharpoons}} T_cP, \qquad T_m + P_m \underset{k_{-1}^p}{\overset{k_1^p}{\rightleftharpoons}} T_mP,$$

we obtain

$$[T_cP] = \frac{[T_c][P_c]}{K_m^p}, \qquad [T_mP] = \frac{[T_m][P_m]}{K_m^p}, \tag{C.7}$$

with

$$K_m^p = \frac{k_{-1}^p}{k_1^p}. \tag{C.8}$$

Under REA, the concentrations of the transporter–substrate complexes are therefore algebraic functions of the free transporter and substrate concentrations, as in (C.2), (C.5), and (C.7). The slow, rate–limiting steps in the forward cycle are the conformational transitions of the loaded carrier:

$$T_mS \underset{k_{-c}^s}{\overset{k_c^s}{\rightleftharpoons}} T_cS, \qquad T_mM \underset{k_{-c}^m}{\overset{k_c^m}{\rightleftharpoons}} T_cM, \qquad T_cP \underset{k_{-c}^p}{\overset{k_c^p}{\rightleftharpoons}} T_mP.$$

Appendix C.1.1 Intermediate product formation: v_1^f

Under REA, the reversible binding and unbinding of substrates to the carrier on either side of the membrane occur much faster than the conformational (ping–pong) transition of the loaded carrier. Thus, the conformational change is the rate-limiting step, and the dicarboxylate flux is governed by the net conversion of the matrix-facing complexes (T_mS, T_mM) into their external-facing counterparts (T_cS, T_cM).

Accordingly, the forward-cycle flux through the dicarboxylate leg can be written as the rate of formation of the external-facing loaded transporter states:

$$v_1^f = \frac{d[T_cS]}{dt} + \frac{d[T_cM]}{dt}. \tag{C.9}$$

Substituting the conformational transition rates for these processes yields

$$v_1^f = k_c^s[T_mS] - k_{-c}^s[T_cS] + k_c^m[T_mM] - k_{-c}^m[T_cM], \tag{C.10}$$

which represents the net forward flux through the rate-limiting conformational transitions of the loaded carrier.

Substituting the rapid–equilibrium expressions (C.2) and (C.5), we obtain

$$v_1^f = \left(\frac{k_c^s[T_m][S_m] - k_{-c}^s[T_c][S_c]}{K_m^s} + \frac{k_c^m[T_m][M_m] - k_{-c}^m[T_c][M_c]}{K_m^m} \right). \tag{C.11}$$

Under the symmetry assumption for the conformational transitions, this expression can be written in the compact form

$$v_1^f = \left(\frac{k_c^s\left([T_m][S_m] - [T_c][S_c]\right)}{K_m^s} + \frac{k_c^m\left([T_m][M_m] - [T_c][M_c]\right)}{K_m^m} \right). \tag{C.12}$$

We define

$$\lambda_1 = \frac{k_c^s}{K_m^s}, \qquad \lambda_2 = \frac{k_c^m}{K_m^m}.$$

Factoring out $[T_m]$ and $[T_c]$ gives

$$v_1^f = [T_m]\left([S_m]\lambda_1 + [M_m]\lambda_2\right) - [T_c]\left([S_c]\lambda_1 + [M_c]\lambda_2\right). \tag{C.13}$$

Appendix C.1.2 Final product formation: v_2^f

In the forward direction of the transport cycle, phosphate is released into the matrix as a consequence of the conformational (ping–pong) transition of the phosphate-loaded carrier. Under REA, phosphate binding and unbinding occur rapidly relative to this conformational change, which therefore constitutes the rate limiting step for phosphate transport in the forward direction.

Accordingly, the forward phosphate flux v_2^f can be written as the rate at which the matrix-facing phosphate-loaded transporter (T_mP) is formed:

$$v_2^f = \frac{d[T_mP]}{dt}. \tag{C.14}$$

Substituting the microscopic conformational transition rates gives

$$v_2^f = k_c^p\,[T_cP] - k_{-c}^p\,[T_mP], \tag{C.15}$$

which represents the net forward flux through the rate-limiting conformational transition of the phosphate-loaded carrier. Using the rapid–equilibrium expressions (C.7),

$$v_2^f = \frac{k_c^p[T_c][P_c] - k_{-c}^p[T_m][P_m]}{K_m^p}. \tag{C.16}$$

Under symmetry of the conformational rates,

$$v_2^f = \frac{k_c^p\,([T_c][P_c] - [T_m][P_m])}{K_m^p}. \tag{C.17}$$

Defining

$$\lambda_3 = \frac{k_c^p}{K_m^p},$$

we can write

$$v_2^f = [T_c][P_c]\lambda_3 - [T_m][P_m]\lambda_3. \tag{C.18}$$

Appendix C.1.3 Cycle flux balance and relation between T_m and T_c

In a cyclic ping–pong mechanism, the net flux through the cycle must be constant at steady state [56]. Thus, in the forward cycle, the rate of intermediate production (v_1^f) must equal the rate of final product formation (v_2^f):

$$v_1^f = v_2^f. \tag{C.19}$$

This condition also enforces the 1:1 antiport stoichiometry: each complete transport cycle flips exactly one dicarboxylate (either S or M) in one direction and one phosphate in the opposite direction at steady state.

Equating (C.13) and (C.17), we obtain

$$\Big([T_m]\big([S_m]\lambda_1 + [M_m]\lambda_2\big) - [T_c]\big([S_c]\lambda_1 + [M_c]\lambda_2\big)\Big) = \Big([T_c][P_c]\lambda_3 - [T_m][P_m]\lambda_3\Big). \tag{C.20}$$

Rearranging terms,

$$[T_m]\Big([S_m]\lambda_1 + [M_m]\lambda_2\Big) + [T_m]\Big([P_m]\lambda_3\Big) = [T_c]\Big([P_c]\lambda_3\Big) + [T_c]\Big([S_c]\lambda_1 + [M_c]\lambda_2\Big). \tag{C.21}$$

We can rewrite this as

$$[T_m]\Big(\lambda_1[S_m] + \lambda_2[M_m] + \lambda_3[P_m]\Big) = [T_c]\Big(\lambda_3[P_c] + \lambda_1[S_c] + \lambda_2[M_c]\Big). \tag{C.22}$$

Solving for $[T_c]$ gives

$$[T_c] = [T_m]\,\frac{\lambda_1[S_m] + \lambda_2[M_m] + \lambda_3[P_m]}{\lambda_1[S_c] + \lambda_2[M_c] + \lambda_3[P_c]} = [T_m]\phi, \tag{C.23}$$

where we have defined

$$\phi = \frac{\lambda_1[S_m] + \lambda_2[M_m] + \lambda_3[P_m]}{\lambda_1[S_c] + \lambda_2[M_c] + \lambda_3[P_c]} = \frac{[S_m] + \lambda_{21}[M_m] + \lambda_{31}[P_m]}{[S_c] + \lambda_{21}[M_c] + \lambda_{31}[P_c]}, \tag{C.24}$$

with $\lambda_{21} = \lambda_2/\lambda_1$ and $\lambda_{31} = \lambda_3/\lambda_1$.

Appendix C.2 Reverse Cycle

In the reverse cycle, dicarboxylates move from the external compartment back into the matrix, coupled to the counter-transport of phosphate from the matrix into the external compartment. The same rapid–equilibrium relations for binding (Eqs. (C.2)–(C.7)) apply; only the direction of the net flux is reversed.

Appendix C.2.1 Intermediate product formation: v_1^r

In the reverse direction of the transport cycle, dicarboxylates are delivered into the mitochondrial matrix through the conformational (ping–pong) transition of the substrate-loaded carrier. Under the rapid–equilibrium assumption, binding and unbinding of dicarboxylates occur on a much faster timescale than the conformational change; therefore, the reverse conformational transition constitutes the *rate-limiting step* for dicarboxylate transport into the matrix.

The reverse flux v_1^r can be expressed as the rate of formation of the matrix-facing transporter–substrate complexes:

$$v_1^r = \frac{d[T_mS]}{dt} + \frac{d[T_mM]}{dt}. \tag{C.25}$$

Substituting the microscopic conformational transition rates yields

$$v_1^r = k_{-c}^s\,[T_cS] - k_c^s\,[T_mS] + k_{-c}^m\,[T_cM] - k_c^m\,[T_mM], \tag{C.26}$$

which represents the net reverse flux of succinate and malate delivered to the matrix via the rate limiting conformational transitions of the substrate loaded carrier. Using the rapid equilibrium relations

$$[T_mS] = \frac{[T_m][S_m]}{K_m^s}, \quad [T_cS] = \frac{[T_c][S_c]}{K_m^s}, \tag{C.27}$$

$$[T_mM] = \frac{[T_m][M_m]}{K_m^m}, \quad [T_cM] = \frac{[T_c][M_c]}{K_m^m}, \tag{C.28}$$

we obtain

$$v_1^r = \left(\frac{k_{-c}^s[T_c][S_c] - k_c^s[T_m][S_m]}{K_m^s} + \frac{k_{-c}^m[T_c][M_c] - k_c^m[T_m][M_m]}{K_m^m}\right). \tag{C.29}$$

Under the symmetry assumption for the conformational transitions we write

$$v_1^r = \left(\frac{k_c^s\,([T_c][S_c] - [T_m][S_m])}{K_m^s} + \frac{k_c^m\,([T_c][M_c] - [T_m][M_m])}{K_m^m}\right). \tag{C.30}$$

Introducing the effective transport efficiencies

$$\lambda_1 = \frac{k_c^s}{K_m^s}, \qquad \lambda_2 = \frac{k_c^m}{K_m^m},$$

we can express v_1^r compactly as

$$v_1^r = \Big([T_c]\,([S_c]\lambda_1 + [M_c]\lambda_2) - [T_m]\,([S_m]\lambda_1 + [M_m]\lambda_2)\Big). \tag{C.31}$$

Appendix C.2.2 Final product formation: v_2^r

In the reverse direction of the transport cycle, phosphate is released into the external compartment as a consequence of the conformational (ping–pong) transition of the phosphate-loaded carrier. As in the forward cycle, phosphate binding and dissociation occur much faster than the conformational change; thus, the reversible conformational transition represents the rate limiting step governing phosphate export to the external side.

Accordingly, the reverse phosphate flux v_2^r can be written as the rate of formation of the external-facing phosphate-loaded transporter:

$$v_2^r = \frac{d[T_cP]}{dt}. \tag{C.32}$$

Substituting the microscopic conformational transition rates gives

$$v_2^r = k_{-c}^p\,[T_mP] - k_c^p\,[T_cP], \tag{C.33}$$

which represents the net reverse flux of phosphate delivered to the external compartment via the rate limiting conformational transition of the phosphate-loaded carrier. Using the rapid equilibrium expressions

$$[T_mP] = \frac{[T_m][P_m]}{K_m^p}, \qquad [T_cP] = \frac{[T_c][P_c]}{K_m^p}, \tag{C.34}$$

we obtain

$$v_2^r = \frac{k_{-c}^p[T_m][P_m] - k_c^p[T_c][P_c]}{K_m^p}. \tag{C.35}$$

Under symmetry of the conformational rates this becomes

$$v_2^r = \frac{k_c^p\big([T_m][P_m] - [T_c][P_c]\big)}{K_m^p}. \tag{C.36}$$

Defining

$$\lambda_3 = \frac{k_c^p}{K_m^p},$$

we can write

$$v_2^r = [T_m][P_m]\lambda_3 - [T_c][P_c]\lambda_3. \tag{C.37}$$

Appendix C.2.3 Reverse-cycle flux balance and relation between T_m and T_c

As in the forward cycle, the net flux through the cycle must be constant at steady state [56]. In the reverse direction, this implies that the rate of matrix-facing dicarboxylate production (v_1^r) equals the rate of phosphate production on the external side (v_2^r):

$$v_1^r = v_2^r. \tag{C.38}$$

Equating (C.31) and (C.37) gives

$$\Big([T_c]\,([S_c]\lambda_1 + [M_c]\lambda_2) - [T_m]\,([S_m]\lambda_1 + [M_m]\lambda_2)\Big) = \Big([T_m][P_m]\lambda_3 - [T_c][P_c]\lambda_3\Big). \tag{C.39}$$

Rearranging terms,

$$[T_c]\Big([S_c]\lambda_1 + [M_c]\lambda_2 + [P_c]\lambda_3\Big) = [T_m]\Big([S_m]\lambda_1 + [M_m]\lambda_2 + [P_m]\lambda_3\Big). \tag{C.40}$$

Solving for $[T_c]$ yields

$$[T_c] = [T_m]\,\frac{\lambda_1[S_m] + \lambda_2[M_m] + \lambda_3[P_m]}{\lambda_1[S_c] + \lambda_2[M_c] + \lambda_3[P_c]} = [T_m]\phi, \tag{C.41}$$

where we define

$$\phi = \frac{\lambda_1[S_m] + \lambda_2[M_m] + \lambda_3[P_m]}{\lambda_1[S_c] + \lambda_2[M_c] + \lambda_3[P_c]} = \frac{[S_m] + \lambda_{21}[M_m] + \lambda_{31}[P_m]}{[S_c] + \lambda_{21}[M_c] + \lambda_{31}[P_c]}, \tag{C.42}$$

with $\lambda_{21} = \lambda_2/\lambda_1$ and $\lambda_{31} = \lambda_3/\lambda_1$.

Appendix C.3 Total transporter conservation

The total transporter amount per gram protein $[T_{\text{total}}]$ is distributed among all transporter states. We write

$$\begin{aligned}[T_{\text{total}}] = {} & [T_m] + [T_mS] + [T_mM] + [T_c] + [T_cP] \\ & + [T_cS] + [T_cM] + [T_mP].\end{aligned} \tag{C.43}$$

Using the rapid equilibrium relations (C.2), (C.5), and (C.7), this becomes

$$\begin{aligned}[T_{\text{total}}] = {} & [T_m] + \frac{[T_m][S_m]}{K_m^s} + \frac{[T_m][M_m]}{K_m^m} + [T_c] + \frac{[T_c][P_c]}{K_m^p} \\ & + \frac{[T_c][S_c]}{K_m^s} + \frac{[T_c][M_c]}{K_m^m} + \frac{[T_m][P_m]}{K_m^p}.\end{aligned} \tag{C.44}$$

Equivalently,

$$\begin{aligned}[T_{\text{total}}] = {} & [T_m]\left(1 + \frac{[S_m]}{K_m^s} + \frac{[M_m]}{K_m^m} + \frac{[P_m]}{K_m^p}\right) \\ & + [T_c]\left(1 + \frac{[S_c]}{K_m^s} + \frac{[M_c]}{K_m^m} + \frac{[P_c]}{K_m^p}\right).\end{aligned} \tag{C.45}$$

We define

$$\delta_1 = 1 + \frac{[S_m]}{K_m^s} + \frac{[M_m]}{K_m^m} + \frac{[P_m]}{K_m^p}, \tag{C.46}$$

$$\delta_2 = 1 + \frac{[S_c]}{K_m^s} + \frac{[M_c]}{K_m^m} + \frac{[P_c]}{K_m^p}, \tag{C.47}$$

so that the total transporter conservation can be written as

$$[T_{\text{total}}] = [T_m]\delta_1 + [T_c]\delta_2. \tag{C.48}$$

Substituting (C.23) into (C.48) yields

$$[T_{\text{total}}] = [T_m]\delta_1 + [T_m]\phi\delta_2, \tag{C.49}$$

so that

$$[T_m] = \frac{[T_{\text{total}}]}{\delta_1 + \phi\delta_2}. \tag{C.50}$$

Appendix C.3.1 Final rate expressions for forward cycle

Substituting (C.50) into the forward flux expression (C.13) yields

$$v_1^f = \left(\frac{[T_{\text{total}}]}{\delta_1 + \phi\delta_2} \left([S_m]\lambda_1 + [M_m]\lambda_2\right) - \frac{[T_{\text{total}}]}{\delta_1 + \phi\delta_2} \phi \left([S_c]\lambda_1 + [M_c]\lambda_2\right) \right). \tag{C.51}$$

Equivalently,

$$v_1^f = \left[\frac{\lambda_1 [T_{\text{total}}] \left([S_m] - \phi[S_c]\right)}{(\delta_1 + \phi\delta_2)} + \frac{\lambda_2 [T_{\text{total}}] \left([M_m] - \phi[M_c]\right)}{(\delta_1 + \phi\delta_2)} \right], \tag{C.52}$$

Recalling that $\lambda_1 = \frac{k_c^s}{K_m^s}$ and $\lambda_2 = \frac{k_c^m}{K_m^m}$, and defining $T_{\max}^s = k_c^s [T_{\text{total}}]$ and $T_{\max}^m = k_c^m [T_{\text{total}}]$, we obtain

$$v_1^f = \left[\frac{T_{\max}^s \left([S_m] - \phi[S_c]\right)}{K_m^s(\delta_1 + \phi\delta_2)} + \frac{T_{\max}^m \left([M_m] - \phi[M_c]\right)}{K_m^m(\delta_1 + \phi\delta_2)} \right]. \tag{C.53}$$

Similarly, substituting (C.50) into the phosphate flux expression (C.17) yields

$$\begin{aligned} v_2^f &= \left([T_c][P_c]\lambda_3 - [T_m][P_m]\lambda_3 \right) \\ &= \left(\frac{[T_{\text{total}}]}{\delta_1 + \phi\delta_2} \phi [P_c]\lambda_3 - \frac{[T_{\text{total}}]}{\delta_1 + \phi\delta_2} [P_m]\lambda_3 \right) \\ &= \left(\frac{T_{\max}^p \left(\phi[P_c] - [P_m]\right)}{K_m^p(\delta_1 + \phi\delta_2)} \right), \end{aligned} \tag{C.54}$$

where $T_{\max}^p = k_c^p [T_{\text{total}}]$.

Appendix C.3.2 Final rate expressions for reverse cycle

Substituting (C.50) into the reverse flux expression (C.31) yields

$$\begin{aligned} v_1^r &= \left(\frac{[T_{\text{total}}]}{\delta_1 + \phi\delta_2} \phi \left([S_c]\lambda_1 + [M_c]\lambda_2\right) - \frac{[T_{\text{total}}]}{\delta_1 + \phi\delta_2} \left([S_m]\lambda_1 + [M_m]\lambda_2\right) \right) \\ &= \left[\frac{\lambda_1 [T_{\text{total}}] \left(\phi[S_c] - [S_m]\right)}{(\delta_1 + \phi\delta_2)} + \frac{\lambda_2 [T_{\text{total}}] \left(\phi[M_c] - [M_m]\right)}{(\delta_1 + \phi\delta_2)} \right], \end{aligned} \tag{C.55}$$

Recalling that $\lambda_1 = \frac{k_c^s}{K_m^s}$ and $\lambda_2 = \frac{k_c^m}{K_m^m}$, and defining $T_{\max}^s = k_c^s [T_{\text{total}}]$ and $T_{\max}^m = k_c^m [T_{\text{total}}]$, we obtain

$$v_1^r = \left[\frac{T_{\max}^s \left(\phi[S_c] - [S_m]\right)}{K_m^s(\delta_1 + \phi\delta_2)} + \frac{T_{\max}^m \left(\phi[M_c] - [M_m]\right)}{K_m^m(\delta_1 + \phi\delta_2)} \right]. \tag{C.56}$$

Similarly, substituting $[T_m]$ and $[T_c] = [T_m]\phi$ into (C.37), we obtain

$$\begin{aligned} v_2^r &= \left([T_m][P_m]\lambda_3 - [T_c][P_c]\lambda_3 \right) \\ &= \left(\frac{[T_{\text{total}}]}{\delta_1 + \phi\delta_2} [P_m]\lambda_3 - \frac{[T_{\text{total}}]}{\delta_1 + \phi\delta_2} \phi [P_c]\lambda_3 \right) \\ &= \left(\frac{\lambda_3 [T_{\text{total}}] \left([P_m] - \phi[P_c]\right)}{(\delta_1 + \phi\delta_2)} \right). \end{aligned} \tag{C.57}$$

Defining $T^p_{\max} = k^p_c[T_{\text{total}}]$, we obtain

$$v^r_2 = \frac{T^p_{\max}\left([P_m] - \phi[P_c]\right)}{K^p_m(\delta_1 + \phi\delta_2)}. \tag{C.58}$$

Appendix C.4 Net Flux of the Complete Cycle

The complete transport cycle is reversible and can proceed in both the forward and reverse directions. Under REA, the forward-cycle fluxes of dicarboxylates and phosphate are

$$v^f_1 = \left[\frac{T^s_{\max}\left([S_m] - \phi[S_c]\right)}{K^s_m(\delta_1 + \phi\delta_2)} + \frac{T^m_{\max}\left([M_m] - \phi[M_c]\right)}{K^m_m(\delta_1 + \phi\delta_2)}\right], \tag{C.59}$$

$$v^f_2 = \frac{T^p_{\max}\left(\phi[P_c] - [P_m]\right)}{K^p_m(\delta_1 + \phi\delta_2)}, \tag{C.60}$$

where

$$T^s_{\max} = k^s_c[T_{\text{total}}], \qquad T^m_{\max} = k^m_c[T_{\text{total}}], \qquad T^p_{\max} = k^p_c[T_{\text{total}}],$$

and

$$\delta_1 = 1 + \frac{[S_m]}{K^s_m} + \frac{[M_m]}{K^m_m} + \frac{[P_m]}{K^p_m}, \tag{C.61}$$

$$\delta_2 = 1 + \frac{[S_c]}{K^s_m} + \frac{[M_c]}{K^m_m} + \frac{[P_c]}{K^p_m}. \tag{C.62}$$

The corresponding reverse-cycle fluxes are

$$v^r_1 = \left[\frac{T^s_{\max}\left(\phi[S_c] - [S_m]\right)}{K^s_m(\delta_1 + \phi\delta_2)} + \frac{T^m_{\max}\left(\phi[M_c] - [M_m]\right)}{K^m_m(\delta_1 + \phi\delta_2)}\right], \tag{C.63}$$

$$v^r_2 = \frac{T^p_{\max}\left([P_m] - \phi[P_c]\right)}{K^p_m(\delta_1 + \phi\delta_2)}, \tag{C.64}$$

with

$$\phi = \left(\frac{[S_m] + \lambda_{21}[M_m] + \lambda_{31}[P_m]}{[S_c] + \lambda_{21}[M_c] + \lambda_{31}[P_c]}\right) \tag{C.65}$$

Appendix C.4.1 Net dicarboxylate flux

We define the net dicarboxylate exchange rate as the difference between the reverse and forward contributions,

$$V^{\text{net}}_1 = v^r_1 - v^f_1. \tag{C.66}$$

Substituting the expressions above for v^r_1 and v^f_1 yields

$$\begin{aligned} V^{\text{net}}_1 = &\left[\frac{T^s_{\max}\left(\phi[S_c] - [S_m]\right)}{K^s_m(\delta_1 + \phi\delta_2)} + \frac{T^m_{\max}\left(\phi[M_c] - [M_m]\right)}{K^m_m(\delta_1 + \phi\delta_2)}\right] \\ &- \left[\frac{T^s_{\max}\left([S_m] - \phi[S_c]\right)}{K^s_m(\delta_1 + \phi\delta_2)} + \frac{T^m_{\max}\left([M_m] - \phi[M_c]\right)}{K^m_m(\delta_1 + \phi\delta_2)}\right]. \end{aligned} \tag{C.67}$$

We decompose this into separate contributions from succinate and malate,

$$V_1^{\text{net}} = J_{\text{succ}} + J_{\text{mal}}, \tag{C.68}$$

where

$$J_{\text{succ}} = \left[\frac{T^s_{\max}\left(\phi[S_c] - [S_m]\right)}{K^s_m(\delta_1 + \phi\delta_2)}\right] - \left[\frac{T^s_{\max}\left([S_m] - \phi[S_c]\right)}{K^s_m(\delta_1 + \phi\delta_2)}\right], \tag{C.69}$$

$$J_{\text{mal}} = \left[\frac{T^m_{\max}\left(\phi[M_c] - [M_m]\right)}{K^m_m(\delta_1 + \phi\delta_2)}\right] - \left[\frac{T^m_{\max}\left([M_m] - \phi[M_c]\right)}{K^m_m(\delta_1 + \phi\delta_2)}\right]. \tag{C.70}$$

Appendix C.4.2 Net phosphate flux

Analogously, the net phosphate exchange rate is defined as

$$V_2^{net} = v_2^r - v_2^f, \tag{C.71}$$

so that

$$V_2^{net} = \left[\frac{T^p_{\max}\left([P_m] - \phi[P_c]\right)}{K^p_m(\delta_1 + \phi\delta_2)}\right] - \left[\frac{T^p_{\max}\left(\phi[P_c] - [P_m]\right)}{K^p_m(\delta_1 + \phi\delta_2)}\right]. \tag{C.72}$$

We denote the corresponding net phosphate flux by

$$J_{\text{pho}} = \left[\frac{T^p_{\max}\left([P_m] - \phi[P_c]\right)}{K^p_m(\delta_1 + \phi\delta_2)}\right] - \left[\frac{T^p_{\max}\left(\phi[P_c] - [P_m]\right)}{K^p_m(\delta_1 + \phi\delta_2)}\right]. \tag{C.73}$$

These expressions provide the net dicarboxylate and phosphate fluxes for the complete reversible ping–pong cycle under the rapid–equilibrium assumption with a symmetric carrier and competitive binding of malate and succinate at a single site.

Appendix D Simulating the Effect of Succinate dehydrogenase (SDH) on the Dynamics of the SLC25A10 Transporter

Succinate dehydrogenase (SDH) is an enzyme involved in both the tricarboxylic acid (TCA) cycle and the electron transport chain (ETC). It takes part in tranportation of electrons by catalyzing the oxidation of succinate into fumarate (F) while reducing ubiquinone (Q) to ubiquinol (QH_2). This reaction results in the depletion of the mitochondrial succinate pool, affecting the fluxes and dynamics of the SLC25A10 transporter due to its role in exchanging succinate with phosphate. The electron transfer reactions catalyzed by SDH or Complex II are:

$$\mathrm{S}_m + \mathrm{FAD}_m \rightleftharpoons \mathrm{F}_m + \mathrm{FADH}_{2,m} \tag{D.1}$$

$$\mathrm{FADH}_{2,m} + \mathrm{Q}_m \rightleftharpoons \mathrm{FAD}_m + \mathrm{QH}_{2,m} \tag{D.2}$$

These reactions can be lumped into a single reaction:

$$\mathrm{S}_m + \mathrm{Q}_m \rightleftharpoons \mathrm{F}_m + \mathrm{QH}_{2,m} \tag{D.3}$$

where S_m denotes mitochondrial succinate, Q_m denotes ubiquinone, F_m denotes mitochondrial fumarate and $QH_{2,m}$ denotes mitochondrial ubiquinol.

The overall reaction flux, J_{SDH}, is adopted from Shima Sadri et al. (2023), who modeled using a reversible bi-bi kinetic equation, the flux equation is as follow:

$$J_{\text{SDH}} = \frac{V_{\max}^{sdh}\left(\frac{[\text{S}_m][\text{Q}_m]}{k_m^{s,\text{eff}}k_m^q} - \frac{[\text{F}_m][\text{QH}_m]}{k_m^f k_m^{qh} K_{\text{eq}}^{sdh}}\right)}{\left(1+\frac{[S_m]}{k_m^{s,\text{eff}}}+\frac{[F_m]}{k_m^f}\right)\left(1+\frac{[Q_m]}{k_m^q}+\frac{[QH_m]}{k_m^{qh}}\right)} \tag{D.4}$$

where $k_m^{s,\text{eff}}$ is the effective succinate binding constant and calculated as follow:

$$k_m^{s,\text{eff}} = k_m^{s,sdh}\left(\frac{k_m^o + [O_m]}{k_m^o}\right)\left(\frac{k_m^{m,sdh}}{k_m^{m,sdh} + [M_m]}\right) \tag{D.5}$$

this modification to the succinate binding constant ($k_m^{s,sdh}$) reveals that SDH is inhibited by oxaloacetate (O_m) accumulation and stimulated by malate (M_m) accumulation in the mitochondrial matrix. The equilibrium constant (K_{eq}^{sdh}) is derived from the Gibbs free energy:

$$K_{\text{eq}} = e^{-\Delta G'^0_{sdh}/RT} \tag{D.6}$$

where is $\Delta G'^0_{sdh}$ is gibbs free energy for SDH enzyme. The kinetic parameters for the SDH model are given in Table 10.

Table 10: SDH Model Kinetic Parameters

Parameter	Definition	Value	Units	Ref.
$V_{\max}^{sdh}$	Maximum forward reaction rate	100	$\mu mol/min/g$	Assumed
$k_m^{s,sdh}$	Succinate binding constant	1.80×10^{-3}	M	[17]
k_m^q	Ubiquinone binding constant	140×10^{-6}	M	[17]
k_m^f	Fumarate binding constant	1.80×10^{-3}	M	[17]
k_m^{qh}	Ubiquinol binding constant	2.45×10^{-6}	M	[17]
k_m^o	Oxaloacetate binding constant	0.0315×10^{-6}	M	[17]
k_m^m	Malate binding constant	11.7×10^{-6}	M	[17]
$\Delta G'^0_{sdh}$	Gibbs free energy of the reaction (pH=7)	-2.41	KJ/mol	[17]

The fixed mitochondrial concentrations of metabolites involved in the SDH reaction are given in Table 11.

Table 11: Fixed Mitochondrial Concentrations for SDH Model

Metabolite	Concentration	Unit	Source
F_m	10	mM	[17]
O_m	10	mM	[17]
Q_m	3.75×10^{-1}	mM	[17]
QH_{2m}	1.12	mM	[17]

We incorporate the flux of this reaction (J_{sdh}) as an external source into reduced SLC25A10 model with a negative sign, representing the catalytic efficiency of SDH. A high activity level implies rapid depletion of mitochondrial succinate due to its conversion to

fumarate. Conversely, low activity indicates succinate accumulation within mitochondria, whereas moderate activity corresponds to balanced succinate metabolism. The modified reduced system of ordinary differential equations (ODEs) thus becomes:

$$\frac{d[M_m]}{dt} = \frac{1}{\tilde{V}_m} J_{\text{mal}}, \tag{D.7}$$

$$\frac{d[M_c]}{dt} = -\frac{1}{\tilde{V}_c} J_{\text{mal}}, \tag{D.8}$$

$$\frac{d[S_m]}{dt} = \frac{1}{\tilde{V}_m} \left(J_{\text{succ}} - J_{\text{SDH}}\right), \tag{D.9}$$

$$\frac{d[S_c]}{dt} = -\frac{1}{\tilde{V}_c} J_{\text{succ}}, \tag{D.10}$$

$$\frac{d[P_m]}{dt} = -\frac{1}{\tilde{V}_m} \left(J_{\text{pho}}\right), \tag{D.11}$$

$$\frac{d[P_c]}{dt} = \frac{1}{\tilde{V}_c} J_{\text{pho}}, \tag{D.12}$$

Appendix E Simulating the Effect of Succinyl-CoA synthetase (SCoAS) on the Dynamics of the SLC25A10 Transporter

Succinyl–CoA synthetase (SCoAS), also known as succinyl–CoA ligase, is another enzyme which is involved in TCA cycle. This enzyme catalysis the reversable reaction of conversion of succinyl-coA to succinate. The free energy released from this reaction drives the substrate-level phosphorylation of guanosine diphosphate (GDP) to guanosine triphosphate (GTP), using inorganic mitochondrial phosphate (P_m). This reaction result into depletion of mitochondrial phosphate pool and increasing the mitochondrial succinate pool by conversion of succinyl-coA to succinate. Therefore it affects the fluxes and dynamic of SLC25A10 transporter. The chemical reactions are:

$$\mathrm{SCoA_m} + \mathrm{GDP_m} + \mathrm{P_m} \rightleftharpoons \mathrm{S_m} + \mathrm{GTP_m} + \mathrm{CoA_m} + \mathrm{H_m^+}$$

We adopt overall flux model of this transporter from sadri et al. (2023). The overall reaction flux, J_{SCAS}, is given by:

$$J_{\text{SCAS}} = \frac{V_{\max}^{scas}\left(\frac{[\mathrm{SCoA}_m][\mathrm{GDP}_m][\mathrm{P}_m]}{K_m^{scoa}K_m^{gdp}K_m^{p,scas}} - \frac{[\mathrm{S}_m][\mathrm{GTP}_m][\mathrm{CoA}_m]}{K_m^{s,scas}K_m^{gtp}K_m^{coa}K'_{\text{eq,scas}}}\right)}{\left(1 + \frac{[\mathrm{SCoA}_m]}{K_m^{scoa}} + \frac{[\mathrm{S}_m]}{K_m^{s,scas}} + \frac{[\mathrm{CoA}_m]}{K_m^{coa}} + \frac{[\mathrm{S}_m][\mathrm{CoA}_m]}{K_m^{s,scas}K_m^{coa}}\right)\left(1 + \frac{[\mathrm{GDP}_m]}{K_m^{gdp}} + \frac{[\mathrm{P}_m]}{K_m^{p,scas}} + \frac{[\mathrm{GTP}_m]}{K_m^{gtp}} + \frac{[\mathrm{GDP}_m][\mathrm{P}_m]}{K_m^{p,scas}K_m^{gdp}}\right)} \tag{E.1}$$

where equilibrium constant ($K'_{\text{eq,scas}}$) for this reaction is:

$$K'_{\text{eq,SCAS}} = \exp\left(\frac{-\Delta G'^{0}_{\text{SCAS}}}{RT}\right) \times 10^{\mathrm{pH}_m - 7} \tag{E.2}$$

this equation incorporate the effect of pH because of generation of one proton.

The kinetic parameters for the SCAS model are given in Table 12.

Table 12: SCAS Model Kinetic Parameters

Parameter	Definition	Value	Unit	Reference
$V_{\max}^{scas}$	Maximum forward reaction rate	100	$\mu mol \times min^{-1} \times g^{-1}$	Assumed
K_m^{scoa}	SCoA binding constant	12.5×10^{-6}	M	[17]
K_m^{gdp}	GDP binding constant	5.70×10^{-6}	M	[17]
$K_m^{p,scas}$	Pi binding constant	2.10×10^{-3}	M	[17]
$K_m^{s,scas}$	SUC binding constant	451×10^{-6}	M	[17]
K_m^{gtp}	GTP binding constant	23.1×10^{-6}	M	[17]
K_m^{coa}	CoA binding constant	17.7×10^{-6}	M	[17]
$\Delta G'^{0}_{\text{SCAS}}$	Gibbs free energy of the reaction (pH=7)	1.26	$KJ \times mol^{-1}$	[17]

The fixed mitochondrial concentrations of metabolites involved in the SCAS reaction are given in Table 13.

Table 13: Fixed Mitochondrial Concentrations for SCAS Model

Metabolite	Concentration	Unit	Source
SCoA_m	10×10^{-3}	M	[17]
GDP_m	2.5×10^{-5}	M	[17]
GTP_m	9.75×10^{-4}	M	[17]
CoA_m	10×10^{-3}	M	[17]

We incorporate the SCAS flux J_{SCAS} as an enzymatic source of matrix succinate and a sink of matrix inorganic phosphate, reflecting the net stoichiometry of succinyl–CoA conversion coupled to substrate-level phosphorylation. High SCAS activity therefore tends to increase $[S_m]$ while depleting $[P_m]$, strengthening the metabolic drive for succinate handling but simultaneously tightening the phosphate constraint on SLC25A10 antiport cycling. Conversely, low SCAS activity reduces succinate production and relaxes phosphate demand. Under this coupling, the modified reduced ODE system becomes

$$\frac{d[M_m]}{dt} = \frac{1}{\tilde{V}_m} J_{\text{mal}}, \tag{E.3}$$

$$\frac{d[M_c]}{dt} = -\frac{1}{\tilde{V}_c} J_{\text{mal}}, \tag{E.4}$$

$$\frac{d[S_m]}{dt} = \frac{1}{\tilde{V}_m} \left(J_{\text{succ}} - J_{\text{SDH}} + J_{\text{SCAS}}\right), \tag{E.5}$$

$$\frac{d[S_c]}{dt} = -\frac{1}{\tilde{V}_c} J_{\text{succ}}, \tag{E.6}$$

$$\frac{d[P_m]}{dt} = -\frac{1}{\tilde{V}_m} \left(J_{\text{pho}} + J_{\text{SCAS}}\right), \tag{E.7}$$

$$\frac{d[P_c]}{dt} = \frac{1}{\tilde{V}_c} J_{\text{pho}}, \tag{E.8}$$

Appendix F Description of the experimental work

To elucidate the metabolic consequences of diminished SLC25A10 activity, we conducted a comparative metabolomic analysis. We utilized immortalized murine chromaffin cells (imCCs) wherein an inducible knockdown of Slc25a10 (SLC25A10-KD) was established, alongside corresponding scramble imCCs serving as controls. Subsequent to verification of the efficacy of SLC25A10 knockdown, extracts of cellular metabolites of both SLC25A10-KD and scramble imCC are subjected to a comprehensive metabolomic profiling based on liquid chromatography-mass spectrometry (LC-MS).

The metabolomic data revealed significant alterations in the cellular metabolic landscape attributable to SLC25A10 deficiency. In a targeted analysis (Fig. 17b), several dicarboxylates—including succinate, fumarate, and malonate—showed increased abundance in SLC25A10-KD cells relative to controls. This finding directly aligns with the known function of SLC25A10 as a mitochondrial dicarboxylate transporter, indicating that its reduced expression impairs the mitochondrial efflux or exchange of these metabolites.

Furthermore, a broader, untargeted view of the metabolome (Fig. 17a) underscored the extensive impact of SLC25A10 knockdown. This analysis highlighted a global metabolic reprogramming, with numerous metabolites exhibiting statistically significant changes in abundance. Among those notably elevated in SLC25A10-KD cells were L-lactic acid, 3-hydroxy-L-proline, urocanic acid, and D-pantothenic acid, in addition to fumaric acid. These widespread metabolic shifts suggest that SLC25A10 plays an integral role in maintaining broader cellular metabolic homeostasis, likely through its influence on the tricarboxylic acid (TCA) cycle and interconnected pathways.

We emphasize that these measurements reflect whole-cell metabolite pools and therefore conflate contributions from multiple subcellular compartments. Accordingly, we use the metabolomics results as qualitative context for the transporter modelling rather than as direct, compartment-resolved validation of transport directionality or thermodynamic driving forces.

Appendix F.1 Method description

Cell Lines and Culture Conditions: Immortalized murine chromaffin cells (imCCs) [57] were utilized for all experiments. Cells were maintained in Dulbecco's Modified Eagle Medium (DMEM) high glucose (Gibco, Cat# 11965), supplemented with 10% (v/v) fetal bovine serum (FBS; Sigma, Cat# 7524). Cultures were maintained at 37 °C in a humidified atmosphere containing 5% CO_2. Cells were routinely passaged at 70–80% confluency using TrypLE and seeded for experiments.

Generation of Inducible Slc25a10 Knockdown imCCs: To generate imCCs with inducible knockdown of Slc25a10, a Tet-On 3G doxycycline-inducible shRNA lentiviral system (VectorBuilder) was used. This system involves sequential stable expression of the Tet regulatory protein and a Tet-On inducible knockdown sequence. Doxycycline (5 µg/mL) was added to the cells for 48 hours to induce knockdown, after which knockdown efficacy

was confirmed via western blotting. Cells were then plated onto 6-well plates, and doxycycline was added the day after plating to induce knockdown. After 48 hours, metabolites were harvested from scramble and knockdown cells for downstream LC-MS analysis.

LC-MS Sample Preparation: Cells were washed with ice-cold saline and scraped into pre-cooled acetonitrile/methanol/water (40:40:20) containing 0.5% formic acid and 1 µg/mL D_6-glutaric acid (internal standard), and immediately placed on ice. After 5 minutes, 8.8 µL of 15% NH_4HCO_3 per 100 µL of sample was added and mixed. Samples were immediately snap-frozen on dry ice for 15 minutes, then centrifuged at 14,800 g for 5 minutes at 4 °C. Supernatants were collected and stored at −80 °C until LC-MS analysis.

LC-MS Analysis: Samples were analysed using an Agilent Infinity II HPLC coupled with an Agilent G6545A qTOF mass spectrometer. Metabolites were separated on a Waters Premier BEH Z-HILIC column (1.7 µm, 2.1 × 150 mm). Mobile phase A consisted of 20 mM ammonium bicarbonate with 0.1% ammonium hydroxide and 0.1% InfinityLab deactivator. Mobile phase B consisted of H_2O:ACN (1:9 ratio) with 0.1% InfinityLab deactivator. The flow rate was 0.2 mL/min with the following gradient: 10% A held for 2 min, ramped to 35% A at 18 min, 70% A at 22 min, 90% A at 22.1 min (held for 2.9 min), followed by 10% A at 25.1 min and held for 5 min. Data processing was performed using Agilent Profinder 10. Normalisation to the internal standard and total protein content was performed using an in-house script.

Appendix G Analytical Equilibrium Concentrations for SLC25A10 Transporter

To derive analytical equilibrium expressions for the concentrations of mitochondrial succinate ($[S_m^{eq}]$), phosphate ($[P_m^{eq}]$), and malate ($[M_m^{eq}]$), as well as external succinate ($[S_c^{eq}]$), phosphate ($[P_c^{eq}]$), and malate ($[M_c^{eq}]$), as functions of the initial mitochondrial concentrations ($[S_m^0]$, $[P_m^0]$, $[M_m^0]$) and external concentrations ($[S_c^0]$, $[P_c^0]$, $[M_c^0]$), we employ conservation laws and Gibbs free energy minimization.

Here we derive closed-form expressions for the equilibrium concentrations of succinate and phosphate across the mitochondrial inner membrane mediated by the electroneutral antiporter SLC25A10. The derivation explicitly accounts for unequal compartment volumes and is based on mass conservation and thermodynamic equilibrium.

The analytical derivation relies on the following assumptions: The system consists of a well-mixed mitochondrial matrix and external side, each characterized by fixed volumes V_m and V_c, respectively, Transport occurs via a one-to-one electroneutral antiport mechanism:

$$\mathrm{S}_m + \mathrm{P}_\mathrm{c} \rightleftharpoons \mathrm{S}_\mathrm{c} + \mathrm{P}_m.$$

The system is considered at equilibrium, such that the Gibbs free energy change of the transport reaction is zero. Only succinate and phosphate participate in the exchange reaction; malate concentration is assumed to be zero in this derivation. Volume changes due to osmotic effects are neglected. Total amounts of succinate and phosphate are

conserved across compartments:

$$V_m[S_m^{\mathrm{eq}}] + V_{\mathrm{c}}[S_{\mathrm{c}}^{\mathrm{eq}}] = V_m[S_m^0] + V_{\mathrm{c}}[S_{\mathrm{c}}^0], \tag{G.1}$$

$$V_m[P_m^{\mathrm{eq}}] + V_{\mathrm{c}}[P_{\mathrm{c}}^{\mathrm{eq}}] = V_m[P_m^0] + V_{\mathrm{c}}[P_{\mathrm{c}}^0]. \tag{G.2}$$

To enforce the strict 1:1 electroneutral antiport stoichiometry of SLC25A10, the transport process is parameterized by a single reaction extent ξ, which represents the net progress of the exchange cycle. Each transport event transfers exactly one succinate molecule in one direction and one phosphate molecule in the opposite direction, implying that changes in their concentrations are equal in magnitude and opposite in sign. Accordingly, the equilibrium concentrations in each compartment can be expressed as linear functions of the same exchange parameter, for example

$$[S_{\mathrm{c}}^{\mathrm{eq}}] = [S_{\mathrm{c}}^0] + \xi \tag{G.3}$$

$$[P_{\mathrm{c}}^{\mathrm{eq}}] = [P_{\mathrm{c}}^0] - \xi. \tag{G.4}$$

This formulation ensures mass conservation and electroneutrality by construction, while compartment volumes are incorporated separately when converting exchanged amounts to concentrations.

Substituting into Eqs. (G.1)–(G.2) yields:

$$[S_m^{\mathrm{eq}}] = [S_m^0] - \frac{V_{\mathrm{c}}}{V_m}\,\xi, \tag{G.5}$$

$$[P_m^{\mathrm{eq}}] = [P_m^0] + \frac{V_{\mathrm{c}}}{V_m}\,\xi. \tag{G.6}$$

For an electroneutral exchange reaction, the Gibbs free energy change is:

$$\Delta G = RT \ln\left(\frac{[S_{\mathrm{c}}^{\mathrm{eq}}][P_m^{\mathrm{eq}}]}{[S_m^{\mathrm{eq}}]P_{\mathrm{c}}^{\mathrm{eq}}}\right). \tag{G.7}$$

At equilibrium, $\Delta G = 0$, which implies:

$$[S_{\mathrm{c}}^{\mathrm{eq}}][P_m^{\mathrm{eq}}] = [S_m^{\mathrm{eq}}]P_{\mathrm{c}}^{\mathrm{eq}}. \tag{G.8}$$

Substituting the expressions above into Eq. (G.8) and simplifying yields a linear equation for ξ, whose solution is:

$$\xi = \frac{V_m\big([S_m^0][P_{\mathrm{c}}^0] - [S_{\mathrm{c}}^0][P_m^0]\big)}{V_m([S_m^0] + [P_m^0]) + V_{\mathrm{c}}([S_{\mathrm{c}}^0] + [P_{\mathrm{c}}^0])}. \tag{G.9}$$

Substituting Eq. (G.9) into the expressions for the equilibrium concentrations yields:

$$[S_c^{eq}] = [S_c^0] + \frac{[P_c^0][S_m^0] - [P_m^0][S_c^0]}{[P_m^0] + [S_m^0] + \frac{V_c}{V_m}([P_c^0] + [S_c^0])}, \tag{G.10}$$

$$S_m^{eq} = [S_m^0] - \frac{\frac{V_c}{V_m}([P_c^0][S_m^0] - [P_m^0][S_c^0])}{[P_m^0] + [S_m^0] + \frac{V_c}{V_m}([P_c^0] + [S_c^0])}, \tag{G.11}$$

$$P_c^{eq} = [P_c^0] - \frac{[P_c^0][S_m^0] - [P_m^0][S_c^0]}{[P_m^0] + [S_m^0] + \frac{V_c}{V_m}([P_c^0] + [S_c^0])}, \tag{G.12}$$

$$P_m^{eq} = [P_m^0] + \frac{\frac{V_c}{V_m}([P_c^0][S_m^0] - [P_m^0][S_c^0])}{[P_m^0] + [S_m^0] + \frac{V_c}{V_m}([P_c^0] + [S_c^0])}. \tag{G.13}$$

These expressions reduce to the classical concentration-only formulas in the special case $V_m = V_c$. An analogous derivation can be carried out for malate–phosphate exchange by assuming zero succinate concentration.

Appendix H Determination of Proteoliposome Compartment Volumes

This appendix describes how the internal and external compartment volumes were parameterized for the proteoliposome assays. All primary quantities were taken directly from Indiveri et al. [23] (Table 14). The only non-tabulated value extracted from a figure is the intraliposomal (internal) volume at the optimized condition (13 Amberlite passages), which was read from Fig. 2 of Indiveri et al. [23] and treated as an approximate value.

Table 14: Primary quantities taken from Indiveri et al. [23] and used as inputs to the volume calculations.

Symbol	Quantity (as reported)	Value used here
V_{mix}	Total reconstitution mixture volume	0.68 mL = 680 μL
V_{assay}	Aliquot (reaction) volume used per transport assay	100 μL
m_{PL}	Total phospholipid mass in the reconstitution mixture	6.7 mg
m_{prot}	Total protein mass in the reconstitution mixture	7–15 μg
$V_{\text{in}}^{\text{approx}}$	Intraliposomal volume at 13 Amberlite passages	$\approx$ 4.0 μL/mg PL

The external (extraliposomal) compartment volume in the transport assay is defined as the total assay volume V_{assay} minus the total internal volume V_m. Therefore, the total external volume V_c is

$$V_c = V_{\text{assay}} - V_m, \tag{H.1}$$

where $V_{\text{assay}} = 100$ μL. To express the external volume in the same normalized units as the internal compartment (volume per mass of reconstituted carrier protein), we first compute the protein mass per assay from the mixture composition. The protein mass was

reported as a range (7–15 μg) in the full reconstitution mixture volume ($V_{\text{mix}} = 680\ \mu$L). We therefore define the average protein mass in the mixture as

$$m_{\text{prot,avg}} = \frac{7+15}{2}\ \mu\text{g} = 11\ \mu\text{g}. \tag{H.2}$$

Because each assay used a 100 μL aliquot of the 680 μL mixture, the protein mass per assay is

$$m_{\text{prot,assay}} = m_{\text{prot,avg}} \left(\frac{V_{\text{assay}}}{V_{\text{mix}}}\right) = 11\ \mu\text{g} \left(\frac{100}{680}\right) = 1.618\ \mu\text{g} = 1.618 \times 10^{-6}\ \text{g}. \tag{H.3}$$

The total internal (intraliposomal) aqueous volume present in the full reconstitution mixture is obtained by multiplying the intraliposomal volume per lipid mass (read from Fig. 2 of Indiveri et al. [23] at the optimized condition) by the total lipid mass used in the mixture:

$$V_{\text{m,mix}} = V_{\text{in}}^{\text{approx}}\, m_{\text{PL}} = \left(4.0\ \frac{\mu\text{L}}{\text{mg PL}}\right)(6.7\ \text{mg PL}) = 26.8\ \mu\text{L}. \tag{H.4}$$

The specific internal volume, expressed as internal volume per gram of reconstituted protein, is then

$$\tilde{V}_m = \frac{V_{\text{m,mix}}}{m_{\text{prot,avg}}}. \tag{H.5}$$

Using $V_{\text{m,mix}} = 26.8\ \mu$L and $m_{\text{prot,avg}} = 11\ \mu$g yields

$$\tilde{V}_m = \frac{26.8\ \mu\text{L}}{11\ \mu\text{g}} = 2.436\ \frac{\mu\text{L}}{\mu\text{g}} = 2.436\ \text{L}\,\text{g}^{-1}. \tag{H.6}$$

The total internal volume corresponding to a single 100 μL assay aliquot is

$$V_m = \tilde{V}_m\, m_{\text{prot,assay}} = \left(2.436\ \text{L}\,\text{g}^{-1}\right)\left(1.618 \times 10^{-6}\ \text{g}\right) = 3.94 \times 10^{-6}\ \text{L} = 3.94\ \mu\text{L}. \tag{H.7}$$

From (H.1), the total external volume is

$$V_c = 100\ \mu\text{L} - 3.94\ \mu\text{L} = 96.06\ \mu\text{L}. \tag{H.8}$$

Finally, the specific external volume is defined by normalizing the external volume by the protein mass present in the same assay aliquot:

$$\tilde{V}_c = \frac{V_c}{m_{\text{prot,assay}}} = \frac{96.06 \times 10^{-6}\ \text{L}}{1.618 \times 10^{-6}\ \text{g}} = 59.4\ \text{L}\,\text{g}^{-1}. \tag{H.9}$$

Together, these definitions provide consistent internal and external compartment volumes in both absolute units (μL per assay) and normalized units (L g^{-1} protein).

Appendix I Determination of Compartment Volumes in Intact Rat Liver Mitochondria Assays

The uptake assays using intact rat liver mitochondria in Palmieri et al. [3] follow an inhibitor-stop and rapid-centrifugation protocol. In these experiments, intramitochondrial concentrations are obtained by converting the measured intrapellet radioactivity

into an amount (e.g., nmol) and dividing by the aqueous volume that is inaccessible to extracellular sucrose (the sucrose-inaccessible space). In parallel measurements, ^3H_2O and [^{14}C]sucrose are used to estimate total pellet water and the sucrose-permeable space, respectively, which together determine the intramitochondrial aqueous space relevant for solute accumulation. Because Palmieri et al. [3] do not report a single numerical value for the sucrose-inaccessible space across all experiments, we adopt a literature value for rat liver mitochondria under comparable conditions for the specific internal volume [39].

Table 15: Primary quantities taken from Palmieri et al. [3] and Harris et al. [39] and used as inputs to the compartment-volume calculations for intact rat liver mitochondria uptake assays.

Symbol	Quantity (as reported)	Value used here
m_p	Mitochondrial protein per assay (range)	1.55–2.50 mg
$\tilde{V}_m$	Sucrose-inaccessible water space (mean)	0.70 mL g^{-1}
V_c	External incubation volume	Not stated (assume 1.0 mL)

The specific internal volume is defined as the sucrose-inaccessible aqueous space per unit mitochondrial protein. In our model notation, this corresponds to the matrix volume per protein, $\tilde{V}_m$. The total internal volume is the internal aqueous volume present in a single assay and equals the specific internal volume multiplied by the protein mass used in that assay; this corresponds to the matrix volume V_m in our model. The total external volume is the incubation-medium volume in which mitochondria are suspended; this corresponds to the external compartment volume V_c in our model. The specific external volume is the external volume normalized per unit mitochondrial protein; this corresponds to $\tilde{V}_c$ in our model.

Table 15 summarizes the quantities reported in Palmieri et al. [3] and the literature value used for the sucrose-inaccessible aqueous space [39]. The incubation (external) reaction volume was not explicitly specified; therefore, we assume an incubation volume of 1.0 mL. In our model notation, this incubation medium corresponds to the external compartment volume V_c.

A literature mean value for the sucrose-inaccessible water space of rat liver mitochondria was used:

$$\tilde{V}_m = 0.70 \text{ mL g}^{-1} = 0.70 \ \mu\text{L mg}^{-1} = 7.0 \times 10^{-4} \text{ L g}^{-1}. \tag{I.1}$$

For an assay containing mitochondrial protein mass m_p (in mg), the total internal aqueous volume is

$$V_m = \tilde{V}_m \, m_p. \tag{I.2}$$

Since the m_p range is given, we used mean protein mass $\bar{m}_p = 2.03$ mg and (I.1),

$$V_m = (0.70 \ \mu\text{L mg}^{-1})(2.03 \text{ mg}) = 1.42 \ \mu\text{L}. \tag{I.3}$$

The specific external volume is the incubation volume normalized by mitochondrial protein mass:

$$\tilde{V}_c = \frac{V_c}{\bar{m}_p} = \frac{10^{-3} \text{ L}}{2.03 \times 10^{-3} \text{ g}} = 0.49 \text{ L g}^{-1}. \tag{I.4}$$

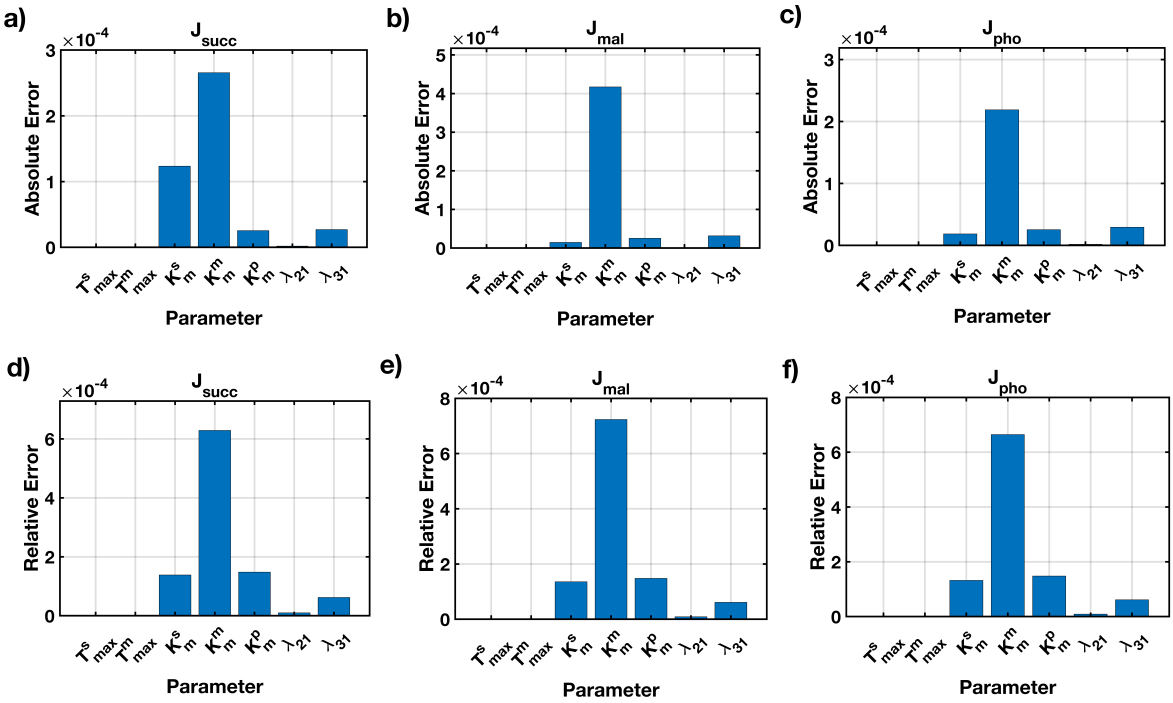

Figure 18: Comparison of finite-difference and complex-step sensitivity estimates. Absolute (a–c) and relative (d–f) differences between sensitivity coefficients computed by finite differences (using the perturbation described in Section 3.7) and the complex-step method.

Appendix J Finite-Difference versus Complex-Step Sensitivity Comparison

To assess numerical accuracy of the finite-difference sensitivity coefficients reported in Section 3.7, we compute the same local sensitivities using the complex-step method [43]. Figure 18 reports absolute and relative differences between the two estimates, showing small discrepancies across all parameters (maximum error $< 8 \times 10^{-4}$).

Appendix K Posterior Summaries and Density Estimation of MCMC Parameters

The smooth density estimates shown in Fig. 4 (intact-mitochondria calibration) and Fig. 5 (proteoliposome calibration) are computed directly from the posterior samples of each parameter obtained by MCMC. For each parameter, we report standard posterior summary statistics (mean, variance, median, and a 95% credible interval) and overlay a smooth density estimate on the corresponding histogram. The pseudocode below summarizes the procedure used to produce the density estimates and summary statistics for Fig. 4.

An analogous procedure is used for Fig. 5, except that KDE is applied to λ_{31}:

Algorithm 1 Posterior density selection and summary procedure for Fig. 4

Require: Posterior samples $\{\theta^{(i)}\}_{i=1}^{N}$, dimension P

```
for j = 1 to P do
    Extract finite samples v_j = {θ_j^(i) : θ_j^(i) is finite}
    Compute posterior mean, variance, median, and 95% credible interval from v_j
    if θ_j = λ_21 then
        Estimate a smooth density f̂_j(x) using kernel density estimation (KDE)
        Compute the posterior mode as arg max_x f̂_j(x)
    else
        if all v_j > 0 then
            Set candidate families F_j ← {Normal, Lognormal, Gamma}
        else
            Set candidate families F_j ← {Normal}
        end if
        for each candidate distribution k ∈ F_j do
            Fit parameters by maximum likelihood
            Compute the log-likelihood ℓ_k
        end for
        Select k* = arg max_k ℓ_k
        Compute the posterior mode from the selected distribution k*
    end if
end for
return Summary statistics and selected density estimate for each parameter
```

Algorithm 2 Posterior density selection and summary procedure for Fig. 5

Require: Posterior samples $\{\theta^{(i)}\}_{i=1}^{N}$, dimension P

```
for j = 1 to P do
    Extract finite samples v_j = {θ_j^(i) : θ_j^(i) is finite}
    Compute posterior mean, variance, median, and 95% credible interval from v_j
    if θ_j = λ_31 then
        Estimate a smooth density f̂_j(x) using kernel density estimation (KDE)
        Compute the posterior mode as arg max_x f̂_j(x)
    else
        if all v_j > 0 then
            Set candidate families F_j ← {Normal, Lognormal, Gamma}
        else
            Set candidate families F_j ← {Normal}
        end if
        for each candidate distribution k ∈ F_j do
            Fit parameters by maximum likelihood
            Compute the log-likelihood ℓ_k
        end for
        Select k* = arg max_k ℓ_k
        Compute the posterior mode from the selected distribution k*
    end if
end for
return Summary statistics and selected density estimate for each parameter
```